AD-A209 874

SOLID STATE
ELECTRONICS
LABORATORY

DEVELOPMENT OF SUPERLATTICES FOR ULTRA HIGH-SPEED ELECTRONIC AND OPTOELECTRONIC DEVICES

FINAL TECHNICAL STATUS REPORT

4/1/86 through 3/31/89

Sponsored by

Office of Naval Research
Contract Number N00014-86-K-0530

DTIC
ELECTE
JUN 30 1989
S D
D

James S. Harris
Prinicipal Investigator
(415) 723-9775

DISTRIBUTION STATEMENT A
Approved for public release;
Distribution Unlimited

STANFORD ELECTRONICS LABORATORIES • DEPARTMENT OF ELECTRICAL ENGINEERING
STANFORD UNIVERSITY • STANFORD, CA 94305-4055

DEVELOPMENT OF SUPERLATTICES FOR ULTRA HIGH-SPEED ELECTRONIC AND OPTOELECTRONIC DEVICES

Final Technical Report

For the period 4/1/86 through 3/31/89

Sponsored by
Office of Naval Research
Contract Number N00014-86-K-0530

James S. Harris
Prinicipal Investigator

Accesion For
NTIS CRA&I
DTIC TAB
Unannounced
Justification
By
Distribution /
Availability Codes
Dist | Avail and / or Special
A-1

Table of Contents

Section I	Introduction	1
Section II-1	Fabrication	10
Section II-2	Experimental Apparatus	12
Section II-3	Experimental Zero-Field Optical Transmission Resusits	14
Section II-4	Experimental Modulation Results	19
Section II-5	*Discussion*	25
Section III	Tunable Fabry-Perot Cavity	27
Section iii-1	Device Concept: P-I-N Diode	28
Section III-2	Modulation of the Refractive Index by Carrier Injection	30
Section III-3	Device Design	37
Section III-4	Device Fabrication	40
Section III-5	Experimental Results	43
Section III-6	Discussion of Results	44
Section IV	The Current-Voltage Characteristics of RTDs	53
Section IV-1	Calculating the Current-Voltage Characteristics of an RTD	53
Section IV-2	Limitations of this Method	55
Section IV-3	Ionized Impurities as a Design Paramenter	62
Section IV-4	The Design of RTDs	71
Section V	RTDs for High Speed Electronics	75
Section V-1	Present State of the Art	76
Section V-2	Pulse Forming Circuit	77
Section V-3	Piecewise Linear Approximation	80
Section V-4	Static I-V Curves	83
Section V-5	Scattering Paramenter Measurements	85
Section V-6	Switching Measurements	88
Section VI	Publications	95

I. Introduction

The remarkable advances in computation and communications technologies in the last half century have been made possible by the invention and development of a vast array of solid state electronic and optical devices. By striving to achieve higher speeds of operation, and greater levels of integration, ever more powerful computing and communications tools have been created. The transistor, the laser and a host of other devices have been invented and reinvented many times in a multitude of materials systems. As materials growth and fabrication technologies continue to improve, it becomes possible to use new physical phenomena in solid state devices, in addition to optimizing the performance of existing devices.

1.1 Optical Devices

Optical interconnects are attracting attention as a means to overcome the interconnection bottleneck in high speed electronic systems. The best type of light source for such schemes is sometimes a continuous-wave laser used in conjunctino with a light modulator, which acts as an external switch. Modulators that operate in perpendicular geometry, with light directed normal to the plane of the device, allow simple fabrication of two-dimensional arrays: these are of interest for multiple parallel optical interconnections and for optical information processing.

The multiple quantum well electroabsorption modulator, the most common perpendicular modulator, suffers from two disadvantages: Its power handling capacity is low, and the operating wavelength is fixed by the material. We propose a new type of modulator, based on tunable optical interference filters, that is non-absorbing and can handle high optical power levels.

Optical interference filters contain alternating layers of two materials with different refractive indices. As a result of multiple reflections from the various interfaces, incident

light may be either transmitted or reflected, depending on the wavelength and the layer thicknesses. Sharp transitions between strong reflection and nearly complete transmission occur over very small ranges of wavelength. Shifting these transitions electrically causes changes in the amount of light transmitted, and hence modulation.

We have fabricated two types of device have been fabricated from gallium arsenide and aluminum gallium arsenide on gallium arsenide substrates by molecular beam epitaxy[1-1]. The first was a "quarter wave stack". Strong electric fields across the structure caused shifts in the transmission spectrum that were sufficient to cause modulation. High voltages were required, however, making it unsuitable for most applications. The "quarter wave stack" is discussed in chapter two of this report. The second was a Fabry-Perot interferometer, which was operated at lower voltage in two modes; one based upon electric field, and a second by carrier injection. The Fabry-Perot interferometer is discussed in chapter 3 of this report.

1.2 Resonant Tunneling Devices

In the area of microwave communications, there are applications for devices with negative differential resistance (NDR). This effect is useful for a number of reasons. By applying the proper bias across the device, it can be used to convert D.C. power into high frequency oscillations. Other applications include signal processing, and using the resonant tunneling device as a load element in a logic circuit.

The existing technologies for obtaining NDR include; the Gunn diode, the IMPATT diode and the Esaki tunnel diode. Unfortunately, there are physical limitations to each of these devices. The Gunn diode operates by transferring charge from the high mobility gamma valley of a semiconductor (typically GaAs) to the low mobility L valley under large electric fields. This device is very important in microwave communications, however, it is fundamentally limited to operating below 150 GHz, and actual operation frequencies are significantly lower (~80 GHz). The IMPATT diode only oscillates at a specific frequency,

fixed by its drift region. It is capable of producing a large power output, however, it is plagued by noise. The Esaki tunnel diode operates by tunneling from the conduction to the valence band through the band gap in a p/n junction diode. This is accomplished by degenerately doping the emitter and collector contacts with n and p-type dopants, respectively. Due to the required proximity of the adjacent contact layers and the very high doping required to achieve tunneling, the capacitance of this device is very large and thus the frequency response is seriously limited. Ultimately, new types of devices will be used to accommodate the demand for increased communication frequencies and signal processing capabilities.

Recently, a new group of high speed electronic devices has been made possible by advances in crystal growth technologies. One of these devices, the resonant tunneling diode (RTD), exhibits NDR at room temperature and has shown the potential to oscillate up to several hundred GHz[1-2]. The potential of RTDs lies in the fact that several of the parameters can be varied resulting in the possibility of achieving both low capacitance and high current density, and thus operation at higher frequencies than are currently possible with either Esaki or Gunn diodes. The flexibility in design parameters also provides the possibility of adjusting the resonant bias condition, the peak to valley ratio, and the peak current density in order to meet circuit design specifications.

In addition to specific investigation of RTDs, one would hope to gain a greater understanding of related device categories. Specifically, the high speed ballistic or hot electron transistor, relies on a similar double barrier structure and shares similar charge transport and quantum physics with these devices. The RTD can also be used as an energy filter within other devices such as the heterojunction bipolar transistor to create new electronic applications. In addition, the double barrier structure is a very simple case of a finite superlattice, superlattices being the foundation for several classes of optoelectronic devices. Perhaps the greatest potential for these devices is the possibility of using several resonant states within the device, or several such devices in series, to provide the building blocks for multi-state logic systems.

In chapter four of this report, the fundamentals of transport in RTDs are discussed[1-4]. This chapter includes experimental work on using ionized impurities as a design parameter

in RTDs[1-4], and extensive discussion of the optimization of RTD performance by using this model. Chapter five contains a discription of the application and measurement of high performance RTDs[1-5] (with peak current densities of 1.4×10^5 A cm^{-2} and peak to valley ratios of 2.5 at room temperature)[1-6]. It is found that RTDs can outperform Esaki diodes for pulse forming applications.

Intensive efforts in the area of RTDs continue in our group, including more work on fundamental transport issues, the vertical integration of multiple resonant tunneling diodes, novel quantum structures, and new applications for high performance RTDs.

References:

1-1. G. W. Yoffe, Ph.D. Thesis, Stanford University, 1988.

1-2. T. C. L. G. Sollner, W.D. Goodhue, P.E. Tannenwald, C.D. Parker and D.D. Peck, Appl. Phys. Lett., **43**, 588, 1983.

1-3 E. Wolak, PhD. Thesis, Stanford University, 1989.

1-4. E. Wolak, K.L. Lear, P.M. Pitner, B.G. Park, E.S. Hellman, T. Weil, J.S. Harris Jr., and D. Thomas, Appl. Phys. Lett. 53 (3), 201 (1988).

1-5. S.K. Diamond, PhD. Thesis, Stanford University, 1989.

1-6 S.K. Diamond, E. Ozbay, M.J.W. Rodwell, D.M. Bloom, Y.C. Pao, E. Wolak and J.S. Harris, Electron Device Letters, 10, 104 (1989).

2. QUARTER WAVELENGTH STRUCTURES

The basic idea for the structure is shown in Figure 2.1. Devices need to have a quarter-wave reflector structure and electrical contacts. The variables to consider were: the wavelength of operation, what materials to use, the number of periods, and the method for making electrical contact.

The operating wavelength had to be in the region where GaAs is non-absorbing, since it was intended that the structures would be fabricated by MBE on doped GaAs substrates. The bandgap of GaAs is 1.42 eV, which corresponds to a wavelength of 8720 Å. This was calculated using the simple relationship,

$$E\,(\mathrm{eV}) = \frac{h\nu}{q} = \frac{\hbar\omega}{q} = \frac{12400}{\lambda(\text{Å})}. \qquad (2\text{-}1)$$

Doped substrate material absorbs some light at longer wavelengths because of bandtail states.[42] In order to be well clear of any absorption the device should be designed to operate at a wavelength greater than 9200 Å. There is always some uncertainty, maybe ± 5%, in MBE growth rates, so it was decided that the devices should have their high-reflectance band centered at 1 μm wavelength. This should put the short wavelength edge of the band at around 9500 Å. In the event that the layers should come out much thinner than intended, the long wavelength edge would still be usable. The long wavelength edge is expected to shift more for a given change in refractive index. Thus it would make sense to design devices with the long wavelength edge of the high-reflectance band at around 9500 Å and with the short wavelength edge buried by absorption. However, it was intended that these devices should demonstrate several effects, including the full high-reflectance band. A spectrum showing only half of it would be less interesting.

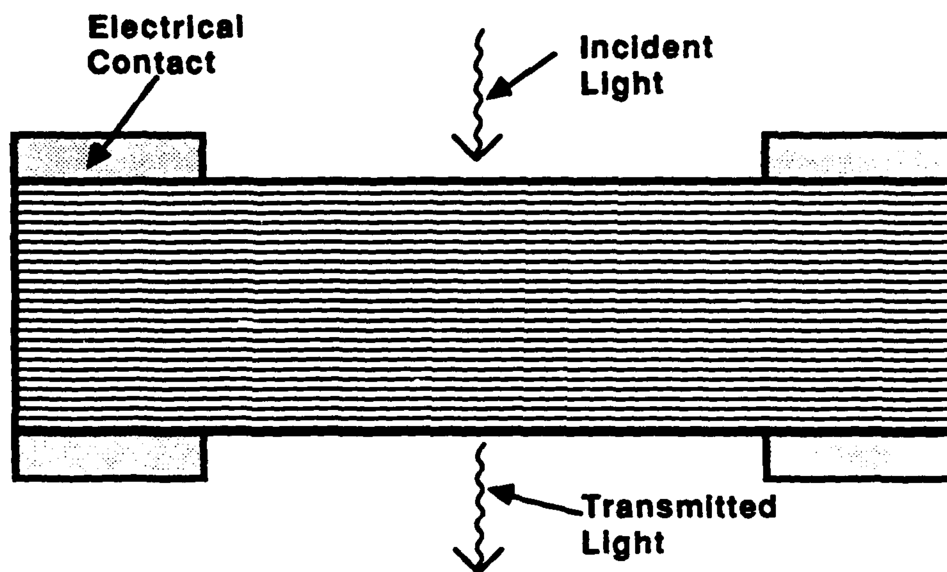

Figure 2.1. Schematic diagram of a quarter-wave stack with electrical contacts.

The choice of materials was simple. The main objective was to maximize the refractive index difference, since this would minimize the number of layers required. Within the $Al_xGa_{1-x}As$ material system, this is obtained by using GaAs and AlAs, with refractive indices at 1 μm of around 3.5 and 3.0 respectively. Quarter-wave thicknesses are therefore approximately 710 Å and 830 Å. It was also desired that a sample should be fabricated incorporating quantum wells, to ascertain whether a similar electrorefractive effect could indeed be obtained. Therefore the GaAs layers were to be replaced by relatively thick GaAs quantum wells, with $Al_{.5}Ga_{.5}As$ barriers. This choice of barrier material gave about the largest conduction band offset, and conveniently allowed equal growth rates of GaAs and AlAs in the MBE chamber. The barriers needed to be at least 50 Å wide, to minimize coupling between wells; it was also desired to keep them as thin as possible, so that the average refractive index of the quantum well layers would be as high as possible.

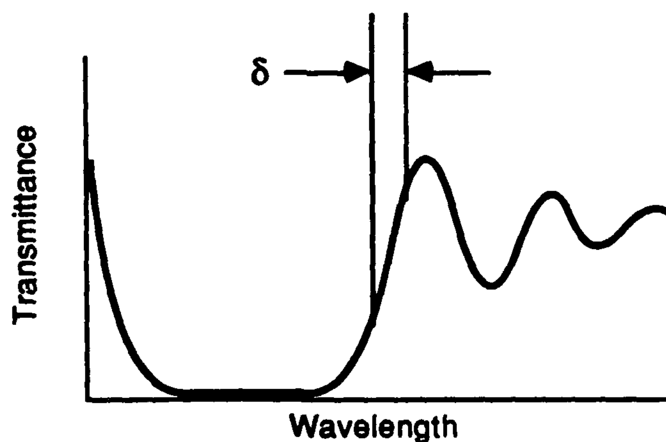

Figure 2.2. The measure of sharpness, δ, for the transmission spectrum of a quarter-wave stack, is the range of wavelength over which the transmittance doubles.

Computer simulations were performed to predict the sharpness of the edges. Since the edges are roughly parabolic, a convenient measure is the wavelength range, δ, over which the transmission doubles or halves, say between 20% and 40%. The predicted

values for δ, the same on each side, are given as a function of the number of periods in Table 2.1.

Table 2.1. Effect of the number of periods on the sharpness of the spectrum.

# of Periods	δ GaAs/ AlAs (Å)	δ Quantum Well/ AlAs (Å)
20.	20	30
30.	8	12
40.	4	6
50.	2.5	3.5

It appears from Table 2.1 that one would like to have as many periods as possible. There are, however, a number of hazy upper limits. Firstly, the MBE machine has a limited quantity of source material and several people want to use it; several 10 μm thick device structures would take a lot of time and seriously deplete the sources. Secondly, a very strong electric field is required in order to see any effect. For a given spectral shift, therefore, a thicker structure requires a greater voltage. A field of 300 kV/cm would drop 4.5 V across each 1500 Å period. A 50-period structure, therefore, would need over 200 V to drive it. This was regarded as excessive, but the device was obviously not going to be a low voltage one. Next, there comes a point where extra layers will not improve matters when laser light is unavailable, as was going to be the case for all of our measurements. The theory for multi-layer interference filters assumes that the incident light is coherent. For monochromated white light, as used in our experiments, the coherence length is only a few wavelengths. Structures more than "a few" wavelengths thick can not be considered thin films, and the theory starts to break down. These then were the considerations. The

compromise chosen was to put 30 periods in the regular quarter-wave stack and 40 periods in the quantum well sample. These numbers put the sharpness, δ, below 10 Å. It was anticipated that non-uniformities across the wafer would be limiting at this point.

As a side experiment, a third structure was designed with an asymmetric multi-layer reflector, containing three eighths wavelength GaAs layers and one eighth wavelength AlAs layers. Such a structure had been suggested, but not demonstrated, by Gourley.[2.1] The theoretical transmission spectrum is asymmetric, but it still exhibits a band of high reflectance, albeit rather narrower than for a quarter-wave stack. The motivation for building this structure was two-fold: Firstly, a larger fraction of the structure is GaAs, and since only the GaAs will be affected by an applied electric field, this should increase any spectral shifts that might be obtained. Secondly, it was hoped that one of the edges of the high-reflectance band might be sharper and cover a wider range of transmittance than the corresponding edge for a symmetric quarter-wave stack. For comparison's sake, a 30-period structure was designed for this one too. The values of δ (compare with Table 2.1) were calculated to be 14 Å on both sides of the band. Theoretical transmission spectra for the symmetric and asymmetric 30-period structures are shown in Figure 2.3.

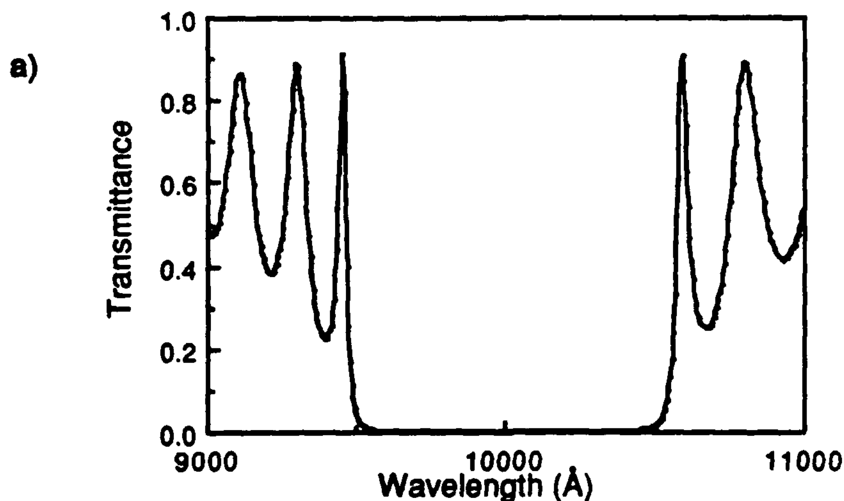

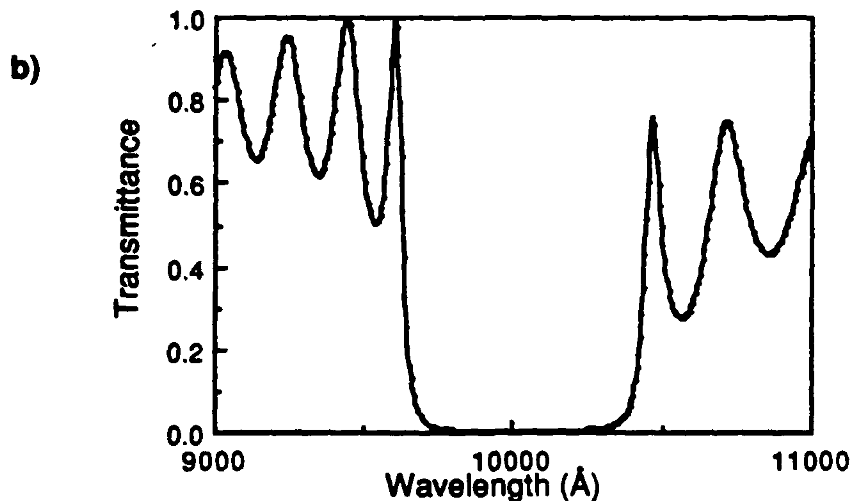

Figure 2.3. Theoretical transmission spectra for **a)** the 30-period symmetric GaAs/AlAs quarter-wave stack, and **b)** the 30-period asymmetric structure, consisting of three-eighths wavelength GaAs and one-eighth wavelength AlAs layers.

2.1. FABRICATION

A schematic cross-section of the actual devices is shown in Figure 2.4. A thin buffer layer was incorporated to smooth out any irregularities in the substrate. The symmetric quarter-wave stack contained 30 periods of alternating layers of GaAs, 714 Å thick, and AlAs, 833 Å thick. In the 40-period stack with quantum wells, each GaAs layer was replaced by three 160 Å GaAs quantum wells with 65 Å $Al_{.5}Ga_{.5}As$ barriers. In the 30-period asymmetric structure, the thicknesses were 1071 Å for GaAs and 417 Å for AlAs.

The structures were all grown on 5 cm diameter substrates in Stanford University's Varian Gen II MBE machine. A growth rate of 0.5 µm/h was selected for both GaAs and AlAs. This rather slow rate has been found experimentally to give smoother interfaces and to reduce the number of oval defects. The substrates were rotated at approximately 10 rpm for the sake of uniformity across the wafers.

The topic of substrate temperature is rather complex. The indicated substrate temperatures were 680^{0} C for the GaAs/A1As structures and 750^{0} C for the sample containing quantum wells. It has been found[2.2] that the quality of $A1_xGa_{1-x}As$ for optical devices impoves monotonically with increasing substrate temperature. At a certain point, however, GaAs begins to desorb, so the flux rates need to be increased to compensate for this loss.[2.3] The amount of material that is lost is hard to predict and is different for GaAs and $A1_xGa_{1-x}As$. In our system, 750^{0} C has been found to be the point where this starts to be noticeable, and the Ga flux rate was increased by 3% to keep the required growth rate. The temperatures given by Ralston et. al.[2.3] are rather lower than ours. this is a result of errors in the thermocouple readings in our machine. Since the wafer is not soldered to a block, but instead held on with wires, it does not become as hot as the thermocouple, which is closer to the heater. Hellman et. al.[2.4] compared thermocouple and pyrometer readings and found a considerable difference. An indicated temperature of 750°C corresponds to a pyrometer temperature of around 650°C, while 680°C, indicated is probably close to an actual temperature of 600°C. Acuurate measurement of substrate temperatures has always been a problem for MBE growers. the substrate was allowed to cool down to 50°C with arsenic overpressure before the A1 Schottky layer was deposited. The thickness of the A1 was nominally 200 Å, but uncalibrated. The growth rates of GaAs and A1As had been calibrated using RHEED oscillations.[2.5] The entire MBE growth process, including the setting of source and substrate temperatures and the operation of the shutters, was controlled by a Hewlett-Packard 9000 computer.

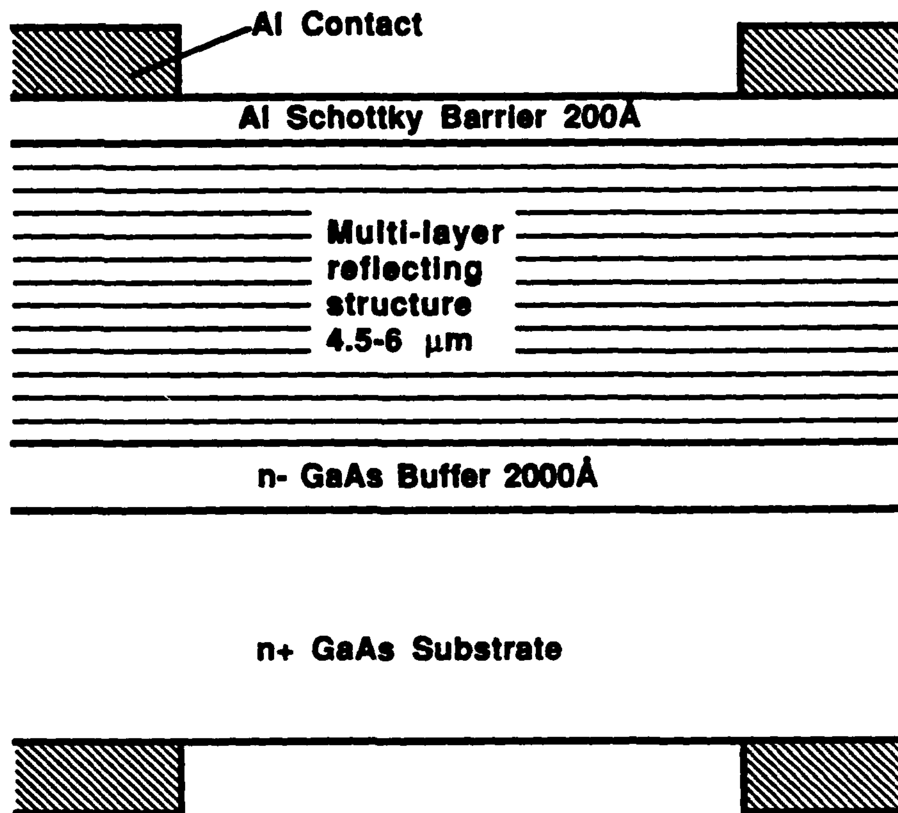

Figure 2.4. Schematic diagram of the modulator. The multi-layer reflector was a 30-period GaAs/AlAs quarter-wave stack in the first sample, a 30-period three-eighths wavelength GaAs/ one-eighth wavelength AlAs stack in the second sample, and a 40-period multiple quantum well/ AlAs quarter-wave stack in the third sample.

The post-growth processing was extremely simple. Aluminum dots were deposited, on both sides of the wafer, through a shadow mask in a bell-jar evaporator. The dots were approximately 3000 Å thick, and 0.25 mm to 1 mm in diameter. They served as robust contacts to allow probing on the epitaxial side of the wafer. An attempt was made to align the dots on the front and rear, so that light would be able to pass between them and through the whole structure. This was found to be no problem. The wafers were then cleaved into small pieces a few millimeters on a side.

2.2. EXPERIMENTAL APPARATUS

The sample holder consisted of a sheet of aluminum with a small hole, approximately 0.5 mm in diameter, drilled through it. A sprung steel clip, its end protected by insulating tape, was used to hold the sample in position over the hole. Ga/ In paint, a liquid at room temperature, was applied to the sample to make good electrical and thermal contact to the aluminum sheet, which formed the positive, grounded, electrode. Tungsten wire, of 0.35 mm diameter, was bent into a suitable shape to act as a probe to make an electrical

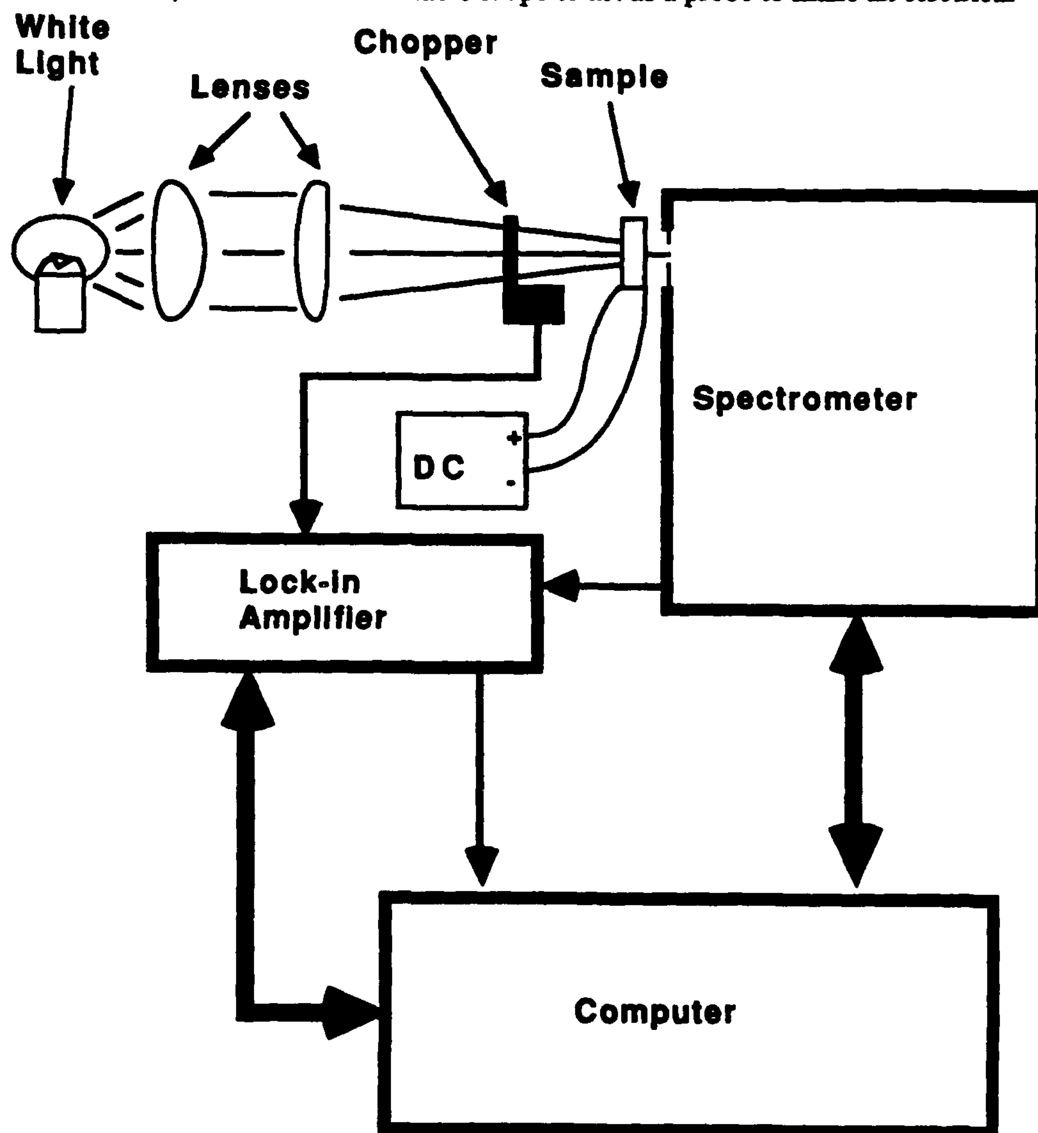

Figure 2.5. Schematic diagram of the apparatus used to measure transmission spectra.

connection between the front side of the wafer and a terminal block. The block was connected to the negative terminal of a DC voltage supply that was capable of providing up to 1000 V. A K-type thermocouple was attached to the regular quarter-wave sample with thermally conductive epoxy.

The apparatus for measuring transmission spectra is shown in Figure 2.5. The samples were illuminated with chopped, focussed white light. They were arranged so that light passed through the substrate first, so that all of the light that might be absorbed was absorbed in the substrate rather than in the epitaxial layers. The light was then focussed into a Spex 1870B 0.5 meter spectrometer, with a cooled S-1 photomultiplier as the detector. Most spectra were taken with the spectrometer slits set to a width of 100 µm, giving 1.6 Å wavelength resolution. The output of the photomultiplier was taken to a lock-in amplifier. The lock-in and spectrometer were both under the full control of our HP 9000 computer.

2.3. EXPERIMENTAL ZERO-FIELD OPTICAL TRANSMISSION RESULTS

All of the zero-field spectra presented for these devices were normalized to take out system non-linearities. A spectrum was measured with the sample holder empty. The measured signal with a device in place was divided by the measured signal for the empty holder at that wavelength. Two effects were expected to reduce the measured transmittances below the theoretical ones presented in Figure 2.4: approximately 30% of the light would be reflected at the air to substrate interface, and an unknown amount would be reflected by the Al Schottky layer.

2.3.1. Zero-Field Transmission Spectra

Figure 2.6 contains experimental zero-bias transmission spectra for the three samples. These may be compared with the theoretical spectra presented in Figure 2.3. Measured values for the sharpness, δ, defined in section 2, are given in Table 2.2.

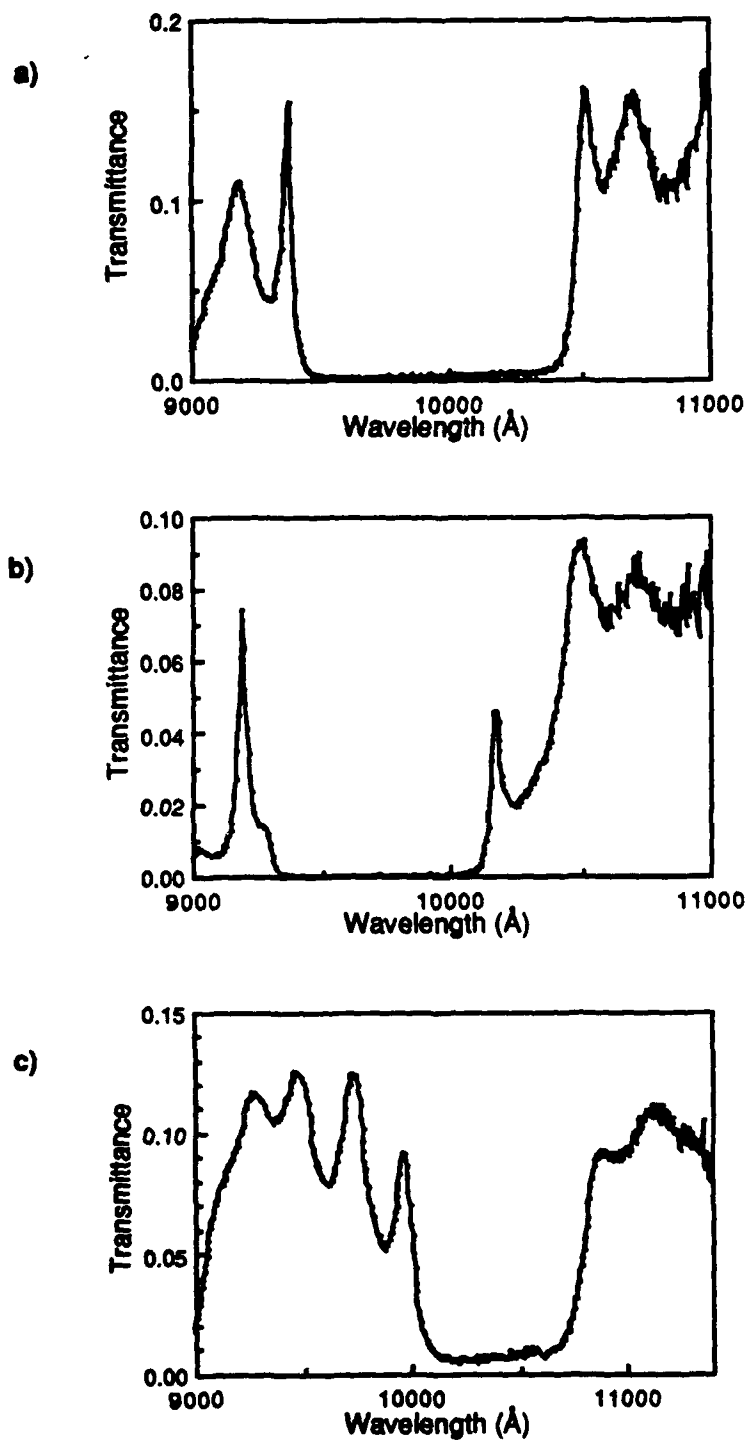

Figure 2.6. Experimental zero-bias transmission spectra for **a)** the symmetric quarter-wave stack, **b)** the symmetric quarter-wave stack with quantum wells, and **c)** the asymmetric structure.

Table 2.2. Experimental and theoretical values of δ (Å).

	SHORT WAVELENGTH		LONG WAVELENGTH	
	δ(theory)	δ(experimental)	δ(theory)	δ(experimental)
Quarter-wave	8	11	8	19
Quantum Well	6	26	6	13
Asymmetric	14	26	14	65

2.3.2. Uniformity Across the Wafer

The peak on the short wavelength side of the high-reflectance band of the regular quarter-wave stack was selected for monitoring, since it was the sharpest feature in any of

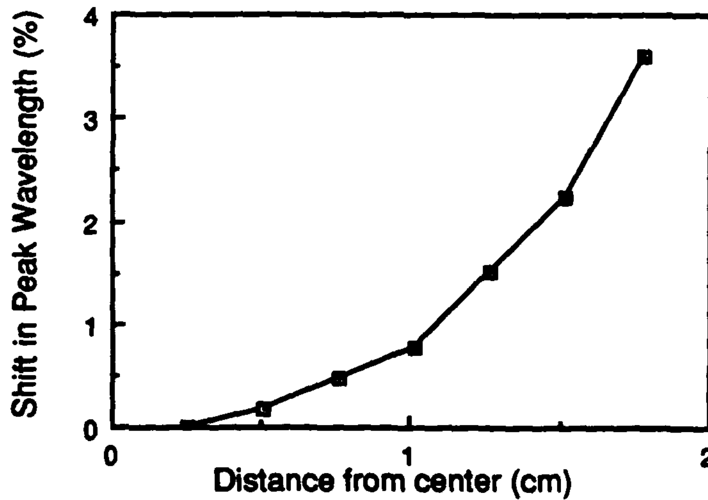

Figure 2.7. Percentage shift in the wavelength of the transmission peak at the short wavelength side of the high-reflectance band for the symmetric quarter-wave stack, as a function of the distance from the center of the wafer.

the spectra. Its wavelength was measured at several points across the wafer. The percentage shift in the peak position is shown as a function of distance from the center of the wafer in Figure 2.7.

2.3.3. Effect of Tilt

The long wavelength peak of the quantum well sample was used in this case, since there was a danger that the peak used above might disappear into the band-edge absorption at a large angle of tilt. Transmission spectra were measured at various angles of tilt. Parts of the spectra for zero tilt and 60° of tilt are shown in Figure 2.8. The fractional shift in the peak compared to its position for normal incidence is plotted in Figure 2.9; the cosine of the internal angle (taking Snell's law into account) is also plotted for comparison.

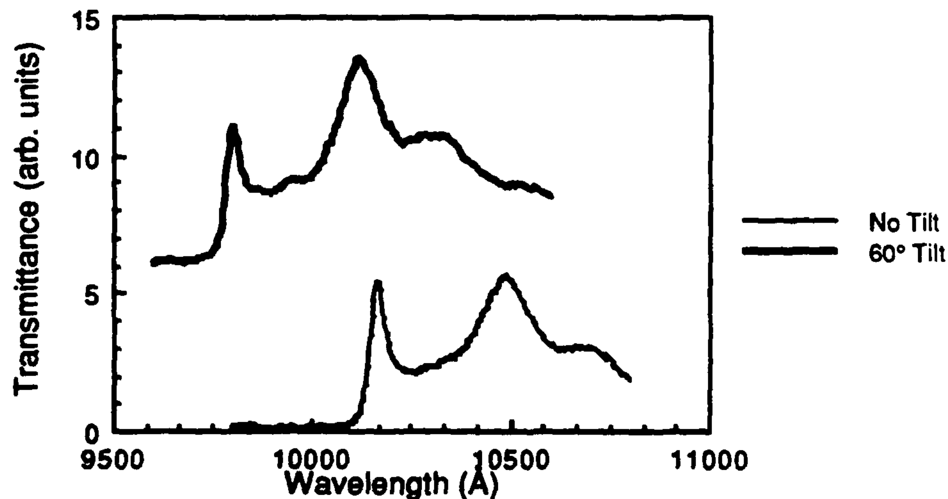

Figure 2.8. Effect of tilt on the transmission spectrum: spectra are shown for the symmetric quarter-wave stack at angles of 0° and 60°.

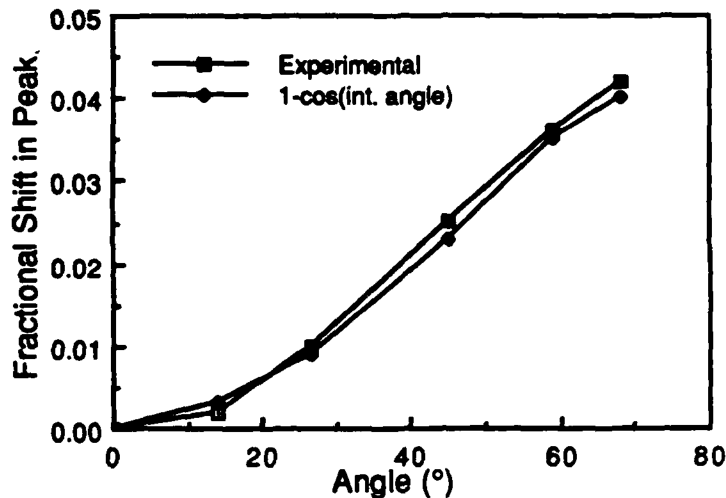

Figure 2.9. Normalized wavelength of a peak in the transmission spectrum of the quantum well quarter-wave stack, as a function of tilt angle.

2.4. EXPERIMENTAL MODULATION RESULTS

2.4.1. Effect of an Electric Field on the Transmission Spectra

Figure 2.10 shows the effect of a strong electric field on parts of the spectra for the two quarter-wave samples. The transmission spectrum for the asymmetric sample was considered not to be sharp enough for it to be worth testing under bias. The devices broke down catastrophically at average applied fields of 200 to 220 kV/cm. The breakdown was somewhat soft. Just below catastrophic breakdown, at an applied voltage of around 100 V, a current of 10 mA was flowing. The quarter-wave device reached a temperature of 40°C at this point, a rise of 17 K over room temperature.

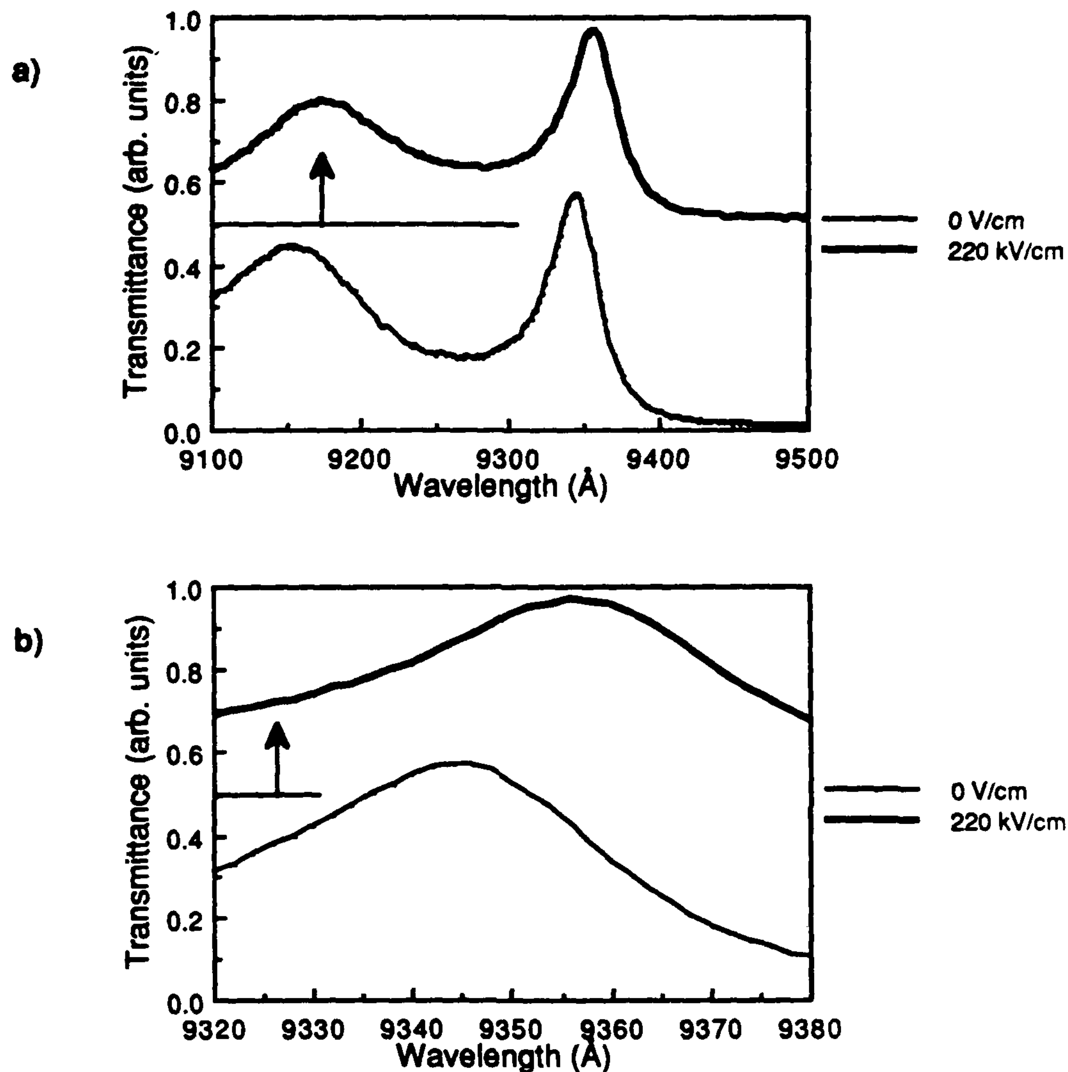

Figure 2.10. Transmission spectra at the short-wavelength edge of the high-reflectance band of the symmetric quarter-wave stack for applied electric fields of 0 V/cm and 200 kV/cm: **a)** wide wavelength scale; **b)** expanded scale.

2.4.2. Modulation of Light

The spectral shifts shown in Figure 2.10 were sufficient to cause modulation of light at various wavelengths. Figure 2.11 contains plots of transmission versus applied field at various wavelengths for the two samples tested. The field-induced shifts were between

10 Å and 15 Å. The selected wavelengths were on the sharpest parts of the spectra, naturally. The maximum modulation ratio was approximately 2.5 for the regular quarter-wave sample, at a wavelength of 9100 Å.

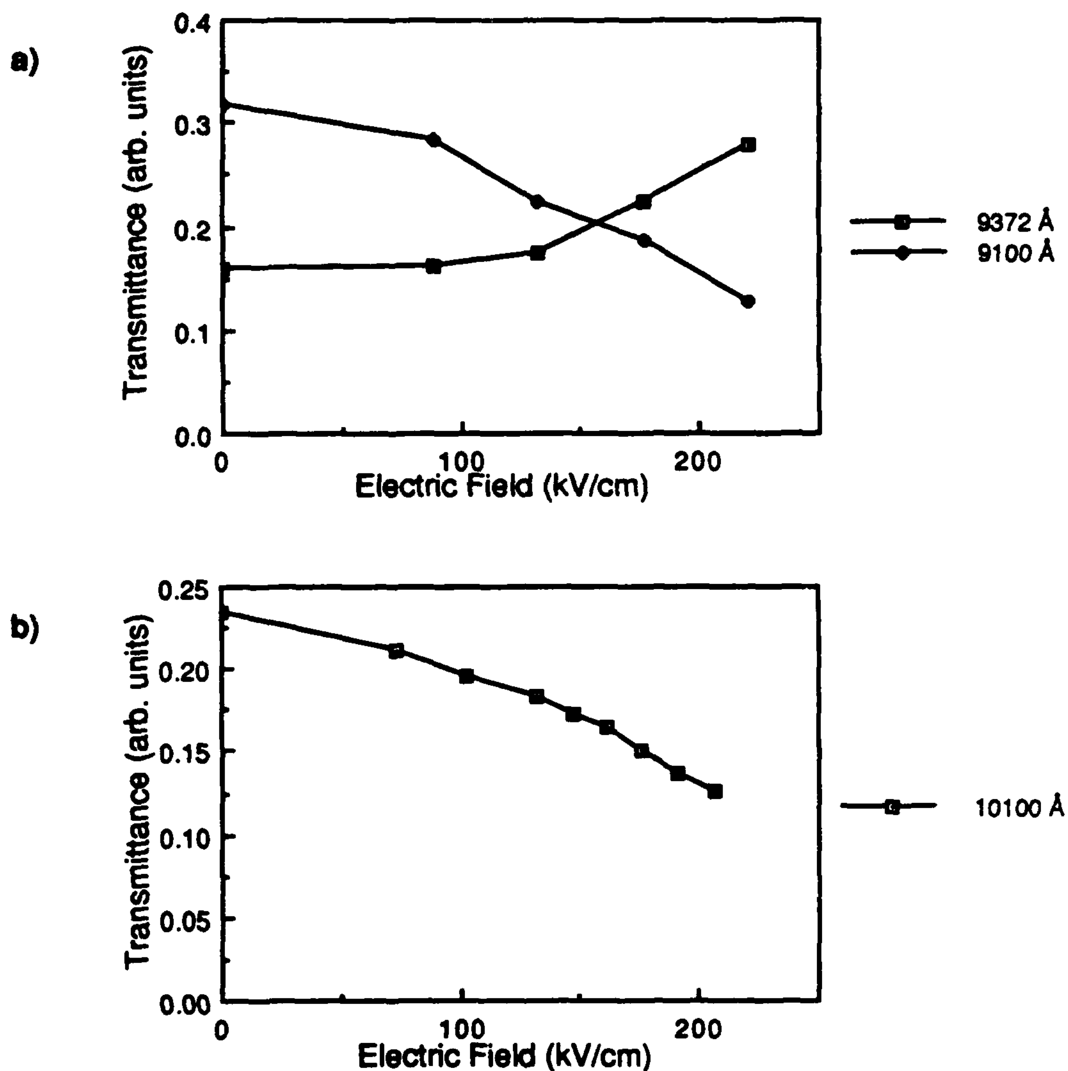

Figure 2.11. Transmittance at selected wavelengths as a function of electric field for **a)** the symmetric quarter-wave stack, on the short wavelength side of the high-reflectance band, and **b)** the quantum well quarter-wave stack on the long wavelength side.

None of the reflectance band edges were as sharp as for the simulated spectra. There are several possible explanations for this. First, non-uniformities across the measurement area would broaden the spectrum. To increase a feature width from 8 Å to 13 Å would require only a 0.1% variation across the sample. From Figure 2.7 we expect rather less than that, since the sample was taken from close to the center of the wafer, and the spot size was approximately 0.5 mm. Some broadening would also have occurred because the light was conical, with a half-angle whose sine was 1/14, to match the input of the spectrometer. This would cause a $\Delta\lambda_\phi$ of 2 to 3 Å, which is fairly insignificant. Another cause of broadening could be oval defects, which are present in all MBE-grown material to an extent dependent on the thickness of the layer. For these thick structures, our machine produces defect densities of several thousand per square cm, so there would certainly have been several inside the measurement area. These defects cause unevenness in the layers, and would therefore cause broadening of the spectrum. A final possible source of broadening lies in the thicknesses of the structures; it is possible that they were beyond the limit of what can be considered "thin films", so that the simulations, assuming coherent light, were not valid.

The reader may observe differences between the spectra of Figure 2.6 and our published spectra.[2.6] The spectra presented here were taken more recently, with a smaller spot size and a much brighter white light source (a 100 W quartz halogen spotlamp). In the case of the asymmetric sample, it is possible that the new spectrum was taken for a sample closer to the center of the wafer than was the original spectrum. The difference in the vertical scales arises from a difference in the normalization techniques. The spectra presented here have been corrected for the response of the system, as described in the introduction to section 2.3. The published spectra were normalized with respect to a "dummy" wafer, which consisted of a heavily doped substrate with a thick layer of $Al_xGa_{1-x}As$ on it. The idea was to remove the effects of substrate absorption and reflection. The factors of 3 to 4 by which the published transmittances are higher is not

fully accounted for by this. The dummy may have been more absorbing than the device substrates, as a result of heavier doping in the substrate or in the epitaxial layer.

The uniformity measurement, Figure 2.7, shows that the layer thicknesses varied by 3 to 4% between the center and the edge of the wafer. It is difficult to determine precisely the variation in thickness from the movement of a peak, since the flux non-uniformities may be different for the different sources.

The variation of the peak position with angle of tilt followed the cosine law very closely. There was some broadening of the spectrum too.

The maximum field that could be applied was 220 kV/cm, calculated by dividing the applied voltage by the total thickness of the epitaxial layers. The field varies through the thickness of the structure because of ionized impurities. If the doping density was indeed 10^{15} /cm^3 as intended, then the electric field at the contact at breakdown was 260 kV/cm, which is very respectable.

The shift in the spectrum that was obtained by increasing the temperature was not consistent with the assertion that only the refractive index of the GaAs would change. We expect a refractive index change of 2.5×10^{-4} /K. This should result in a spectral shift of roughly $0.2 \times 2.5 \times 10^{-4}$ /K /3.5×10000 Å, or 0.15 Å/K, on the short wavelength side of the high-reflectance band. This is much less than the observed shift of 0.5 Å/K, so the index of AlAs must have a similar temperature dependence to that of GaAs. If the two indices had the same temperature dependence, the shift would be around 0.7 Å/K; we can conclude that the refractive index of AlAs increases more slowly with temperature than that of GaAs.

Thermal effects also help to explain why the spectral shifts with applied electric field were rather larger than expected. The short wavelength side of the high-reflectance band of the regular quarter-wave stack shifted by about 13 Å with an applied field of 220 kV/cm. The 17 K temperature rise accounts for approximately 8 Å, or 60% of that shift. If the device had had a better heatsink or a more sophisticated structure to reduce leakage

currents, poorer modulation results would have been obtained. It seems unreasonable to expect electrorefraction alone to have produced shifts of more than 3 Å for either sample. For the regular quarter-wave sample, the peaks were very close to the absorption edge, so there would have been some electroabsorption too. Our simulations did not take absorption into account at all. To incorporate this effect, one could use the complex refractive index, n + ik, in place of the real refractive index, n. In addition to a reduction in the transmitted intensity, which partially accounts for the greater modulation seen at 9100 Å wavelength in Figures 2.10 and 2.11, it may also cause some broadening or shift in the peaks. Absorption cannot explain the size of the shift seen for the quantum well sample, since the photon energy was well below the bandgap. Since the temperature of this device was not measured, it is possible that it heated up more than the regular quarter-wave sample.

2.5. DISCUSSION

2.5.1. Comparison of Results with Theory

The zero-bias optical transmission spectra showed quite good agreement with theory, as can be seen by comparing Figures 2.3 and 2.6. The symmetrical quarter-wave sample, in particular, gave a spectrum very similar in shape and position to the simulation. The width of the high-reflectance band was almost exactly the same as the theoretical value. The maximum values of transmittance for all of the samples were much less than in the simulations because of reflections from the aluminum Schottky contact layer and from the substrate to air interface. Anti-reflection coatings on these surfaces could boost the maximum transmittance. It is likely that there would have been a small amount of absorption due to free carriers in the heavily doped substrates too. The transmittance in the high-reflectance band was very small for both quarter-wave samples, less than 1% even if the spectra are scaled up to give the predicted peak transmittances. The spectrum for the quantum well sample occurs at a slightly shorter wavelength than intended. The error is within the possible calibration error of our MBE machine. It may also be caused by GaAs desorption at the elevated substrate temperature that was not fully compensated for when the beam fluxes were set.

The asymmetric structure showed some asymmetry and a narrower reflectance band in its transmission spectrum, as expected, but the spectrum was generally not as sharp as the others. The reason for this is not clear. Possibly this type of structure is much more sensitive to irregularities in the layers. Our computer simulations showed that this structure is more sensitive to random thickness fluctuations than is the quarter-wave stack. Although Gourley[2.1] proposed this structure, his group has never published any experimental spectra, so maybe it is very difficult to fabricate good devices of this type.

REFERENCES

[2-1] P.L.Gourley, Superlattices and Microstructures **1**, 227(1985).

[2-2] W.T.Tsang, F.K.Reinhart, and J.A.Ditzenberger, Appl.Phys.Lett. **36**, 118 (1980).

[2-3] J.Ralston, G.W.Wicks, and L.F.Eastman, J.Vac.Sci.Technol. **B4**, 594 (1986).

[2-4] E.S.Hellman,P.M.Pitner, A.Harwit, D.Liu, G.W.Yoffe, J.S.Harris, Jr., B.Caffee, and T.Hierl, J.Vac.Sci. Technol. **B4**, 574 (1986).

[2-5] J.J.Harris, B.A.Joyce, and P.J.Dobson, Surf.Sci. **103**, L90 (1981).

[2-6] G.W.Yoffe, D.G.Schlom, and J.S.Harris, Jr., Appl.Phys.Lett. **51**, 1876 (1987).

3 TUNABLE FABRY-PEROT CAVITY

This chapter describes the second, more sophisticated, tunable interference device. A Fabry-Perot cavity consists of two reflectors separated by a spacer; its transmission spectrum exhibits a band of high reflectance, like the spectrum of the quarter-wave stack, but in this case there is a sharp peak of high transmittance at the center of the band. The idea for this device is to tune the light to that resonant peak, which, being very sharp, does not need to be shifted much to produce modulation. Changes in refractive index are employed again, but in this case only the spacer layer needs to be affected. Thus the required voltage will be much smaller than for the quarter-wave device.

A description of a Fabry-Perot interferometer follows, with calculations to find the sharpness of the central resonance. The succeeding sections follow the pattern of the previous chapter, starting with calculations of the effect of changing the refractive index of the spacer layer, followed by an assessment of the magnitude of the change that can be achieved. For this device, two electrical techniques can be used to change the refractive index: a strong electric field, as before, and carrier injection. Device design considerations are then presented. The requirements for good carrier injection are more stringent than those for applying strong electric fields; several factors, including current spreading, device size, and heat flow, had to be considered carefully. Laser diode techniques were used extensively in the analysis and device design phases. The experimental structures are then described, including a detailed processing schedule. This is, to the author's knowledge, the first perpendicular geometry modulator to be designed to operate with carrier injection, and the requirements of bringing photons and electrons together in the active layer were not trivial to fulfill. Experimental results are then presented. Again, they can be described as promising but not at the point where commercial production of the devices is imminent. A cautiously optimistic note is struck in the discussion.

3.1 Device Concept: P-I-N Diode

The simplest type of structure in which a central layer can be affected selectively is a p-i-n diode. The two reflectors are doped, one p-type and one n-type, and the spacer layer is undoped. Since it was planned to use an n-type substrate, the lower reflector would be the n-type one. Figure 3.1 shows the concept. When such a device is reverse biased, most of the voltage is dropped across the intrinsic spacer layer. Thus the field across the spacer is approximately the sum of the applied voltage and the built-in voltage divided by the spacer thickness. In forward bias, carriers are injected into the spacer layer. The compositional changes at the edges of the spacer layer confine most of the carriers, and ideally all of the current is due to recombination inside this layer. Band diagrams for the device under forward and reverse bias are shown in Figure 3.2, where the multi-layer reflectors are approximated by $Al_xGa_{1-x}As$ of an average composition.

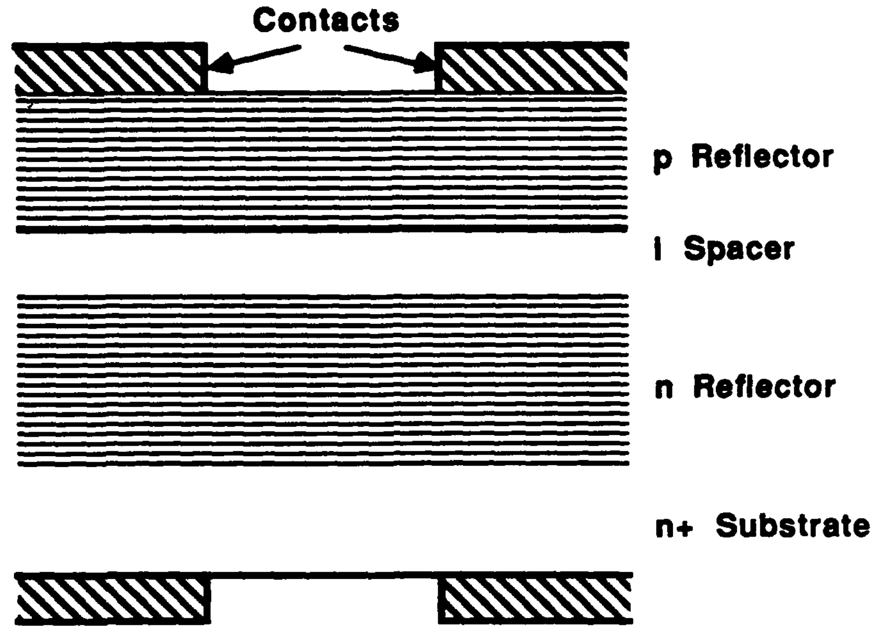

Figure 3.1. Device concept: a p-i-n structure, with doped reflectors and an intrinsic spacer layer.

It will be shown that carrier injection leads to a reduction in the refractive index. This is opposite to the effect of an electric field, so an optimal mode of operation might be to drive the device from a bipolar power supply, switching between forward and reverse bias for the greatest total shift of the peak. Reverse bias will serve the additional function of sweeping out the carriers injected by forward bias, enabling switching times faster than the recombination lifetime to be used. In reverse bias, the maximum change of refractive index is expected to be about the same as for the quarter-wave structure, depending on how high a breakdown electric field can be obtained. The effect of current injection is described below.

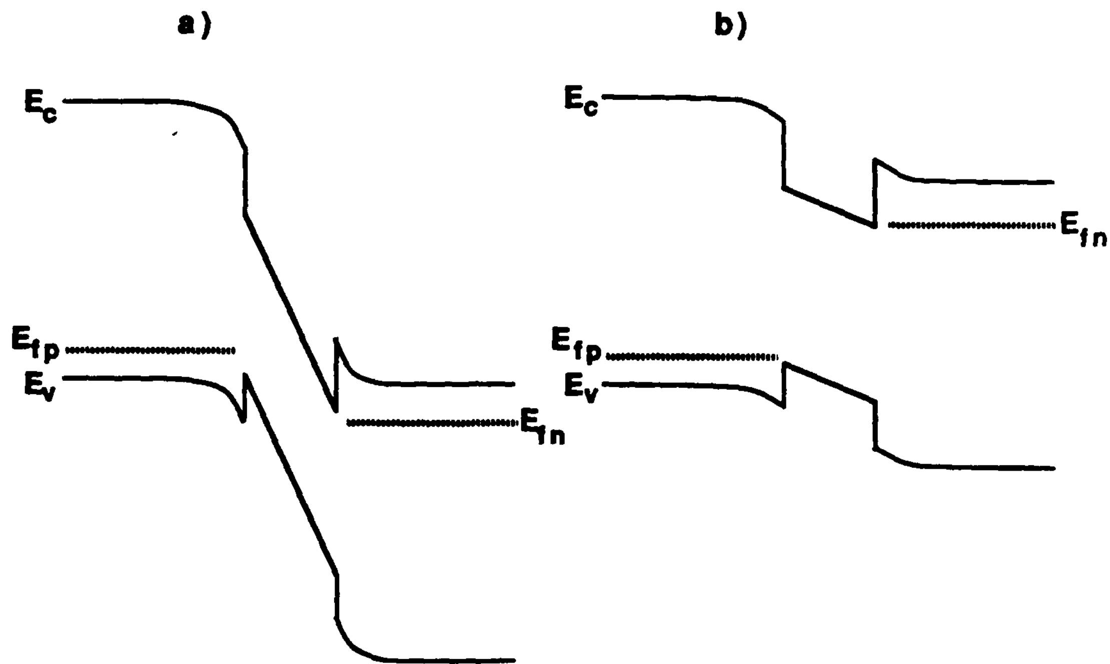

Figure 3.2. Band diagrams of a double-heterojunction P-i-N diode in a) reverse bias and b) forward bias. E_{fp} and E_{fn} are the quasi-Fermi levels for holes and electrons, respectively.

3.2 Modulation of the Refractive Index by Carrier Injection

Calculations of the effect of carrier injection on the refractive index will be presented first, followed by calculations of the current that is required to achieve the necessary carrier density. There are two separate mechanisms by which the refractive index is altered by carrier injection, namely, the plasma effect and band filling, also known as the Burstein-Moss effect.

Kittel [3.1] gives a simple derivation of the plasma effect. He starts with the equation of motion for a free electron in an electric field, and derives the induced polarization. From his equations the change in refractive index can be calculated:

$$\Delta n = \frac{1}{2n} \frac{N\hbar^2}{\varepsilon_0 m_{eh} E^2} \tag{3-1}$$

where N is the density of charged particles, m_{eh} is the reduced effective mass, and E is the photon energy in eV. Substituting $m_{eh} = 0.061 m_0$ and n =3.5 for GaAs, a numerical form can be obtained:

$$\Delta n = -\frac{3.23 \times 10^{-21}}{E^2 (eV)} N \ (/cm^3)\,. \tag{3-2}$$

Unlike the electrorefractive effect, the plasma effect is larger for smaller photon energies. This is because there is a resonance in the response of the plasma at the "plasma frequency", which corresponds to an energy of less than 0.1 eV for carrier densities that can be achieved in semiconductors; the changes in the dielectric constant and the refractive index are greater the closer the photon energy is to this resonance.

Examination of equation (3-2) shows that for photon energies close to the bandgap of GaAs, say 1.2 eV, an injected carrier density of around 10^{18} /cm^3 is required to cause a Δn of 0.1%. This is quite similar to the typical injected density at threshold for a semiconductor laser.

Since the effective density of states in the conduction band is quite low for GaAs, around 4.7×10^{17} /cm^3, injected carrier densities of the required magnitude will put the Fermi level in the conduction band, so the states at the bottom of the band will be filled. This band filling causes a shift, the Burstein-Moss shift, in the absorption edge, since there are no longer any states available to allow absorption of light right at the bandgap. This change in the absorption spectrum leads to a change in the refractive index, which can be calculated using the Kramers-Kronig relationship.

The extent of the band filling, E_1, can be estimated using the Joyce-Dixon approximation.[3.2] At room temperature, an injected carrier density of 10^{18} /cm^3 gives 30 meV for E_1, while 2 x 10^{18} /cm^3 gives 80 meV. Figure 3.3 shows the contributions of the plasma effect and the Burstein-Moss effect to the change in refractive index at these two carrier densities. The band filling effect is greatest for photon energies close to the bandgap, like the electrorefractive effect. The two effects are of similar magnitude at around 1.2 eV. The total change in refractive index is quite encouraging.

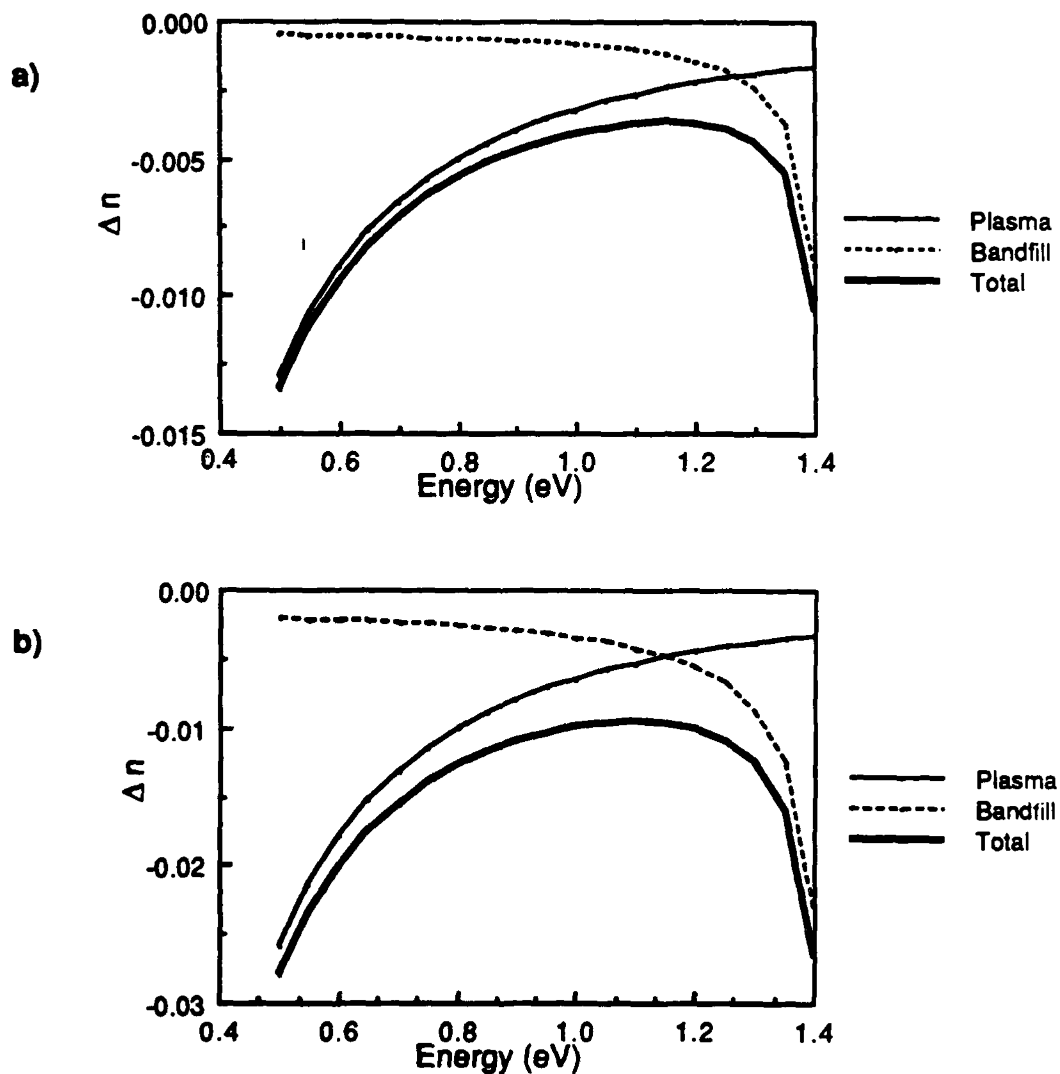

Figure 3.3. Changes in refractive index through the plasma effect and band filling, induced by injected carrier densities of a) 10^{18} /cm^3 and b) 2×10^{18} /cm^3.

It should be noted that a photon energy of 1.2 eV, corresponding to a wavelength of 1 μm, is actually the worst possible operating energy from a device standpoint. However, since our measurement apparatus was set up for this energy range, and since the idea was to demonstrate both forward and reverse bias effects, this was still the chosen operating point.

It is now necessary to determine the current that is required to maintain such a carrier concentration. Assuming no leakage through the heterojunction barriers, an assumption that will be investigated shortly, and ideal interfaces, the current density is simply the rate, J_r, at which injected carriers recombine in the active layer:

$$J_r = \frac{qNd}{\tau} \text{ A/cm}^2 \quad (3\text{-}3)$$

where N is the carrier density, d is the thickness of the spacer, and τ is the carrier lifetime.

There will also be recombination at the $Al_{.4}Ga_{.6}As$/ GaAs interfaces at the sides of the spacer layer. If the spacer layer thickness is much less than a diffusion length then the carrier concentration can be assumed to be constant across it. The interface recombination current density, J_i, can then be written as

$$J_i = 2qNs$$

where s is the interface recombination velocity. The two current components can be combined:

$$J = qNd\left(\frac{1}{\tau} + \frac{2s}{d}\right). \qquad (3\text{-}4)$$

In this form, the interface recombination velocity reduces the effective lifetime, and is important if 2s/d is similar in magnitude to $1/\tau$. For good laser material, $\tau \approx 4$ nS and $s \approx 450$ cm/s.[3.3] With these numbers, interface recombination would halve the lifetime if the spacer layer thickness were less than 360 Å. It is difficult to estimate s in general. If the material is sufficiently bad then s may be high enough to affect the operation of our devices.

Ignoring interface recombination, the required current density is given by equation (3-3). Inserting $\tau = 4$ nS and $N = 10^{18}$ /cm^3, and expressing d in microns, we obtain

$$J = 4000d \text{ A/cm}^2. \qquad (3\text{-}5)$$

For a structure with a 1 µm spacer layer, a 50 µm x 50 µm device would require 100 mA, and a 10 µm x 10 µm device would take 4 mA.

It is now necessary to verify the assumption that no carriers will leak out of the spacer layer over the heterojunction barriers. First it should be noted that rectification will not take place within the reflectors themselves, despite the large number of isotype heterojunctions between GaAs and $Al_{.4}Ga_{.6}As$ layers. Only when the material is lightly doped does diode behavior manifest itself for these junctions. Since we are looking for low resistance, the material will be doped quite heavily, making all the depletion regions thin and making it easy for carriers to tunnel from one material to the other. The spacer layer, however, will be undoped, so the heterojunction barriers will be effective. A good presentation of heterojunction device physics can be found in the book by Casey and Panish.[3.4]

The band diagram of a P-i-N diode under strong forward bias is shown in Figure 3.4.

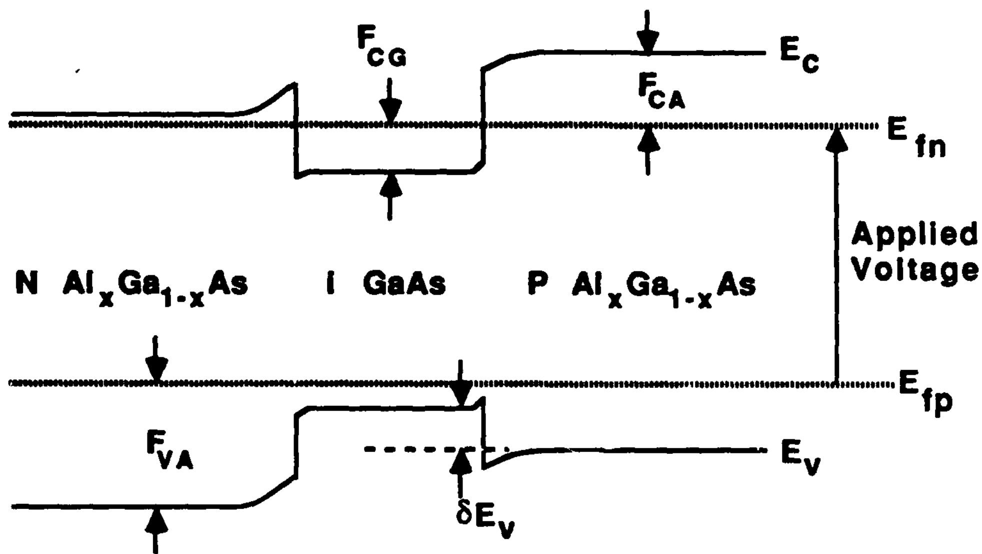

Figure 3.4. Band diagram of a device under strong forward bias, used in calculations of leakage current.

Using the usual simple diffusion current model for a short base diode, and following a similar calculation by Thompson,[3.3] the leakage current of electrons into the P-$Al_xGa_{1-x}As$ is given by

$$J_{1n} = \frac{qD_nN_{CA}}{w_p}\exp\left(-\frac{F_{CA}}{kT}\right) \tag{3-6}$$

where D_n is the diffusion constant for electrons, N_{CA} is the effective density of states in the conduction band in $Al_xGa_{1-x}As$, and w_p is the total thickness of the p-type layers. With the various energies defined in the figure, and a bandgap discontinuity of ΔE_g, F_{CA} can be calculated using the equations:

$$\delta E_V = \frac{kT}{q}\ln\left(\frac{N}{N_{AA}}\right)$$

$$F_{CA} = - F_{CG} + \Delta E_g - \delta E_V \qquad (3\text{-}7)$$

where N_{AA} is the doping density in the P-$Al_xGa_{1-x}As$, and F_{CG} is the same as E_1, defined for band filling earlier. For a doping level of 2×10^{17} /cm^3, $\delta E_V \approx 60$ meV. The appropriate alloy composition is the average composition of the reflector, $Al_{.2}Ga_{.8}As$, which gives $\Delta E_g = 0.25$ eV. Thus $F_{CA} = 0.11$ eV from equation (3-7). With $N_{CA} = 5 \times 10^{17}$ /cm^3, $D_n = 90$ cm^2/s,[30,39] and $w_p = 2.5$ µm, $J_{ln} \approx 400$ A/cm^2.

Thus we see that the barrier is far from perfect, but recombination in the spacer should dominate. Interface quality will affect this leakage current too, since mid-gap states can act as tunnelling paths. The corresponding hole current into the n-type reflector will be rather smaller, since the quasi-Fermi level for holes, E_{fp}, is above the valence band edge in the GaAs, making F_{VA} larger than F_{CA}.

A figure of merit can now be calculated to estimate the modulation depth for a given current as a function of the spacer layer thickness, d. The refractive index change, proportional to N (plasma only), is inversely proportional to d. However, increasing d causes a decrease in the half-power width, δ, and increases the shift for a given Δn. Thus the figure of merit F_m can be written as

$$F_m = \frac{\Delta\lambda(d)\,\Delta n(d)}{\delta(d)} \propto \frac{\Delta\lambda(d)}{d\,\delta(d)} \qquad (3\text{-}8)$$

where both $\Delta\lambda$, the shift of the resonance that is achieved with a Δn of 0.1%, and δ, the resonance width, are obtained from simple computer simulation. Equation (3-8) is plotted in Figure 3.5, with the proportionality taken as an equality and d taken as the order of the spacer. F_m is essentially constant. It does ignore interface recombination, which may be

important for thinner layers, and it assumes that arbitrarily high carrier densities can be obtained.

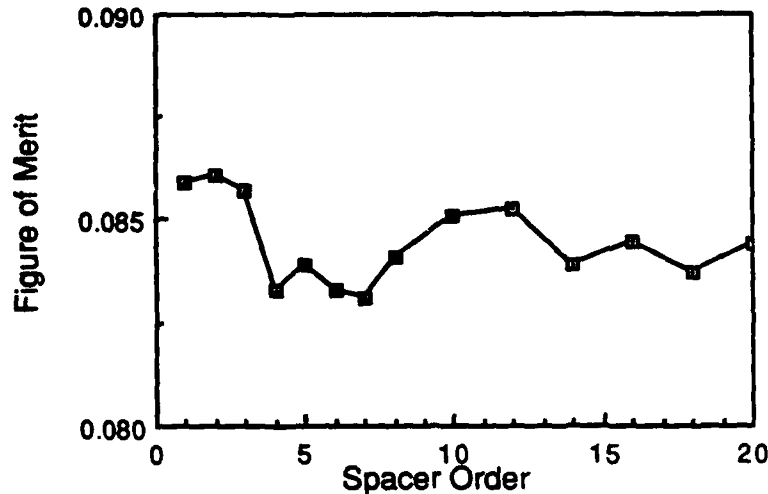

Figure 3.5. Figure of merit for forward bias operation as a function of the order of the spacer layer.

3.3 DEVICE DESIGN

3.3.1 Epitaxial Layers

As was the case for the quarter-wave devices, a number of issues had to be addressed. This time the variables were: the wavelength of operation, the materials to use, the numbers of periods in the reflectors, the thickness of the spacer, and the method for contacting.

The wavelength of operation was chosen to be 1 μm again, even though this is about the worst point for forward bias operation. It was felt that some effect should be obtainable in forward bias, and it was considered desirable to test reverse bias operation too. For reverse bias, the operating wavelength needed to be close to the bandgap, as was the case

for the quarter-wave devices. A peak wavelength of 1 μm allowed some errors in growth rate to be tolerated with little risk of losing the resonance to absorption.

The issue of what materials to use has already been touched on. Ideally one would like to be able to use GaAs and AlAs in the reflectors, since these materials would give the greatest refractive index difference and would therefore minimize the number of layers required. However, high mole-fraction $Al_xGa_{1-x}As$ from our MBE machine tends to have high resistance, probably because of the incorporation of trace amounts of oxygen. Since these devices were going to require large currents, high-resistance reflectors would cause serious series voltage drops and heating. The mole fraction selected was 0.4, the highest that has been used successfully for double heterojunction laser diodes fabricated at Stanford. Thus the device, illustrated conceptually in Figure 3.1, would have a GaAs spacer layer, with reflectors consisting of alternating layers of GaAs and $Al_{.4}Ga_{.6}As$.

The concern in designing test structures was that some shift in the peak should be obtainable with a refractive index change of 0.1%; this would ensure that at least reverse bias should have some effect. Thus the spectrum had to be sharp enough that a shift of a few Ångstroms would be visible. The spacer layer needed to be fairly thick in order to give this much shift. It was decided that two structures would be built, one with a 6th order cavity (3 wavelengths) and one with a 12th order cavity (6 wavelengths). These would have thicknesses of around 0.85 μm and 1.7 μm. There would be little benefit obtained by going to still thicker layers; the main effect would be an increased operating voltage in reverse bias. As was shown in Figure 3.5, for forward bias the spacer thickness is irrelevant to first order. For operation close to the bandgap, a thinner layer might prove slightly advantageous despite the extra interface recombination; the higher injected carrier density for a given current would mean more band filling. The change in refractive index due to band filling can be seen in Figure 3.3 to be super-linear with carrier density.

A peak width, δ, of around 10 Å was desired, in order that a small shift would cause noticeable modulation. This resolution translates to 18 periods in the top reflector and 25 in the lower one.

Ohmic contacts are required for this type of structure. A heavily doped n-type substrate is easy to contact. A heavily doped p+ GaAs cap layer is required on top of the p-type reflector in order for a low resistance contact to be possible there. This p+ contact layer is also crucial to device operation in that it causes current spreading.

For minimum resistance in the reflectors, high doping was required. The Be (p-type) doping level was set at 8×10^{17} /cm^3 in the GaAs. This has been found to be the highest level at which rapid diffusion of Be does not take place at high substrate temperatures. It was vital that the Be did not diffuse into the spacer layer. Since the conductivity of n-type material is much higher than that of p-type material of the same doping density, there is no advantage to using higher n-type doping, and very high doping densities tend to degrade the crystal quality. Therefore the Si doping level was set to 5×10^{17} /cm^3 in the GaAs. A higher doping level was required for the p+ contact layer, and 5×10^{19} /cm^3 was selected. A thickness of 5000 Å was selected; this is typical for laser diodes. This layer would have to be grown at a low substrate temperature to avoid diffusion of Be.

Since the current density, estimated in equation (3-5), was going to be rather large, the maximum practical device dimensions were going to be on the order of 100 μm or less. Chips of this size would be very difficult to handle individually. Larger chips would therefore be used, and some means would be required for blocking the flow of current outside the small device area. Silicon dioxide, silicon nitride, and anodically oxidized insulating layers were rejected in favor of an n-type current blocking layer, that was to be etched away in the actual device area. An n-type layer on the top would form a reverse biased junction to the p+ contact layer, and would therefore prevent any current from flowing where it was present. The layers selected were 1000 Å of n-type $Al_{.4}Ga_{.6}As$ and 2000 Å of n-type GaAs, with doping levels of around 10^{18} /cm^3, to be grown on top of the

p+ contact layer. The $Al_{.4}Ga_{.6}As$ layer was to serve as a marker, so that cross-sectional scanning-electron-microscope (SEM) photographs could be used to determine whether the etch was complete. Since slight over-etch was anticipated, a thickness of 7000 Å was selected for the p+ contact layer, to ensure that at least 5000 Å were present everywhere.

3.4 DEVICE FABRICATION

3.4.1 MBE Growth

The two device structures, 6th order and 12th order Fabry-Perot interferometers, were grown in the MBE chamber, under computer control again. A GaAs growth rate of approximately 0.5 µm/h was used again. Experiments with semiconductor lasers had indicated that the optimum growth temperature for optical devices was around 850°C indicated (probably around 720°C actually). Unfortunately, at the time that the growths were performed the fluxes from the GaAs cells were not stable enough to give precise growth rate control at this high a temperature. At such high substrate temperatures considerable GaAs desorption takes place. At 850°C the loss rate was found to be equivalent to approximately 0.75 µm/h, so that an effective growth rate of 1.25 µm/h would be required to give an actual 0.5 µm/h growth rate. With the uncertainties in the effective rate it was not possible to obtain sufficient accuracy in the actual rates. Therefore an indicated temperature of 700°C was used. Desorption had been found to be fairly insignificant below 750°C indicated, but the surface morphology of structures containing a lot of $Al_xGa_{1-x}As$ had been found to be very poor if the substrate temperature was between 720°C and 800°C. In order to obtain good morphology and predictable growth rates, 700°C was the maximum safe temperature. The temperature was reduced to 600°C indicated for the p+ contact layer and the n-type current blocking layer, in order that the Be

would not diffuse to the other layers. For these layers material quality and carrier lifetimes were not important.

The substrates were rotated during growth to improve the uniformity. To make the interfaces as smooth as possible the growth was interrupted after each layer. Growth interruption has been found to give much smoother interfaces, as a result of increased island size, but also allows the incorporation of more impurities at the interfaces if interruptions of longer than 30 seconds are used.[3-5] Interruptions of 10 seconds after each GaAs layer and 30 seconds after each $Al_xGa_{1-x}As$ layer were used; these times had been found by RHEED studies to be sufficient to give a significant improvement in the surface structure.

3.4.2 Device Processing

The processing for these devices was considerably more complex than for the quarter-wave structures and involved three masks. Quarter wafers were processed.

The first step was to etch the windows in the current blocking layer. After a standard degrease in trichloroethane, acetone, methanol, and de-ionized water, the 65 µm x 65 µm window areas were defined lithographically, using a standard process with AZ 1370SF positive photoresist. Since the chips were eventually to be separated by cleaving, care was taken to align the chip edges to the cleaved edges of the quarter wafers. The n-type current blocking layer was then etched in H_3PO_4:H_2O_2:H_2O 1:1:30 for 4.5 minutes at 15°C. This solution etches GaAs at 800 Å/min and $Al_{.4}Ga_{.6}As$ at 1000Å/min, approximately. An extra minute was given to obtain a slight over-etch, to ensure that the $Al_{.4}Ga_{.6}As$ was all removed. The etch depth was checked by SEM using stain-etched samples. It was found that almost 2500 Å of the p+ contact layer had been removed, rather more than intended, but still leaving over 4000 Å, enough for contacting and for current spreading purposes. The photoresist was then removed with acetone.

The next step was application of the p-type metallization. Lift-off, incorporating a chlorobenzene soak,[3,6] was used to define the pattern. After a full degrease, the photoresist was spun on at 3000 rpm, rather than the usual 5000 rpm, to give a thicker layer, around 1.4 μm according to the manufacturer's data sheet. After a pre-bake, the wafer was soaked in chlorobenzene for 20 minutes. This hardened the top layer of the resist, so that the developed profile would be undercut, making lift-off more likely to succeed. After a standard exposure, the required development time was roughly double that of untreated resist. The post-bake was done at the relatively low temperature of 85°C to make the resist easy to remove. Surface oxides on the GaAs were removed by dilute HCl followed by a 15 second water rinse. An electron-beam evaporator was then used to deposit 1000 Å of Ti and 3000 Å of Au. The amount of metal to be removed by lift-off was rather small, just the 5 μm to 25 μm stripes in the active area and 40 μm stripes between chips. After a long soak in acetone, gentle rubbing with a cotton swab was required to remove the unwanted metal.

The wafers were then thinned before application of the n-side metal. This was to facilitate accurate cleaving, both for final device separation and to provide clean references for alignment during backside lithography. The wafers were first thinned mechanically to approximately 110 μm, using 5 μm Al_2O_3 powder. Chemical polishing, using full-strength domestic bleach (a sodium hypochlorite solution), removed a further 20 μm. A mirror finish was obtained by polishing with heavily diluted bleach.

Preparation for the backside metal deposition was the next stage. The thinned wafers were cleaved carefully, and the exact positions of the cleaved edges with respect to the patterns were noted. The wafers were then attached p-side down to microscope coverglasses, using photoresist as an adhesive. This made them more robust for handling, and also protected the front side from the etches that were to be used on the backside. The backside was then etched in H_2SO_4:H_2O_2:H_2O 8:1:1 at room temperature for 30 seconds, to remove about 0.75 μm. After etching the backside had an uneven appearance, mirror-

like in some areas, cloudy in others. This indicated that insufficient chemical polishing had been performed, and that there was still damage from the mechanical thinning. It would have been better to leave at least the last 30 μm of thinning to the chemical polish.

The electron-beam evaporator was then used to deposit, in sequence, 400 Å of Au, 100 Å of Ge, 125 Å of Ni, and 4000 Å of Au, a standard n-type ohmic contact. The pattern for etching was defined by the third photolithography stage, with the cleaved edges being used for alignment. Because photoresist was being used to attach the wafers to the coverglasses, the usual high temperature singe before application of the resist was omitted, and adhesion promoter was used instead. This was found to work well with the coarse geometries that were involved. The unwanted gold was removed using a proprietary gold etch, consisting of KI and I_2. The wafers were then removed from the coverglasses using acetone. After a full degrease, the metallization was annealed for 20 seconds at 440°C using a rapid thermal annealer.

The individual 800 μm x 800 μm chips were then cleaved along the gaps in the front side gold. It was found that the alignment of the lithographies on the front and back had been accurate to within 10 μm in all cases.

The copper heatsinks were then prepared. They were degreased and etched in HCl for 1 minute to remove all traces of oxide. A bell-jar evaporator was then used to deposit indium to an uncritical thickness of several microns. A chip was then placed carefully on the raised mesa of each heatsink. A small weight was lowered onto the chip, and the heatsink was then placed on a hotplate to melt the indium and to attach the chip securely. Large contact pads were glued to the heatsinks near the chips, using epoxy adhesive. These pads were waste thickness monitor crystals from the electron-beam evaporator, comprising quartz wafers coated with gold on one side. A wire bonder was used to connect the backside metal to the contact pad using aluminum wire.

3.5 EXPERIMENTAL RESULTS

3.5.1 Zero-Bias Optical Transmission Results

The same apparatus was used for these devices as for the quarter-wave structures. Zero-bias transmission spectra for the 3-wavelength structure and the 6-wavelength structure are shown in Figure 3.6. These spectra were taken using unprocessed pieces of the wafer with a spot diameter of approximately 0.5 mm. The half-power widths of the Fabry-Perot resonances in these spectra were 26 Å for the 3-wavelength sample and 19 Å for the 6-wavelength structure. For processed devices, however, these widths were 19 Å and 9Å, respectively, as shown in Figure 3.7, because of the greatly reduced size of the probed area. The small size meant that it was not possible to obtain full spectra out to 11000 Å for the processed devices, since the sensitivity of our system (especially the photomultiplier) drops off very rapidly with increasing wavelength. At this stage it was found that devices with shiny backside finishes exhibited multiple transmission peaks resulting from Fabry-Perot resonances from the whole wafer. Devices with cloudy backside finishes did not have this problem, so devices of this type were selected for testing. Of course, a better remedy would be to apply an anti-reflection coating to the backside.

a)

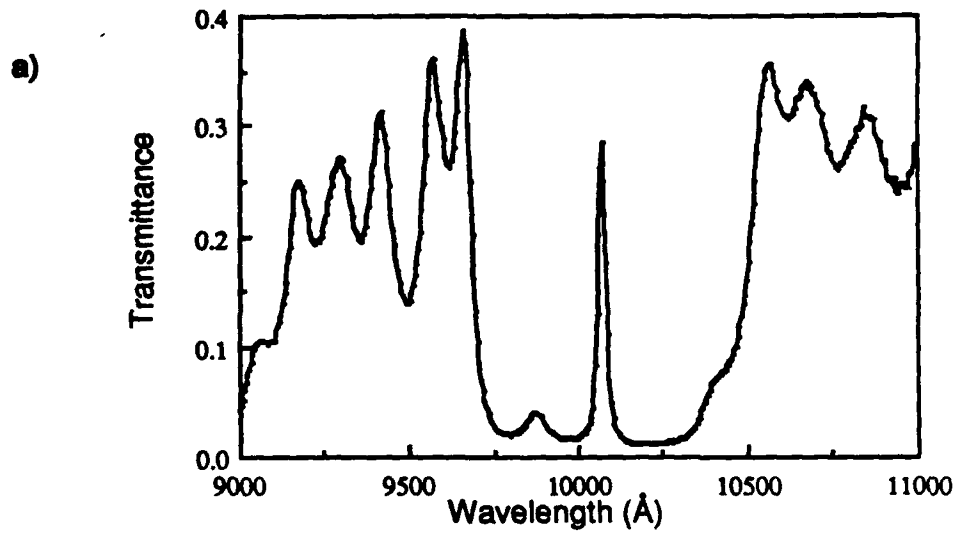

b)

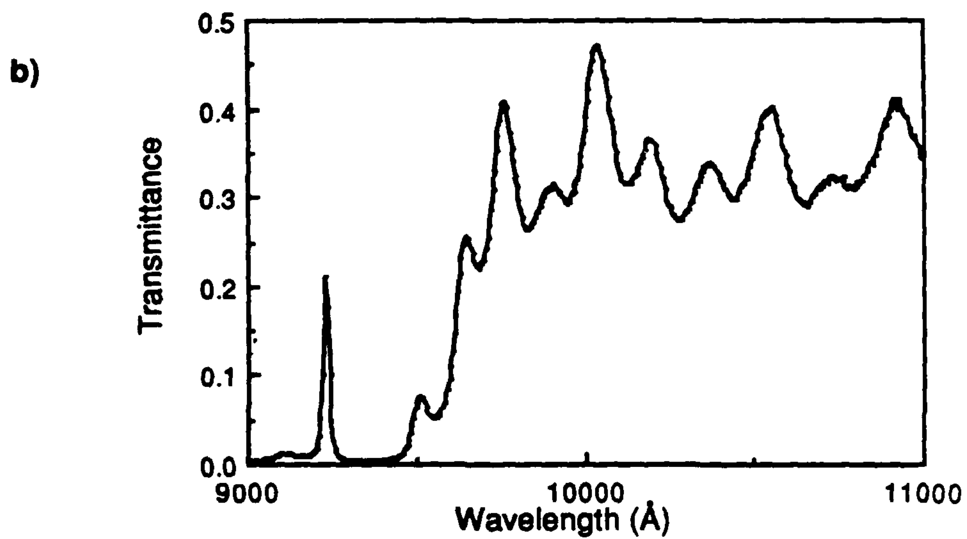

Figure 3.6. Zero-bias transmission spectra for the Fabry-Perot structures with spacer layer thicknesses of **a)** 3 wavelengths, and **b)** 6 wavelengths.

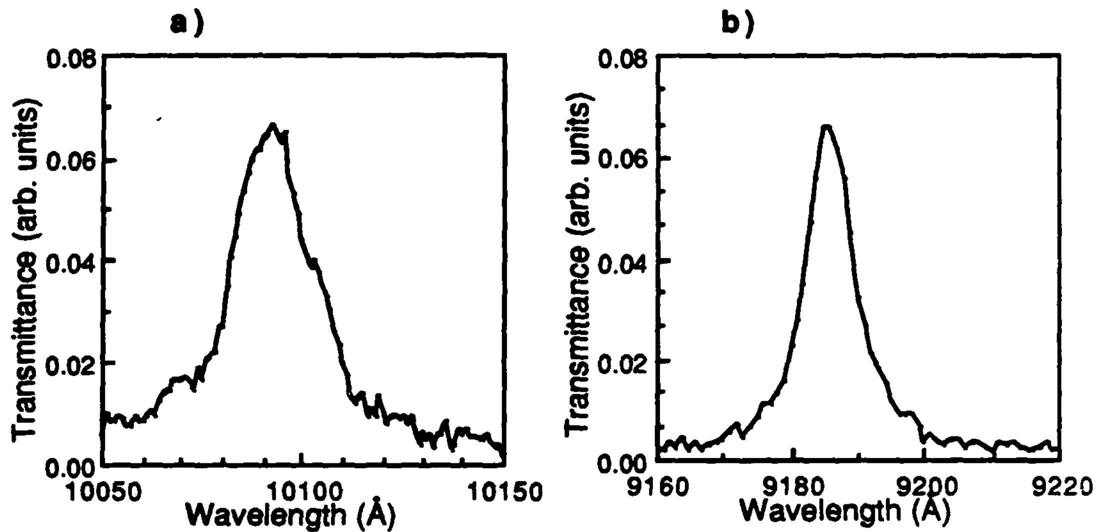

Figure 3.7. Expanded transmission spectra to show the Fabry-Perot resonances of **a)** the 3-wavelength device, and **b)** the 6-wavelength device.

3.5.2 Modulation Results

Devices were selected for reverse-bias tests on the basis of their breakdown voltages. The maximum voltages that could be applied were around 20 V for the 6-wavelength devices and 10 V for the 3-wavelength devices.

No significant effect was seen on the spectrum of the 3-wavelength device, but a clear effect was seen with the 6-wavelength one. Figure 3.8 shows the effect of a reverse bias of 20 V. The peak shifted by 3 Å and decreased in size. A modulation ratio of 2:1 was obtained at a wavelength of 9198 Å. The reverse leakage current for 20 V applied was approximately 25 μA.

For forward bias, good current-voltage characteristics were required, to minimize heating. A forward voltage drop of 2 V for a current of 100 mA is very respectable, and indicates that the ohmic contacts and reflectors had low resistance. For optical testing pulsed current was required. A pulsed power supply designed for laser diodes was used. It provided 30 mA of DC current with pulses of up to 400 mA superimposed. Pulse

widths of 1 μS to 5 μS were used.

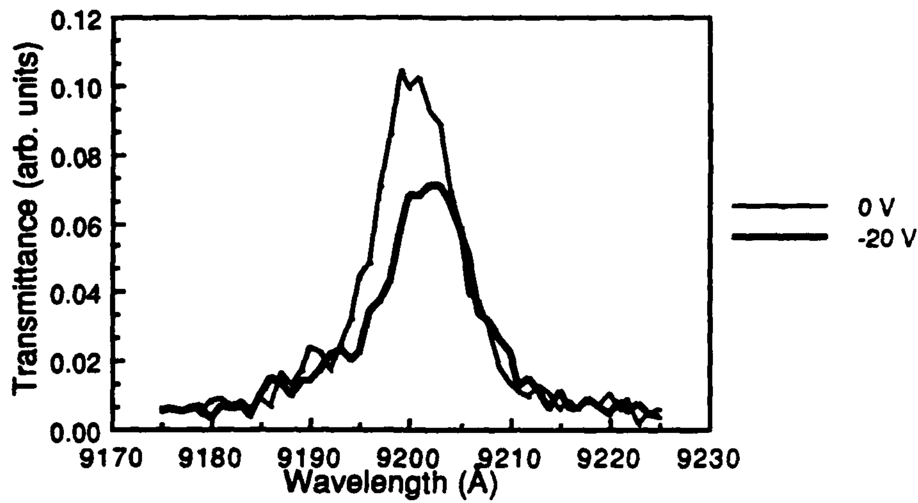

low

Figure 3.8. Effect of reverse bias on a 6-wavelength device: transmission spectra of the Fabry-Perot peak for zero bias and for 20 V applied reverse bias.

Unfortunately it proved to be impossible *to obtain* modulation results under forward bias, since the injection of carriers caused the emission of a lot of light. The devices were behaving as light emitting diodes. The spectra of emitted light for two devices are shown

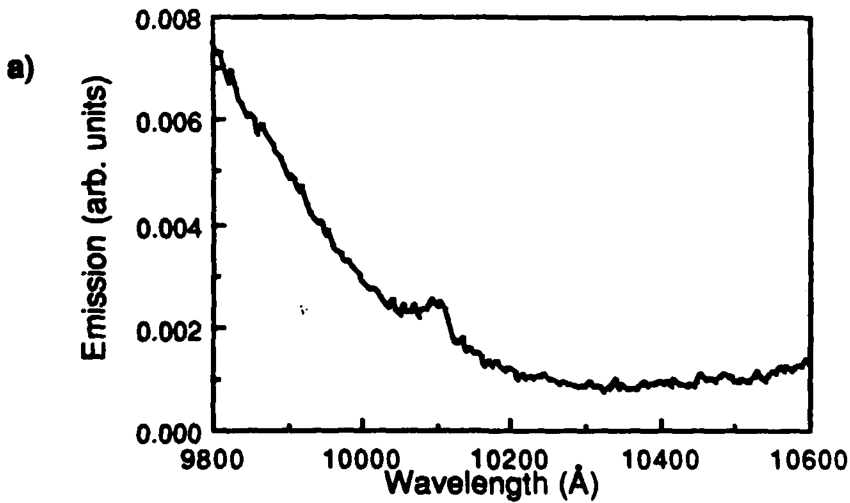

b

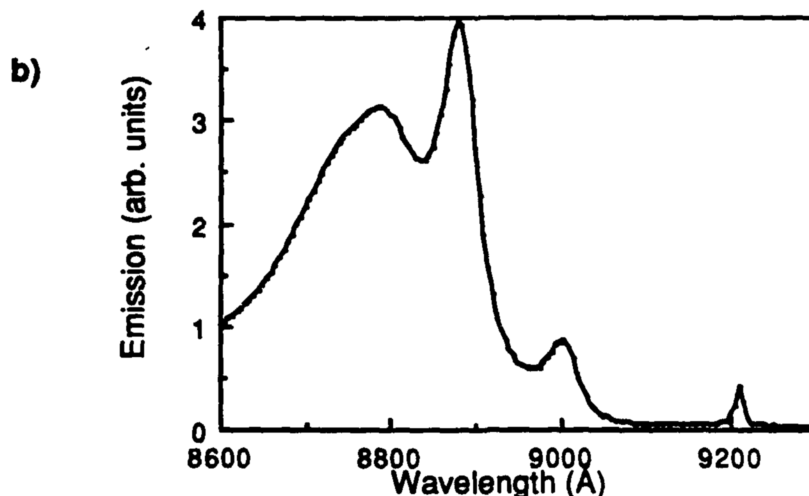

Figure 3.9 Spontaneous emission spectra near the Fabry-Perot resonance for **a)** a 3-wavelength device and **b)** a 6-wavelength device.

in Figure 3.9, uncorrected for system errors. With 200 mA of bias the amount of light emitted at the peak wavelength of 9200 Å was almost an order of magnitude larger than the transmitted light that originated in the white light source. The same effect was found for the 3-wavelength device. The first effect that was obtained upon increasing the forward bias was a small increase in the signal at a current of around 300 mA. This increase was also due to radiation from the modulator. A commercial infra-red light-emitting diode, with an emission peak at 9400 Å was tried, but it too gave out insufficient light to mask the modulator's emissions.

3.6 DISCUSSION OF RESULTS

The zero-bias spectra are qualitatively in agreement with the theory. The resonant peaks are not quite as high as the edges of the high-reflectance band, which suggests that the reflectors were not perfectly matched. The overall magnitude of the transmittance is lower than that in the simulation because of reflections off the substrate and small amounts

of absorption there. The position of the resonance for the 6-wavelength device was at a rather shorter wavelength than that for which it was designed, because of the unstable gallium source in our MBE machine. A number of wafers also came out with wildly inaccurate thicknesses. The designed widths of the peaks were 12 Å and 9 Å, so the obtained values of 19 Å and 9Å were quite satisfactory. The peak for the 3-wavelength device appears to be somewhat asymmetric. This wafer had the shinier backside and greater problems with multiple peaks, so the shoulder on the peak may well be caused by extra reflections, despite the care that was taken to select a device with a cloudy backside. The considerable narrowing of the peak that was obtained for the tiny devices compared to pieces of unprocessed wafer demonstrates that the broadening irregularities were on a small scale.

The reverse bias modulation that was obtained with the 6-wavelength device was made possible by the growth rate inaccuracy, which put the peak very close to the bandgap. The sharpness of the peak meant that only a very small shift was required for modulation to occur. Electroabsorption was also taking place, as shown by the reduction in the height of the peak. There was no problem with device heating here. The 500 μW being dissipated would have caused a shift of less than 0.1 Å, according to the DC measurement made in forward bias. According to the calculations, 500 μW should cause a temperature rise of around 0.1 K, assuming a thermal resistance of 200 K/W. The modulation obtained was promising, especially since the applied field was only a little over 100 kV/cm, but the shift was still only of the same order of magnitude as the stability of a real source. Furthermore, this Franz-Keldysh shift is only possible very close to the bandgap, where some electroabsorption is taking place, and where quantum well electroabsorption modulators will generally be easier to use.

The forward bias results were disappointing. Carrier injection was clearly demonstrated by the emission of light. In order to see any shift in the spectrum, however, high carrier densities, close to those needed for superluminescent radiation, are required.

The spontaneous emission spectrum is quite broad, and it was no real surprise that it extended through the 9200 Å peak of the 6-wavelength device. The long wavelength emission at 1 μm from the 3-wavelength device was probably due to donor-to-acceptor recombination; it may well have originated partly in the N-type $Al_{.4}Ga_{.6}As$, which frequently shows broad photoluminescence in the middle of the bandgap. The relative broadness of the peak, 19 Å, meant that a shift of only a few Ångstroms would have been hard to discern. It was hoped that a commercial light-emitting diode (LED) might produce enough light to completely obscure the modulator's emission, but it proved to be impossible to collect and focus sufficient light. The modulator had a tiny active area and was being driven very hard, at up to 400 mA. The LED's active area was much larger, probably by a factor of over 100, and only a small fraction of its radiation could be focussed onto the modulator. Reflections off the backside of the modulator would have further reduced the incident intensity. For operation at wavelengths so close to the bandgap, a laser light source is required. Unfortunately that is a very difficult wavelength range for both semiconductor lasers and dye lasers.

The DC measurement was a good demonstration of the heating problem. Injected carriers should cause a small peak shift to shorter wavelength. The 100 mW dissipation caused a large shift to longer wavelength by heating the whole device, not just the active layer. For the Fabry-Perot structure we would expect that the fractional shift in the peak per degree of temperature rise would be similar to that of the quarter-wave structure, around 0.5 Å/K. The observed 15 Å shift therefore corresponds to a temperature rise of around 30 K, indicating a thermal resistance of around 300 K/W, rather worse than the calculated value. That particular sample was not attached very securely to the heatsink, however, so this may not have been a typical result. No thermocouple measurements were taken, because of the difficulties involved with attaching a thermocouple to a chip with dimensions less than 1 mm.

Since no modulation results could be obtained in forward bias, it was not possible to attempt high-speed measurements. Since the mechanism for operation is rather similar to that of a laser diode, laser switching speeds give a guideline on the speeds that could be expected. The carrier lifetime decreases with increasing carrier density, so an appropriate mode of operation might be to bias the device well into the high-level injection regime and to apply a modulating signal on top of that. Since higher carrier densities are obtained for a given current in devices with thinner spacer layers, fast devices might be designed with a low-order spacer cavity.

The concept of the tunable Fabry-Perot structure has been demonstrated. Very sharp resonances have been obtained. These structures could form the basis of useful modulators if it were possible to cause appreciable shifts in the position of the peak. The shift that was obtained with reverse bias demonstrated that the spectrum can be tuned electrically, but it was not sufficient to make a useful device. For sub-bandgap operation, carrier injection appears to be the technique of choice. For our structures, the spectrum was too close to the bandgap, so that spontaneous emission from the highly pumped spacer layer obscured any shifts that may have been occurring. The quality of the $Al_{.4}Ga_{.6}As$ was suspect because of the low growth temperature, and it is possible that insufficient numbers of carriers were being injected. The long wavelength emission seen from the 3-wavelength device may well have originated in an $Al_{.4}Ga_{.6}As$ layer.

The plasma effect is greater at longer wavelengths, further from the bandgap. This type of device is therefore best suited to operation at such a wavelength. GaAs-based devices may prove to be useful at the common fiber-optics wavelengths of 1.3μm and 1.55 μm. Should optical communication systems ever be built to operate at even longer wavelengths, say 5 μm or 10 μm, these devices might really come into their own. The alternatives at present are HgCdTe devices, which have great problems with the material technology, and GaAs quantum well devices using inter-subband transitions.[70]

Some of the problems associated with the quarter-wave device are also present in this device. Layer thickness control and uniformity are critical again; this one feature makes all tunable interference filters impractical with current MBE technology. Tilting is not so practical as a tuning mechanism for these devices, since the heatsink will block the light if it is tilted. These devices are also very sensitive to temperature. In the forward bias mode, care would have to be taken to ensure that the average current is kept constant.

References

3.1 C. Kittel, *Introduction to Solid State Physics*, 5th ed. (Wiley, New York, 1976).

3.2 W.B. Joyce and R.W. Dixon, Appl. Phys. Lett. 31, 354 (1977).

3.3 G.H.B. Thompson, *Physics of Semiconductor Laser Devices* (Wiley, Chichester, England, 1980).

3.4 H.C. Casey, Jr., and M.B. Panish, *Heterostructure Lasers* (Academic, New York, 1978), Part A.

3.5 D. Bimberg, D. Mars, J.N. Miller, R. Bauer, and D. Oertel, J. Vac. Sci. Technol. B 4, 1014 (1986).

3.6 R.E. Williams, *Gallium Arsenide Processing Techniques* (Artech House, Dedham, Massachusetts, 1984).

4. The current-voltage characteristics of RTDs

In this chapter we describe our understanding of the current-voltage characteristics of RTDs, which in turn gives us the ability to optimize them. In the first section, the trends predicted by the ballistic transport model are summarized. Some of the limitations of the model are discussed in the second section. The third section describes the use of ionized impurities as a design parameter. The fourth section describes the use of the ballistic model for RTD design.

4.1 Calculating the current-voltage characteristics of an RTD

Due to the nature of the RTD crystal structure, it is usually a good approximation to separate the variables along the growth direction and perpendicular to it. The one dimensional wavefunction solution can be used to find the transmission coefficient strictly as a function of longitudinal energy of the incident electron. The integration of the expression for current density is an integral over the longitudinal energy[4.1, 4.2]:

$$j = \frac{4\pi m^* kT}{h^3} \int_0^\infty dE_x \, |T(E_x, V)|^2 \ln\left\{\frac{1+\exp((E_f - E_x)/kT)}{1+\exp((E_f - E_x - eV)/kT)}\right\}, \quad (4.1)$$

where q is the magnitude of the electronic charge, E_l is the electron energy in the direction of tunneling, E is the total electron energy, f is the Fermi-Dirac distribution function, V is the applied voltage, h is the Planck constant, $E = E_l + E_t$, in which electronic energy transverse to the tunneling direction, E_t, is quantized, and $|T(E_l,V)|^2$ is the tunneling probability as a function of longitudinal energy and applied voltage.

Using the above expressions, the current-voltage characteristics of a RTD can be modelled. The local fluctuation in charge density is given by using a one dimensional Poisson equation solver along the direction of growth[4.3]. Up to 150 points are selected for

each bias condition of interest, including points at each hetero-interface. The discontinuity of the quazi-Fermi level is taken to be at the first hetero-interface.

The potential is approximated by assuming an equal potential between each two adjacent points[4.4], with an abrupt step or interface at each point as shown in figure 4.1. The quantum region is taken to start within the heavily doped emitter layer so that any band bending before the heterointerface is accounted for in the transmission coefficient. The plane wave matching conditions are invoked at each interface to find the transmission coefficient as described in the previous section. Equation (4.1) is integrated using a Newton-Coates 8 panel quadrature method (Quanc8) to find the current-voltage characteristics of the device being simulated. The quantum region is taken to start within the heavily doped emitter layer so that any band bending before the heterointerface is accounted for in the transmission coefficient. The numerical integration is carried out for electron kinetic energies ranging from 0 to at least 500 meV, the upper limit depending on the specifics of the problem. If the upper limit is set correctly, than any contribution from the "thermionic" current component is also included in the model.

The method described above is very effective in simulating the coherent part of the current voltage characteristics of resonant tunneling devices[4.5]. The main transmission resonance is accurately predicted, as are subsequent transmission resonances. The lowest energy resonance is typically much sharper than the higher energy (and less confined) resonances. In general, the simulation results will show much more extreme values of the peak to valley ratio than are observed in the actual device. This is largely due to the effects left out of the simulation.

The quantitative agreement of the model for peak current density is good from the The peak position is usually estimated correctly within 50%, and much of the discrepancy is due to series resistance effects in the physical device. As a result, the measured peak voltage is almost invariably higher than the predictions of the coherent transport model. The peak current is usually correctly predicted to within a factor of 2, which is very good considering the fact that monolayer fluctuations can have a very strong effect on current densities in a tunneling device.

For a given barrier composition, thicker barriers tend to result in a strong decrease in the

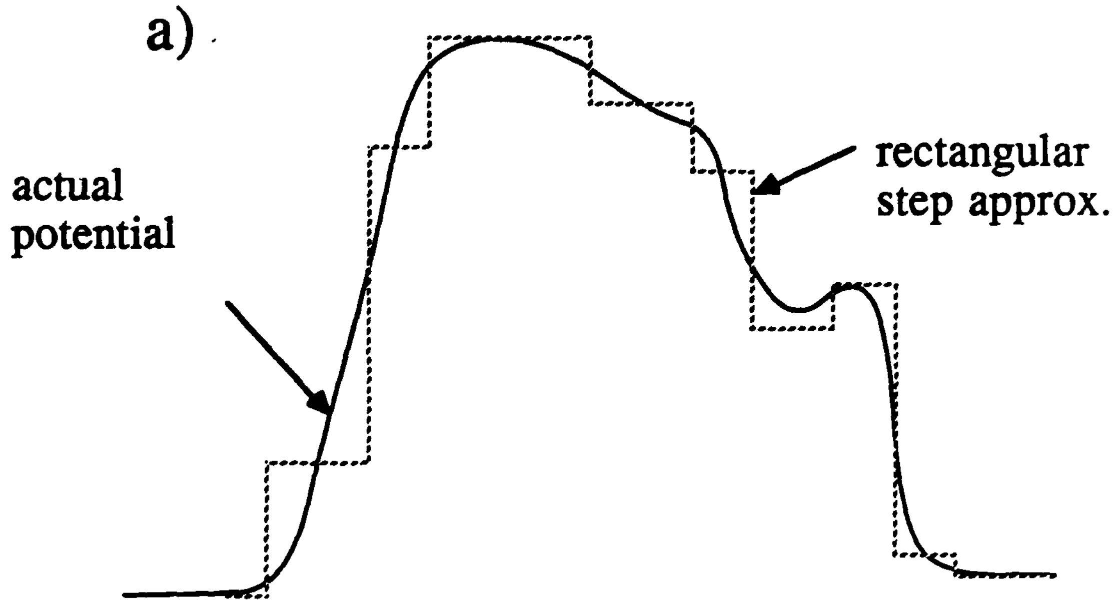

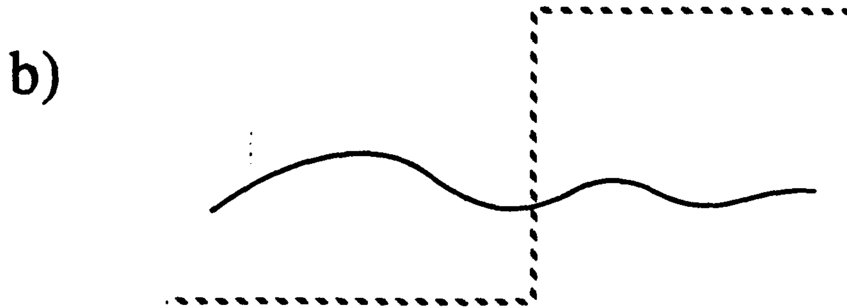

Figure 4.1 - It is shown how an arbitrary potential can be approximated as a series of rectangular steps in a), and the wavefunction A exp(kx)+B exp(-kx) can be matched at each interface in b), note that A, B and k can be complex and are generally different in each segment.

resonant current with only minor effects on the resonant voltage, as shown in figure 4.2. An increase in the potential offset at a heterointerface due to a changing barrier composition can have a similar effect. In the GaAs/AlAs materials system this is done by increasing the Al composition of the barrier alloy. As a result, it is possible to design different barriers of similar transparencies by choosing the correct combinations of barrier composition and thickness.

The width of the quantum well has a strong influence on both the bias needed to reach the resonant condition and the resonant current density as shown in figure 4.3. Similar to the case of the quantum barriers, increasing the width of the well decreases the resonant current in an exponential fashion. As a result of this similarity, even a slight miscalibration in crystal growth can have a huge impact on the resonant current as the change in resonant current, due to changes in both wells and barriers is complimentary instead of offsetting. For this reason, the factor of two agreement between the coherent model and the measured current density shown in figure 4.4 can be considered to be very good.

The undoped collector spacer has it's principle influence on the amount of bias needed to achieve resonance and on the quality of the device itself. Larger undoped collector spacers require larger biases across the RTD to achieve resonance, due to the voltage drop across these spacer layers. There is little effect on the magnitude of the resonant current from changing the collector spacers, however, the valley current tends to decrease with increasing collector spacer due to improvements in crystalline quality and a reduction in scattering effects[4.5].

The contact doping of a RTD influences the resonant bias condition and the resonant current as shown in figure 4.5. The Fermi energy was calculated assuming complete ionization of the dopants and using the Joyce Dixon approximation[4.6]. In general, increasing the contact doping will have a small effect on the resonant current once the incident spread of electrons is similar in width to the width of the transmission resonance. Changes in the contact doping also change the band structure in the emitter part of the RTD, thus complicating the predicted trends in the resonant current.

4.2. Limitations of this method

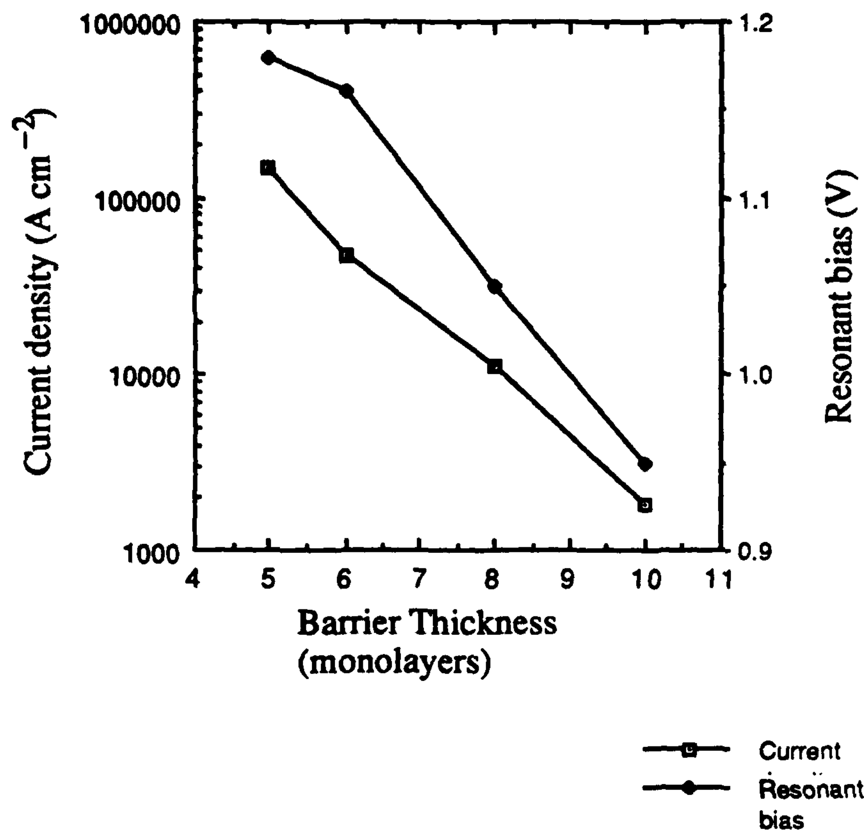

Figure 4.2 - The simulated dependence of the resonant current density and the resonant bias is plotted against barrier thickness for a device with 1E18 contact doping, a 100 Å first spacer layer, a 700 Å second spacer layer, and a 45 Å well operating at room temperature. Note that changing the barrier thickness by even a few monolayers has an exponential effect on the resonant current with only a minor impact on the resonant bias.

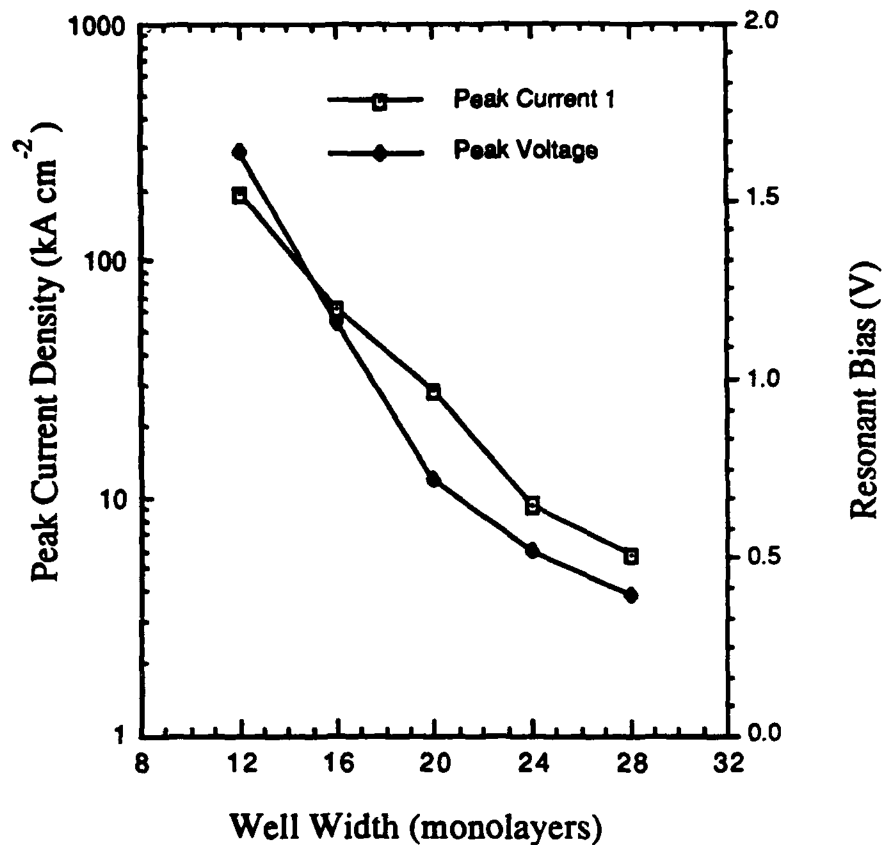

Figure 4.3 - The variation of the resonant bias and resonant current density with changing well width is shown. The devices simulated had 6 monolayer barriers, 100 Å emitter spacer layers, 700 Å collector spacer layers, and a contact doping of 1×10^{18} cm^{-3}. The variation in current density with well thickness is similar to, but not as strong as the variation with barrier thickness. The change in resonant bias is due to the shift in the energy of the resonant state with changing well width.

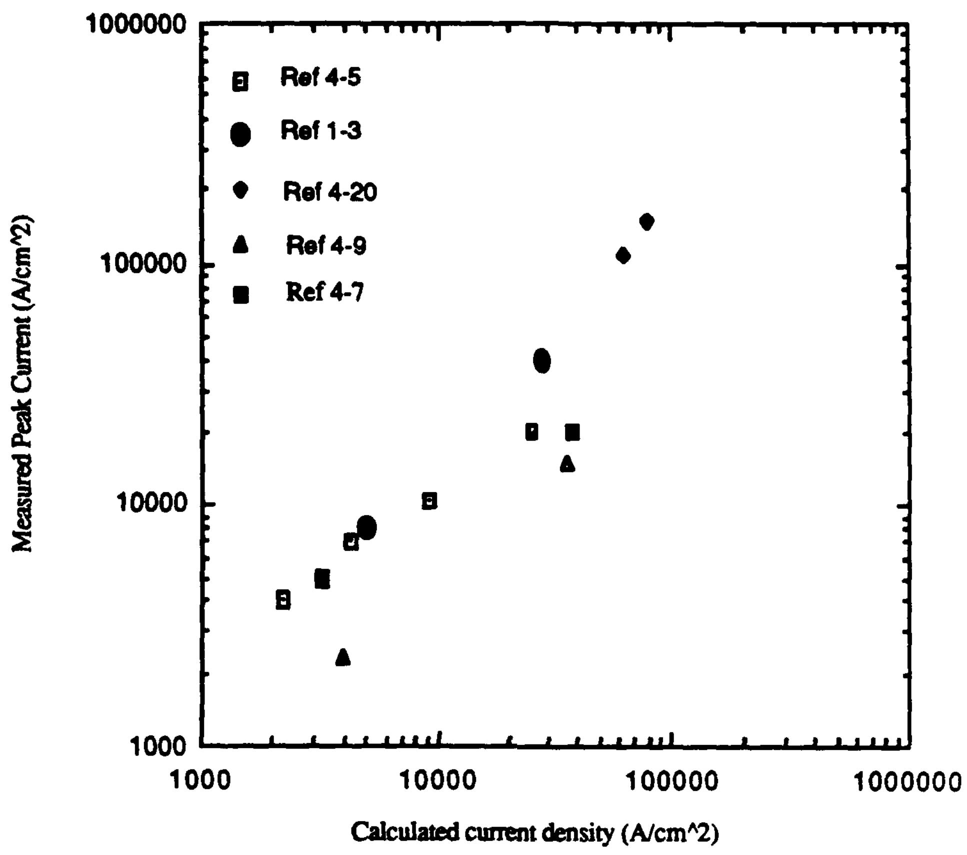

Figure 4.4 - The coherent model is compared against putblished data covering two orders of magnitude. The coherent model agrees with the published data to within a factor of 2, which is good agreement considering the strong dependence of the tunneling current on the well and barrier thicknesses.

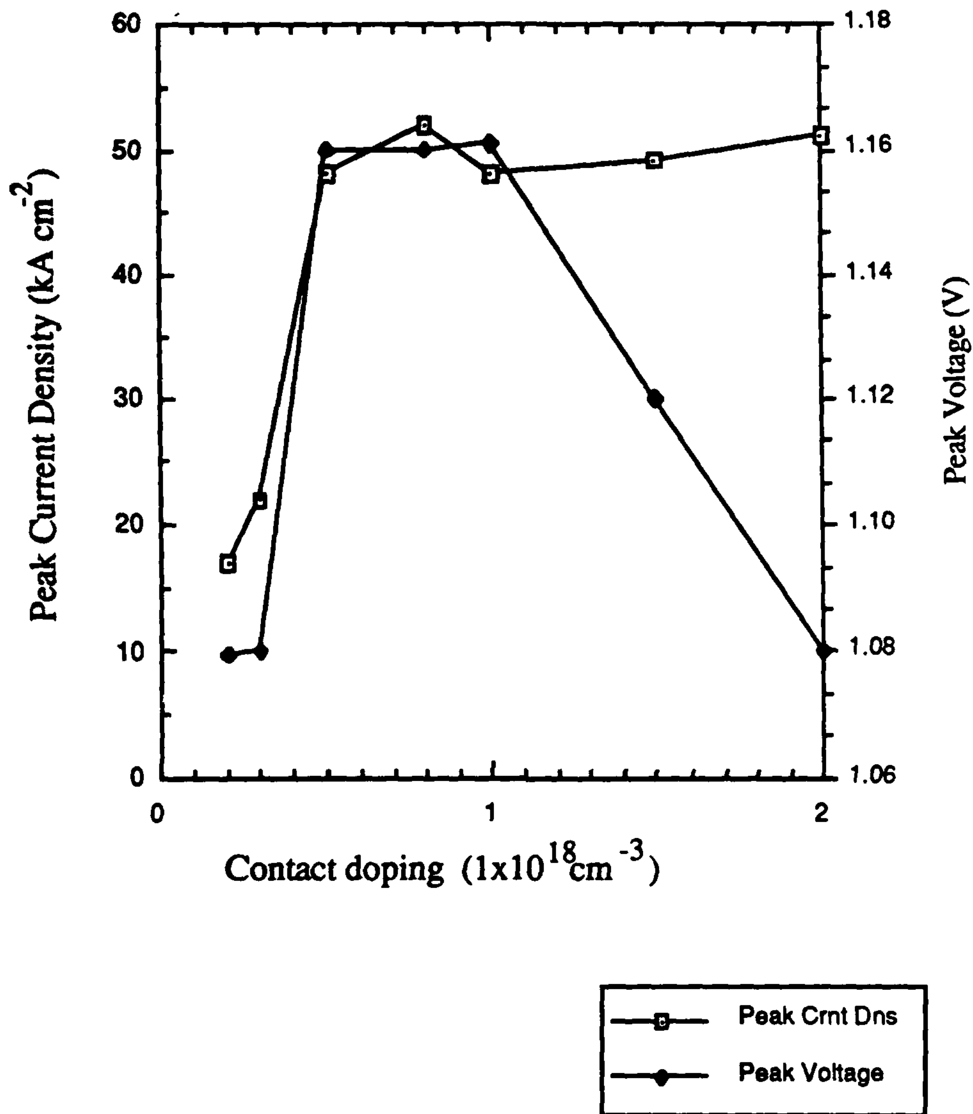

Figure 4-5 - The resonant current density and resonant bias for a device with varied contact doping. The barriers were chosen to be 6 monolayers, the well was 16 monolayers, and the undoped spacer layers were 100 Å on the emitter side and 700 Å on the collector side respectively.

Knowledge of the effects which break down this analysis are crucial to making this model a useful tool for analysis and extrapolation of experimental results.

There are several factors which limit the applicability of the coherent transport model for double barrier resonant tunneling diodes, all of which are potential contributors to the deviations between the model and experiment. Any physical process which disturbs the condition of transverse momentum conservation will violate the separation of variables condition upon which this model is based[4.7]. Several such processes are possible, including; elastic scattering from ionized impurities[4.7], phonon scattering[4.8], scattering due to interface roughness[4.9], scattering due to alloy non-uniformity, and changes in the transverse effective mass.

As quantum transport is assumed through the undoped spacer layers, scattering or phonon emission in the emitter spacer may cause additional valley currents or even additional resonances. Thus undoped or lightly doped ($<10^{17}$ cm^{-3}) spacer layers of more than a few hundred Å on the emitter side can make this model ineffective. The effects of elastic impurity scattering and accumulation layer formation can contribute to the valley current, as can scattering due to impurities on the collector side.

Inelastic scattering events should not change the resonant current of the device to first order if the incoming electrons have an energy distribution which is broader than the width of the resonance. They may, however, alter the background non-resonant current of the device near room temperature. Phonon emission within the well of the DBRTD can add to the valley current by reducing the longitudinal energy of the incident electron such that it falls into an energy within the transmission resonance. A similar effect may result from phonon emission in the accumulation layer which is on the emitter side of the device.

Elastic scattering events can cause a degradation in the current-voltage characteristics of a RTD. The most common sources of elastic scattering are ionized impurity centers and interface roughness. Interface roughness scattering is a major source of the reduction of the peak to valley ratio of RTDs. In general, scattering events which change the longitudinal momentum component will effect the current-voltage characteristics, while scattering events which change the longitudinal momentum should not impact the I-V

characteristics.

The possibility of electrons scattering into the X valley[4,10], specifically at a hetero-interface, must be considered in order to fully understand the behavior of these devices. This problem is very important in the case of AlAs tunnel barriers within a GaAs crystal due to the relatively small energy difference between the longitudinal X valley of AlAs and the Γ valley of GaAs. A substantial amount of work has been done on the problem of Γ - X band mixing, but a model of these effects which is both computationally accessible and physically reliable has yet to be developed.

Qualitatively, it is known that such effects can decrease the peak to valley ratio of a RTD. It is also known, that as the X barrier is lowered, tunneling through this pathway becomes more significant . It is reasonable to conclude, therefore, that higher energy electrons incident on the tunneling barrier are more likely to be affected by Γ - X band mixing than the lower energy electrons. Thus, to avoid a low peak-to-valley ratio it is important to keep the resonant state below the X-point energy in the barrier. It is also important to keep the spread of incident electron energies, (and thus the emitter doping,) low enough so that when the bottom of the conduction band is at resonance, the electrons at the Fermi energy are below the X-point. From these considerations we arrive at a rough limitation on the applicability of the RTD model:

$$E_f + E_{res} < E_x$$

where E_f is the difference between the Fermi energy and the conduction band minimum, E_{res} is the resonant state energy at the resonant bias, and E_x is the energy of the X point of the collector barrier.

The use of the effective mass approximation and the envelope function to determine electron transport through the structure may also introduce deviations from experimental measurements for several reasons. The use of non-parabolic band structure only partially addresses this issue, notably in our implementation of the model. The possibility of dissimilar Bloch wavefunctions is not considered in the envelope function approximation, and this could lead to breakdown of this model if it were an important effect; apparently this is not the case in the GaAs/AlGaAs material system. For thin tunneling barriers, the effective mass approximation based on bulk parameters must fail, presently the limit for

this breakdown is assumed to be 2-5 monolayers. In addition, the change of effective masses at the hetero interface violates the separation of variables condition; this effect is thought to be small, but it becomes more important as the transverse momentum increases. At this time, however, the above assumptions are probably the best approach for making a model which is both computationally accessible and relatively accurate.

4.3 Ionized impurities as a design parameter

Ionized impurities are a crucial element of RTD operation, yet they can be detrimental to the device because any ionized donor is in fact an elastic scattering center. As the location and quantity of ionized impurities can be controlled by MBE, it is important to their understand their effect on the tunneling current of the device. Large undoped spacer layers surrounding the double barrier structure shift the resonant bias of the RTD through band bending effects. This shift can be controlled and is thus a design parameter for adjusting the resonant bias. The presence of dopants near the RTD, however, have been shown to reduce the peak to valley ratio of resonant tunneling devices. Therefore, it is important to study the effect of elastic scattering within and near the well of a resonant tunneling diode. The ballistic model outlined in the does not include this effect, as the major impact of elastic scattering is to break the separation of variables condition upon which the ballistic model is based.

Several workers have investigated the role of elastic scattering events in resonant tunneling devices, including the effect of ionized impurities in the layers immediately outside of the device[4.11] as well as scattering due to interface roughness. The use of doping impurities within the RTD itself has been intentionally implemented and also occurs unintentionally due to background impurities and diffusion; in addition, related structures are being proposed and implemented which include ionized impurities in the wells and barriers of the device.

4.3.1 Elastic scattering in momentum space and scattering assisted transport

In order to understand the role of elastic scattering centers placed in a barrier system

with a one dimensional potential profile V(1), we separate the problem into a longitudinal part, (motion perpendicular to the quantum barriers) and a transverse part (motion parallel to the barriers). In the absence of scattering, transverse momentum is conserved, thus we can define the quantities $E_t \equiv h^2 k_t^2/(2m^*)$ and $E_l \equiv E - E_t - V(1)$ which can be thought of as energies parallel and perpendicular to the wells, respectively; where h is Plank's constant, m* is the effective mass of the electron in GaAs, and E is the sum of the kinetic and potential energies of the electron. Total kinetic energy is conserved in an elastic scattering event, however, the quantum barrier structure removes three dimensional symmetry resulting in the possibility of momentum transfer between the longitudinal and transverse directions. Elastic scattering events which conserve transverse energy, as depicted in figure 4.6a, will not change the I-V characteristics of the device. On the other hand, elastic scattering events which transfer momentum from the longitudinal to the tranverse direction, or vice versa, break the condition of transverse energy conservation upon which ballistic transport models are based.

Scattering allows transitions though the DBRTD which would otherwise be improbable. A specific example of this is the scattering of an electron by impurities in the well of a DBRTD; such scattering could allow an electron which has an incident longitudinal momentum higher than the transmission resonance, to scatter into a longitudinal momentum within the resonant band as shown in figure 4.6b, thus resulting in the transmission of the electron through the double barrier structure. We define the resonant band as the electron states within the full width at half maximum of the resonant state (in longitudinal energy). The net effect of such scattering events is to add current in the valley part of the I-V characteristic, as most incident electrons would have a small transmission probability with no scattering under this bias condition. It is not clear what the effect on the current is near resonance, but it is probably small as the most likely result is to scatter from one resonantly transmitted state to another, resulting in little change to the resonant current.

4.3.2 Experiment with varied well dopings

In order to measure the effect of scattering centers in the well on the I-V characteristics of DBRTDs, four double barrier structures were grown with different dopant profiles using

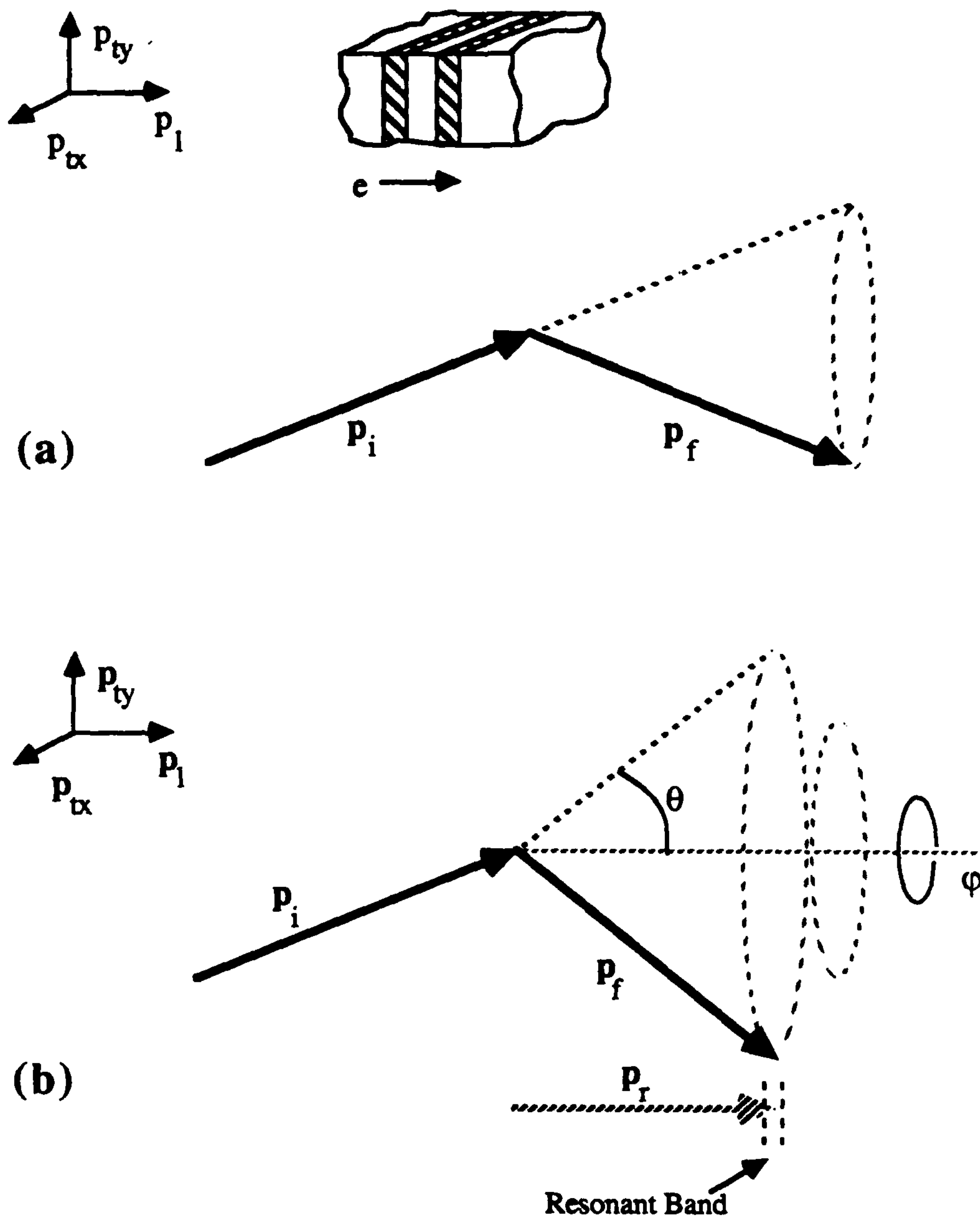

Figure 4.6 - Elastic scattering events which conserve longitudinal energy (a), and do not conserve longitudinal energy (b) are shown in momentum space.

molecular beam epitaxy (MBE) in a modified Varian Gen II. The control sample had an undoped well region, the second sample had 16.7Å of 1.0^{18} cm^{-3} Si n-type doping centered in the well, the third was similarly doped with Be and the fourth sample had 16.7 Å of alternating Si and Be doping to create a highly compensated doping effect in the well's center. As the doped wells have n-type, p-type and compensation doping, the effects of band bending on the I-V characteristics should be separable from the effects of elastic scattering events in the well.

The growths consisted of a 2500 Å GaAs buffer layer with 10^{18} cm^{-3} Si doping, an 80 Å undoped GaAs spacer layer, an undoped 60 Å $Al_xGa_{1-x}As$ (x=0.3) barrier, a 50 Å GaAs well with the aforementioned doping profiles, a 40 Å undoped $Al_xGa_{1-x}As$ (x=0.3) barrier layer, a 40 Å undoped GaAs spacer layer, a 1500 Å GaAs capping layer with 10^{18} cm^{-3} Si doping, and a GaAs/InGaAs superlattice non-alloyed ohmic contact[9,10]. The barriers were intentionally grown to be asymmetric at zero bias so that at the resonance bias condition, the reflections from the two barriers would be nearly equal, thus enhancing the peak resonance current. A 20 second growth interruption was performed 20 Å before the quantum barrier system, in order to smooth the first interface, while minimizing the accumulation of any impurities at the interface itself.

All of the structures were processed by wet etching mesas to isolate the devices as shown in figure 4.7. The mesas were designed to be squares ranging from 2-20 µm on a side with outward slopes along the direction of the interconnect metallization. Large area mesas of 100 µm and 500 µm on a side were also fabricated. A nickel-gold-germanium alloy was deposited to provide ohmic contact to the region surrounding the mesas. SiO_2 was deposited by plasma enhanced chemical vapor deposition to passivate the structure. The alloyed ohmic contacts were subsequently annealed at 450° C for 30 seconds in forming gas. Buffered HF was used to etch openings for the interconnect metallization to connect the ohmic contacts and the bonding pads. Dice from each wafer were mounted and bonded on to 24 pin carriers which were submerged in liquid nitrogen for low temperature measurements.

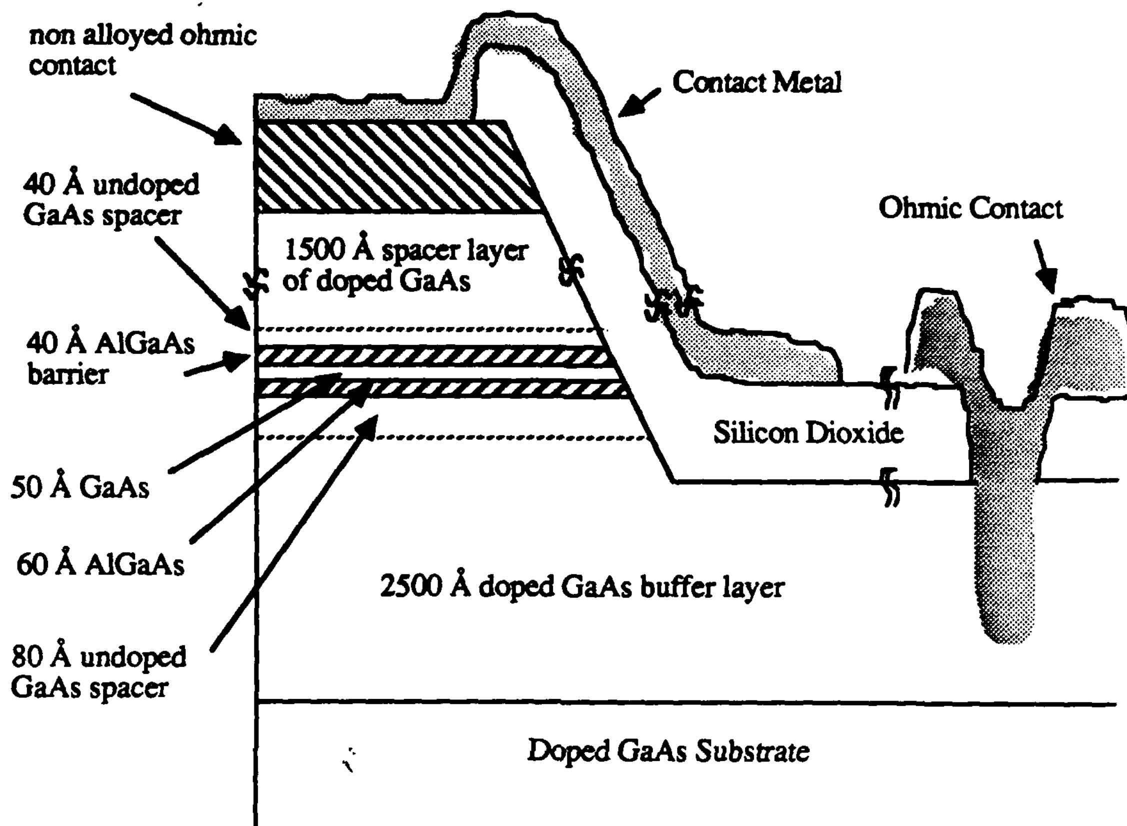

Figure 4.7 - Schematic of processed RTD's for the elastic scattering experiment. The process sequence includes mesa isolation, ohmic metalization, rapid thermal anneal, oxide deposition, etching of contact holes and interconnect metal deposition. The 50 Å GaAs well contains varied dopant types for the purpose of a systematic comparison.

4.3.3 Measurements at 77 K

Measurements at 77 K revealed a systematic shift in the voltage of the peak current. This systematic shift can be explained by band bending effects due to the ionized impurities placed in the well of the device. Ionized p-type dopants in the well bend the conduction band such that the resonant state is raised, thus increasing the amount of bias necessary to achieve resonance. On the other hand, ionized n-type dopants cause an accumulation outside the barriers and bend the bands lower inside the well, thus lowering the resonant state.

Lowering of the peak to valley ratios occurred in all of the devices with doped wells, and it is not clear from the experimental results if the peak to valley ratio decreased due to an increase in the valley current or a decrease in the peak current.

The above results are compared with predictions from the coherent model. A Fermi energy of 0.056 eV above the conduction band and a temperature of 77 K were assumed. The results of this calculation are shown in figures 4.8 and 4.9. We can see that the predicted peak and valley voltages show good agreement with the data in figure 4.9 The model predicts a higher peak to valley ratio for doped devices due to band bending effects, in contradiction with the experimental results. Thus, the experimentally observed reduction in peak to valley ratios in the doped devices cannot be attributed band bending, and must be explained by scattering from the impurities which were intentionally placed in the well, or some other effect. It is not clear from the experimental results whether this reduction in peak to valley ratio is due to a decrease in the peak current or an increase in the valley current due to the large standard deviation of the current densities in the samples (the peak to valley ratios were more consistent).

4.3.4. Discussion

Elastic scattering centers in the well of a DBRTD can change the voltage and magnitude

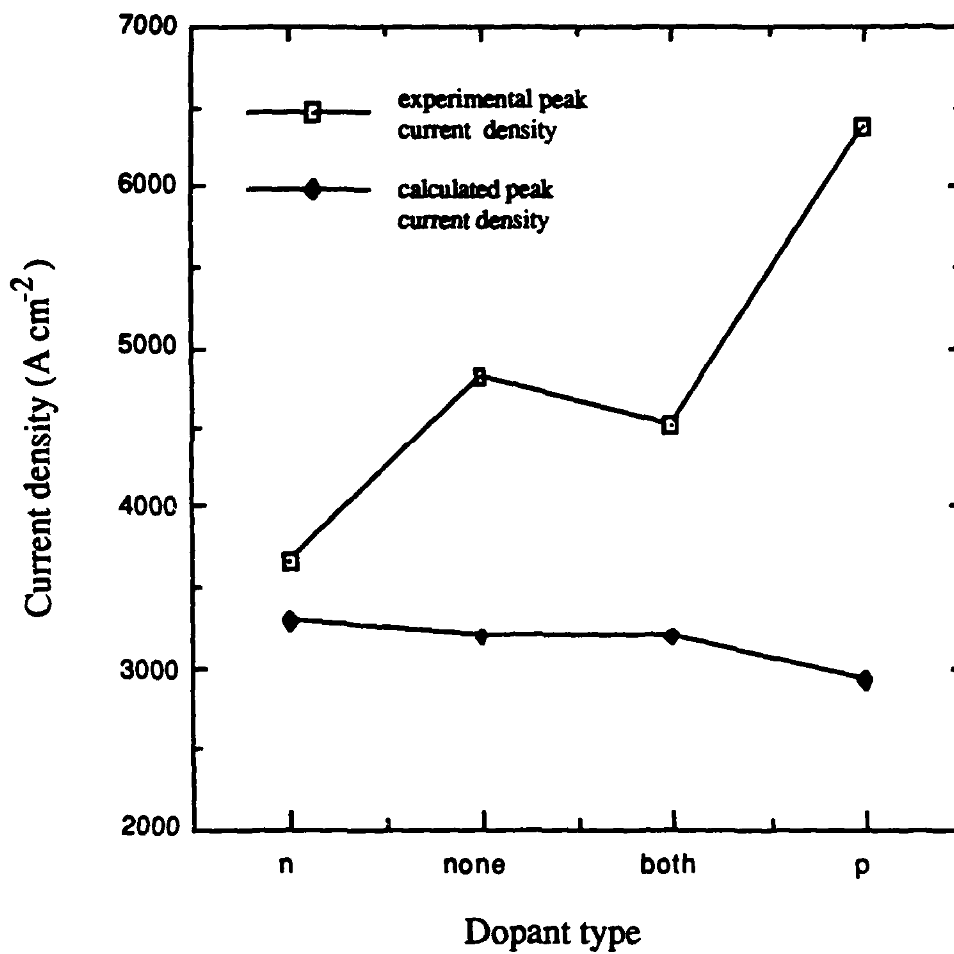

Figure 4.8 - The change in peak current density with well doping is also not correctly predicted by the coherent transport model. It is not clear if this is due to fluctuations in the thickness of the RTD's or a more sophisticated effect.

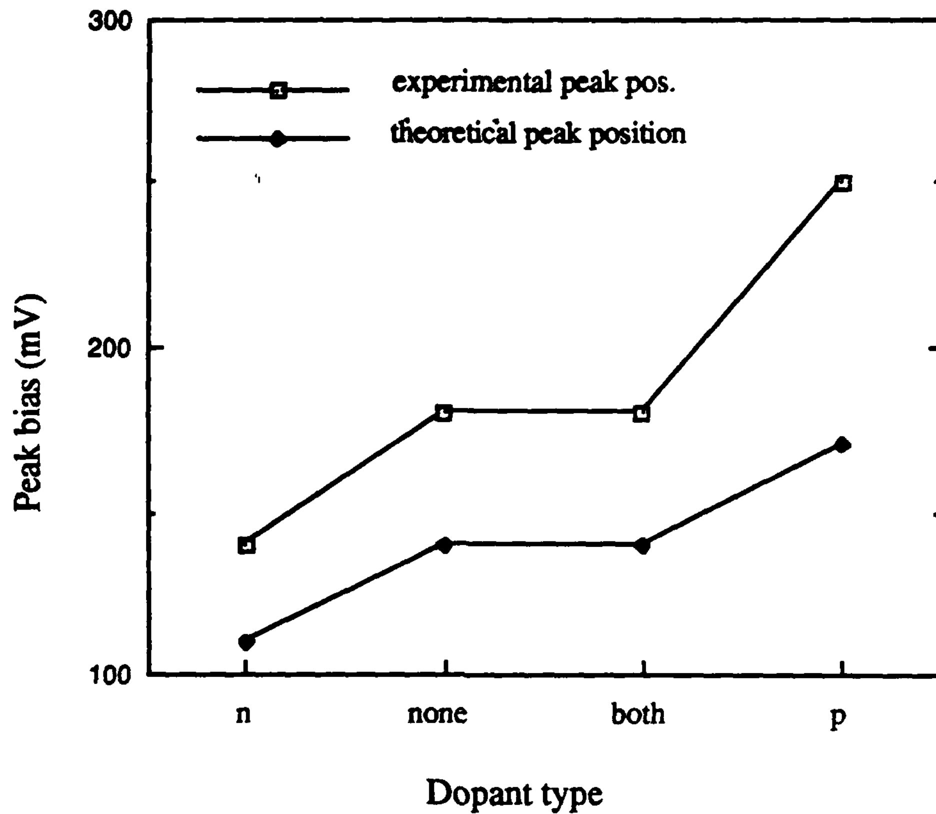

Figure 4.9 - The bias needed to achieve resonance with different types of well doping is compared with the predictions of the coherent transport theory. The model correctly predicts the shift in resonant bias with impurity type. Notice that the predicted resonance occurs at a lower applied voltage than in the experiment, this is a typical result.

of features in the I-V characteristics of resonant tunneling devices. Elastic scattering centers in the barriers of a DBRTD show similar effects, with the devices with additional doping in the barriers showing a shift in the resonant voltage and a degradation of the peak to valley ratio[4.12]. These experiments show that elastic scattering can reduce the peak to valley ratio of a DBRTD, however, it is also apparent that a measured quantity of these centers will not destroy the negative differential resistance of these devices.

These results are also applicable to ionized impurities in the barriers and immediately adjacent contact layers. The ionized impurities in this experiment (which were intentionally placed in the well of the device) occupy an area of roughly 250 Å on a side. For an electron experiencing quantum barriers and a well on the order of 50 Å in the longitudinal direction, the displacement of the scattering center by this amount should not matter much if the electron can be thought of as 100 Å to the side of the impurity. The relative insensitivity to longitudinal placement of the the impurity is exaggerated by the non-localized nature of an unscreened Coulomb potential and the electron wave packets themselves. Thus, ionized impurities will weakly degrade the peak to valley ratio of an RTD if placed in the barriers or within a few nanometers of the quantum structure.

These results have important implications for RTD design. Combined with the studies on scattering centers immediately outside the device, these results emphasize the importance of using undoped spacer layers around a resonant tunneling device. Clearly, ionized impurities serve to degrade the current voltage characteristics from what the ballistic model predicts and their use in the well and barriers of the device is only advisable as a last resort in RTD design, changing the resonant bias can be accomplished by changing the well composition or thickness, as well as changing the surrounding undoped spacer layers. The thickness of spacer layer to use surrounding the double barrier structure is a more difficult question. This is due to the fact that larger spacer layers are beneficial for the purpose of reducing elastic scattering, however, the peak to valley ratio and peak current density predicted by the ballistic model degrade with larger emitter spacer layers. Thus in choosing the correct spacer layers, the tradeoff between ideal transport characteristics and the effects of elastic scattering must be considered. The relatively large number of donors used in the

wells of these devices show that the use of lightly doped regions surrounding the spacer layers, may be a reasonable approach to achieving good band structures yet minimizing impurity scattering effects.

4.4 The design of RTDs

At present, our ability to compute all of the physical phenomena which occur in a RTD is incomplete, however, use of the available information at this time yields useful information about RTD design. The energy of the resonant state is very well understood and physical measurement of the resonant bias condition is well predicted by the model. The current density due to coherent transport through the double barriers is also accurately predicted. The processes which are not addressed in this model tend to cause degradation of RTD operation (as measured by the peak to valley ratio) and thus the RTD should be designed such that these effects are minimized.

The peak current of the RTD is largely determined by the width and magnitude of the transmission coefficient. By making devices with a larger peak transmission coefficient and a wider transmission resonance, it is possible to make devices with higher peak current densities. The transmission coefficient is determined by both the energy difference and thickness of the quantum barriers. In general, it is best to achieve a desired transparency by using thin high barriers, as such barriers are more effective in blocking current flow due to more energetic electrons.

The choice of quantum well width is best determined by considering several physical phenomena. It is important to get good separation between the resonant states in order to achieve a high peak to valley ratio. In addition, the desired resonant state must be higher in energy than the Fermi level on the collector side if a large difference in electron distributions, and thus large current density, are to occur. Narrow quantum wells may be used to achieve this, however, the use of a narrow quantum well raises the lowest resonant state and this increases the amount of bias needed to reach resonance. As a result, increased current flow through the X valley, and increased accumulation layer formation, may result in the degradation of the peak to valley ratio of the device. In addition, interface scattering effects become more important with narrower wells due to the increased resonant

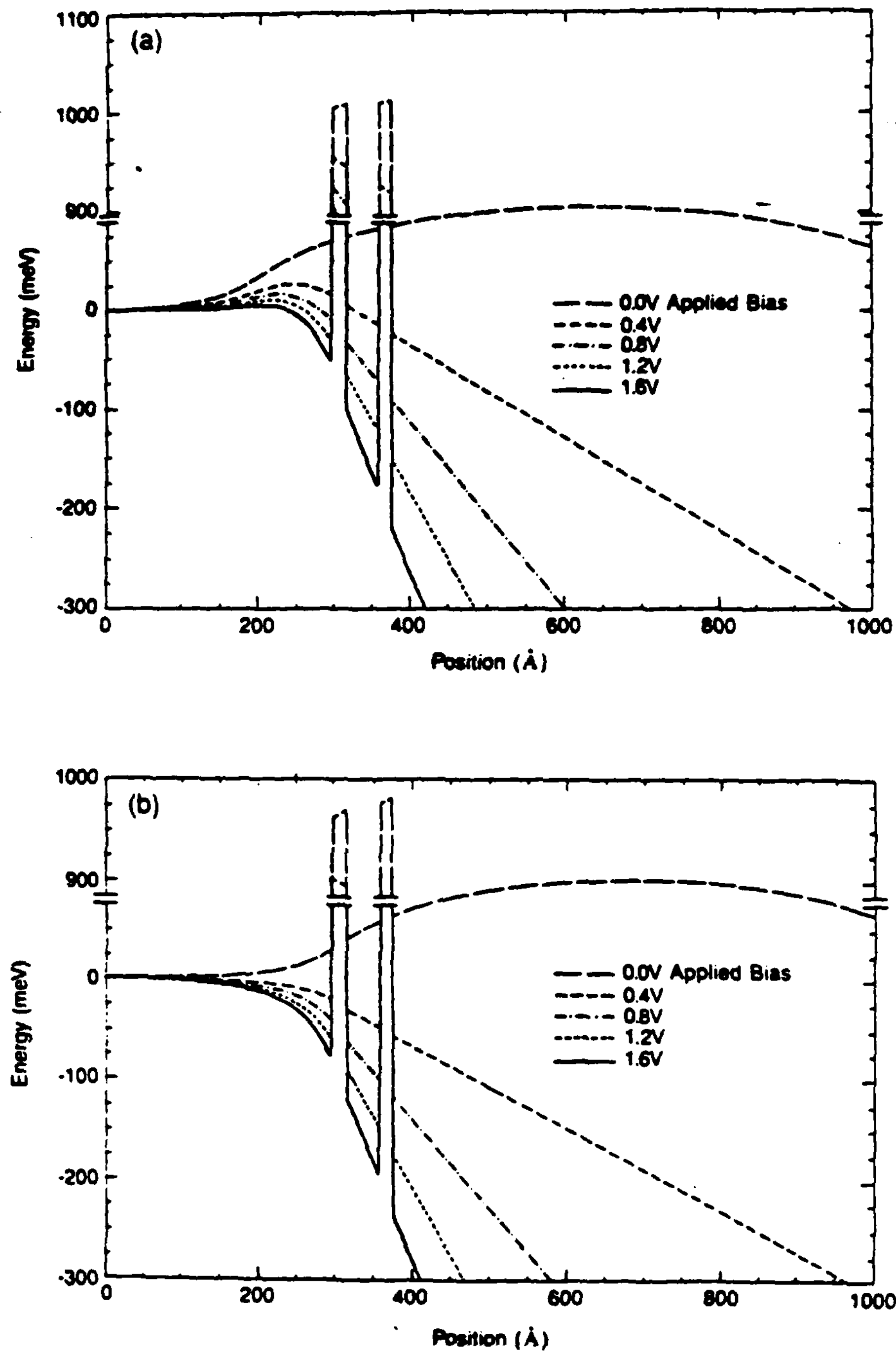

Figure 4.10 - The Poisson equation solution on the conduction band minimum is for resonant tunneling structures with a 700Å undoped second spacer and (a) no undoped emitter spacer and (b) A 100Å undoped emitter spacer. The 100Å emitter spacer helps reduce the effects of accumulation layer formation and impurity scattering.

energy splitting from monolayer fluctuations in the barriers. As a result, wells of approximately 50 Å have been used for ground state resonance effects.

Emitter doping is a parameter that can be used to directly trade off peak current density and peak to valley ratio for an RTD. As doping is increased, the energy distribution of electrons convolved with the transmission resonance is increased. This has two effects, first the peak current density is increased, however, as the spread of incident electron energies rises so does the possibility of tunneling through higher resonances, thus valley current is also increased.

In addition to determining the tunneling current by setting the Fermi level, doping concentrations change the tunneling current due to band banding effects. By the proper use of an undoped spacer layer on the collector side of the RTD, it is possible to reduce capacitance, and increase the peak to valley ratio by quenching the accumulation layer on the emitter side at little cost to the peak current density as shown in figure 4.10. Also, the degradation of the peak to valley ratio due to elastic scattering effects is reduced. The use of an undoped spacer also acts as a lever which changes the amount of bias needed across the device in order to achieve resonance. By correcting choosing barrier thickness, well width, emitter doping, and undoped spacer- layers; we were able to design the high performance RTDs descriped in the next chaper.

References:

4.1. C.B. Duke, Tunneling in Solids, Solid State Suppliment 10.

4.2. R. Tsu and L. Esaki, Appl. Phys. Lett. 43, 588 (1983).

4.3. M.S. Lundstrom and R. J. Schnelke, IEEE Trans. Electron Devices ED-30, 1151 (1983).

4.4. M.O. Vassel, J. Lee and H.F. Lockwood, Journal of Applied Physics 54, 5206 (1983).

4.5. Shunichi Muto, Tsuguo Inata, Hiroaki Ohinishi, Naoki Yokoyama and Satoshi Hiyamizu, Japan Jour. Appl. Phys., 25 (7), L577 (1986).

4.6. Herbert Kroemer, Journal of Applied Physics, 52, 873 (1981).

4.7. E. Wolak, K.L. Lear, P.M. Pitner, E.S. Hellman, B.G. Park, T. Weil, and J.S. Harris Jr., Appl. Phys. Lett. 53 (3), 201 (1988).

4.8. T. Weil and B. Vinter, Appl. Phys. Lett. 50, 1281 (1987).

4.9. M. Tsuchiya and H. Sakaki, Appl. Phys. Lett. 49, 88 (1986).

4.10. David Yuk Kei Ko and J C Inkson, Se[illegible]nd. Sci. Technol. 3, 791 (1988).

4.11. S.K. Diamond, E. Ozbay, M.J.W. Rodwell, D.M. Bloom, Y.C. Pao, E. Wolak and J.S. Harris, Electron Device Letters, 10, 104 (1989).

4.11. Hiroaki Ohnishi, Tsuguo Inata, Shunichi Muto, Naoki Yokoyama, and Akihiko Shibatomi, Appl. Phys. Lett. 49 (19), 1248, 1986.

4.12. E. Wolak, K.L. Lear, P.M. Pitner, B.G. Park, E.S. Hellman, T.Weil, J.S. Harris Jr., and D. Thomas, SPIE no 943, 36, 1988.

Chapter 5

RTD's for High Speed Electronics

The unique shape of the RTD current-voltage curve allows these devices to be used for voltage step generation. Voltage steps can either be used directly or differentiated in simple microwave circuits to create pulses.

In addition to performing useful circuit functions, RTD pulse generators provide an excellent system to examine the large signal switching performance of RTDs. Brown *et al.* have extensively investigated the small signal operation of RTDs in oscillator structures [5.1]. They have measured oscillations up to 200 GHz, however power levels have been limited to .2 μW (-37 dBm). Assuming a 50 Ω load, this is a 3 mV voltage swing which is only a small fraction of the total negative differential resistance region. In contrast, RTD pulse forming structures have voltage swings across the entire negative differential resistance region with voltage swings as high as 500 mV.

There has been a significant amount of research on using resonant tunneling devices in transistor structures [5.2,3]. The characteristic negative differential transconductance make these transistors well suited for digital applications. In digital applications, the device operation is large signal as the device switches on or off. Processing difficulties have limited device performance to low frequency operation. By studying the simpler to fabricate diode pulse forming structures, insight can be gained into the speed of resonant tunneling transistors.

In this chapter the circuit for generating voltage steps with RTDs will be presented. An exact expression for the rise time will be developed and then two estimates to the rise time will be examined. The chapter will conclude by evaluating previous research on RTD pulse forming.

5.1 Present State of the Art

Step and pulse forming circuits are used for sampling, triggering and TDR (Time Domain Reflectometry) applications. Each of these applications has slightly different requirements for the step or pulse generator. For sampling applications a sampling diode needs to be turned on for a brief instant and this requires a short pulse of sufficient amplitude to turn on the diode. For TDR applications a short rise time is needed and spurious oscillations or noise on the pulse should not be present. Table 5.1 lists the current state of the art for voltage step generation.

Technology	Rise time (ps)	ΔV (V)	Comment
Step Recovery Diode	35	10	
Esaki Diode	20	.300	
Josephson Junction [5.4]	2.1	.005	Cryogenic operation
Nonlinear Transmission Line [5.5]	1.6	6	Chip area intensive

Table 5.1: State of the Art

With a rise time less than that of Josephson junctions and a voltage step as high as step recovery diodes the NLTL (NonLinear Transmission Line) appears to be the best technology for pulse formations. For sampling applications a sampling head with a 130 GHz bandwidth has been demonstrated using NLTLs [5.6]. The disadvantage of this technology is that it requires a transmission line on $GaAs$ which is a significant fraction of a centimeter in length. This is costly to fabricate due to the chip area used and potential yield problems.

The NLTL produces the fastest pulses, however it is not a threshold device and is unsuitable for triggering application. A trigger is a decision making element used

in a oscilloscopes and timing circuits. A trigger circuit requires a threshold device which has two input levels with sudden transitions in the output. The most widely known trigger circuit is the Schmitt-trigger which employs transistors. The fastest trigger circuits available use high-speed Esaki diodes [5.7]. Resonant tunneling diodes have a similar current-voltage curve as Esaki diodes and should be equally well suited for triggering circuits. RTDs will not compete with NLTLs for pulse forming applications, however if RTDs can demonstrate faster switching times than Esaki diodes then these devices will be commercially viable.

5.2 Pulse Forming Circuit

A resonant tunneling diode step forming circuit is shown in Fig. 5.1a. The structure consists of a 50 Ω coplanar transmission line with a RTD connected in shunt from the cente conductor of the line to ground at the midpoint of the line. The transmission line and RTD are monolithically integrated on chip.

For the step forming circuit, the transmission lines are matched in their characteristic impedances and can thus be replaced by the matched impedance. The two parallel impedances and voltage source can now be replaced by their Thevenin equivalent and the circuit shown in Fig. 5.1b is obtained. In practice, 50 Ω transmission lines are used to match the lines to available wafer probes and microwave sources, this means the effective load resistance across the RTD will be 25 Ω.

The output voltage of the circuit, V_{out}, is equal to the voltage across the RTD. For calculating the switching time, the switching time of the voltage V_1, internal to the device series resistance, is more readily calculated. The output voltage is related to V_1 and V_{in} through

$$V_{out} = V_1 \frac{R_l}{R_l + R_s} + V_{in} \frac{R_s}{R_l + R_s} \tag{5.1}$$

If the series resistance, R_s, is small in comparison to the load resistance, R_l, then the output switching waveform is the same as the internal voltage, V_1. However, if the series resistance cannot be neglected then in the output waveform a fraction of the input waveform will feed through. The feed through of the input waveform

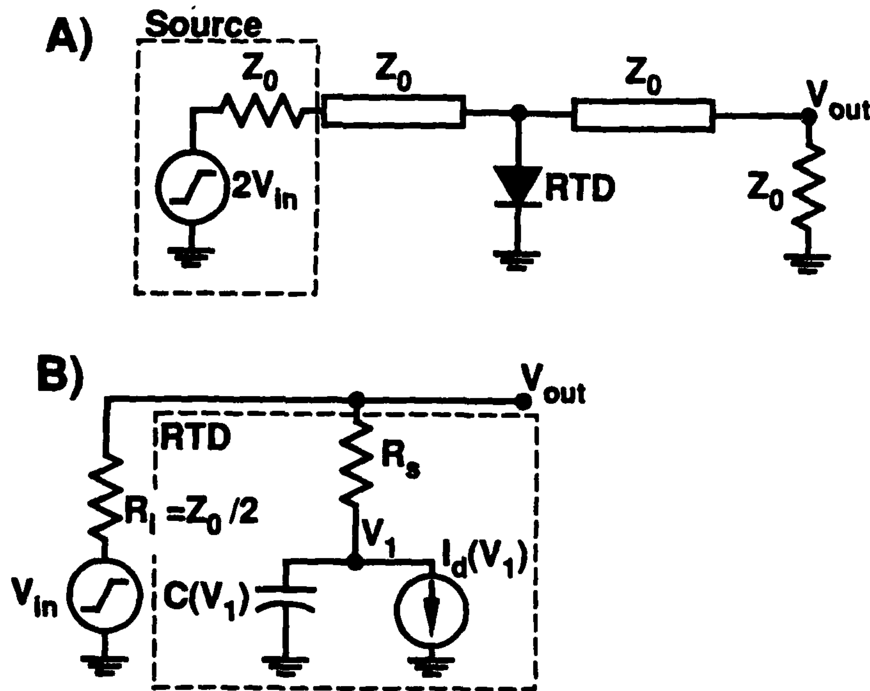

Figure 5.1: (a) High speed RTD pulse forming circuit. The RTD is shunted to ground across a 50 Ω transmission line. In (b) the matched transmission lines and source has been replaced by a Thevenin equivalent, and the equivalent circuit for the RTD is used.

results in a degrading the of shape of the output waveform. Pedestals will appear on the output and the switching transition will occur over a smaller percentage of the total output voltage swing. The degradation of the output waveform should be minimized as much as possible but it is not critical for most applications. This should be contrasted with the situation for oscillator applications where the series resistance limits the maximum frequency of oscillation.

The large signal switching operation of RTDs is illustrated in Fig. 5.2. The device I-V curve is shown along with the load line at two different bias points. The operating point of the device is given by the intersection of the load line with the device I-V curve. Because of the negative differential resistance, there may be several crossing points and the operating point will depend on previous biasing

history. If the source voltage is increased from 0 to V_{in1} then the device operating point will be **A**. A small increase in the source voltage will move the load line upwards and the operating point will shift to **B**. Assuming the series resistance is negligible, a voltage step of magnitude $V_f - V_p$ will be observed at the output.

If the operating point of the device is set to point **B** and then reduced down to zero there will also be a voltage transition across the device as the load drops below the valley. The analysis which will be developed in the following sections applies equally well to the resetting voltage transition. This will not be emphasized because typically the current-voltage curve is not as ideal for the reverse direction and risetimes are typically 1-2 times longer than in the forward direction.

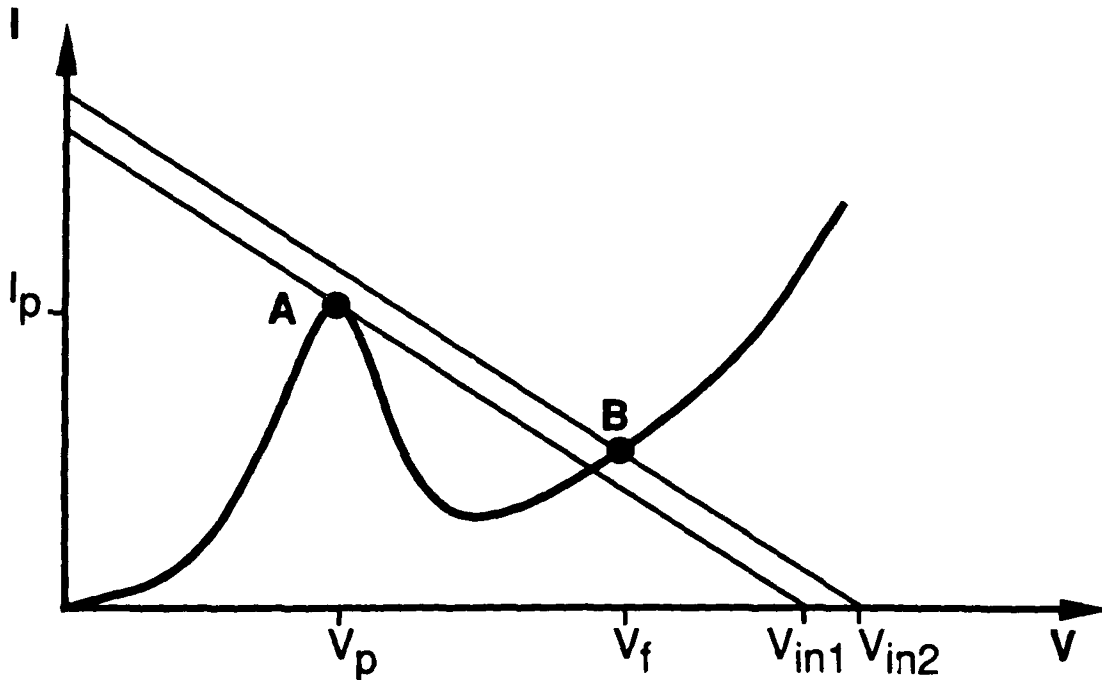

Figure 5.2: Large signal switching behavior or a resonant tunneling diode is observed as the device switches from state **A** to state **B**.

To estimate the time for switching it is easiest to track the charge stored on the device capacitance. As the voltage across the device changes by an incremental amount δv, charge is stored on the capacitor of magnitude $\delta Q = C(v) \cdot \delta v$. The

current which is available for charging this capacitance is the difference between the current which the load can supply, $I_l(v)$, and that which is conducted through the device, $I_d(v)$. This current is indicated as the shaded region in Fig. 5.3. The time to change the voltage across the device by an incremental amount δv is:

$$\delta t = \frac{C(v)\delta v}{I_l(v) - I_d(v)} \tag{5.2}$$

The 10-90% rise time can be obtained by integrating the above expression.

$$T_{rise} = \int_{V_p+.1(V_f-V_p)}^{V_f-.1(V_f-V_p)} \frac{C(v)}{I_l(v) - I_d(v)} dv \tag{5.3}$$

From the previous equation it is apparent that the switching time is directly related to the device capacitance. The PVR (Peak to Valley Ratio) has traditionally been the accepted figure of merit for RTD evaluation however as shown in Fig. 5.3 it is apparent that improving the PVR above two will have minimal impact on the switching time. For example, if the peak to valley ratio is improved from 2 to 100 then the area of the shaded region will increase by a factor of two and the switching speed will be reduced by only a factor of two. Increasing the device current density has the effect of scaling Fig. 5.2 upwards. The current available for charging the device capacitance is thus directly related to the current density and the switching speed is inversely related to current density.

Eq. (5.3) is an exact expression for the rise time, however this form can be difficult to work with and does not emphasize key device parameters. In the following two section approximations to the above integral will be made and their validity will be discussed.

5.3 Piecewise Linear Approximation

To estimate the switching time, the $I_d(v)$ in Eq. 5.3 is approximated by two linear segments (Fig. 5.5) of slope $(1/R_n)$ in the negative resistance region and slope $(1/R_d)$ in the region past resonance. R_n is then the average negative differential resistance. The rise time can then be calculated [5.8].

$$\frac{T_{rise}}{|R_n|C} = \left(\frac{x}{x-1}\right) \ln\left[\frac{10(x+y)}{x(x-y)}\right] + \left(\frac{xy}{x-y}\right) \ln\left[\frac{10(x+y)y}{x(x-y)}\right] \tag{5.4}$$

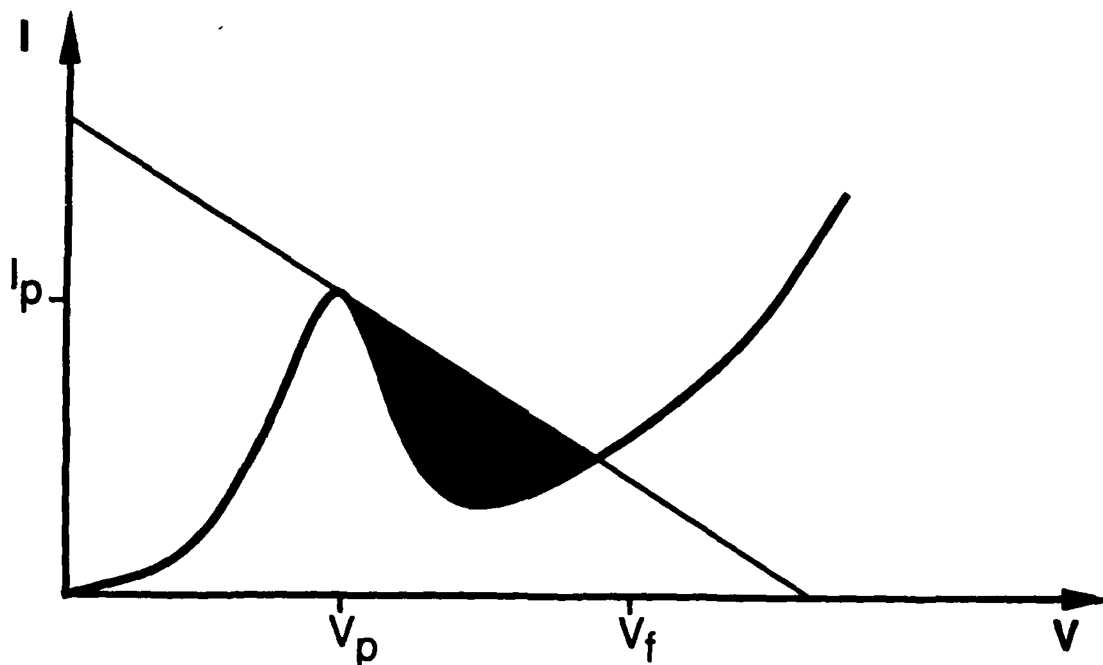

Figure 5.3: The current which is available for charging the device capacitance is shown in the shaded region.

where $y \equiv R_d/|R_n|$ and $x \equiv R_l/|R_n|$. The product $|R_n|C$ limits the device switching speed. Fig. 5.6 plots the normalized rise time $(T_{rise}/|R_n|C)$ as a function of R_l for several $R_d/|R_n|$. As R_l approaches the $|R_n|$, $(x \rightarrow 1)$ the rise time increases dramatically because of a decrease in the current available for charging up the RTD capacitance. As the load impedance increases $(x \rightarrow \infty)$, $(V_f - V_p)$ increases, increasing the rise time. The minimum switching time is achieved when the device I-V curve is V shaped, $R_d = |R_n|$, and the load is a current source $x \rightarrow \infty$. Under these circumstances as minimum switching time of $4|R_n|C$ is obtained. If $R_d \neq |R_n|$ then the minimum rise time cannot be achieved, however, if the load can be adjusted to be roughly 2.5 times the average negative resistance, $R_l = 2.5|R_n|$ then for almost any ratio of R_d/R_n a minimum rise time of $4 - 5|R_n|C$ can be obtained.

Table 1 gives the risetimes, calculated from Eq. 5.4 with R_l optimized for minimum rise time, for several RTDs discussed in the literature. The capacitance was

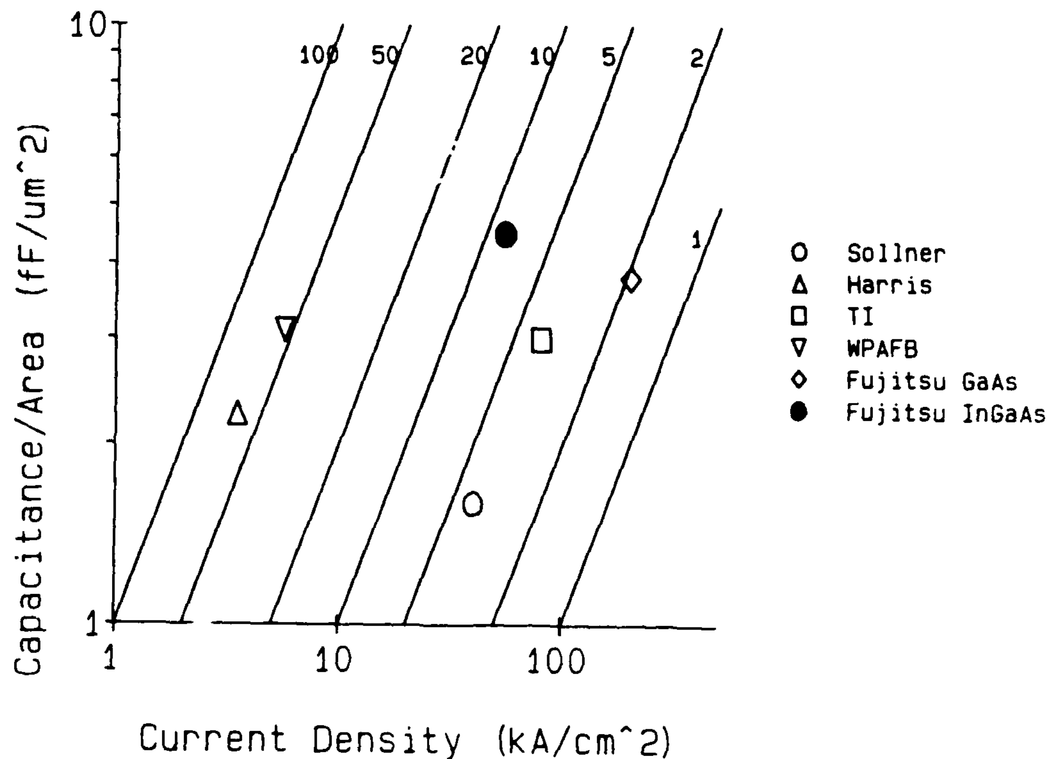

Figure 5.4: Capacitance and current density for the best reported devices. The diagonal lines are lines of constant $\Gamma = I_p/C$. The best devices are on the lower right

estimated from published growth parameters at the bias voltage corresponding to the peak current. A minimum obtainable rise time of 4.6 ps is predicted, however from the current-voltage curve for this device it would have a voltage swing of only 100 mV and would be unsuitable for circuit applications. For devices which have a voltage swing in excess of 300 mV, the minimum predictable rise time is 12 ps.

In practice 50 Ω transmission lines must be [illegible] to match to microwave sources. The means that R_l cannot be varied and is fixed at $R_l = 25\ \Omega$ for the parallel transmission line structure. To obtain the minimum rise time with $R_l = 2.5|R_n|$, different size devices are fabricated and thus $|R_n|$ is varied until $|R_n| = 10\ \Omega$.

For switching applications it is the product $|R_n|C$, where R_n is the average negative differential resistance, which determines the switching speed. Unlike oscillator applications, the appropriate figure of merit is $|R_n|C$ or $f_t = 1/2\pi R_n C$.

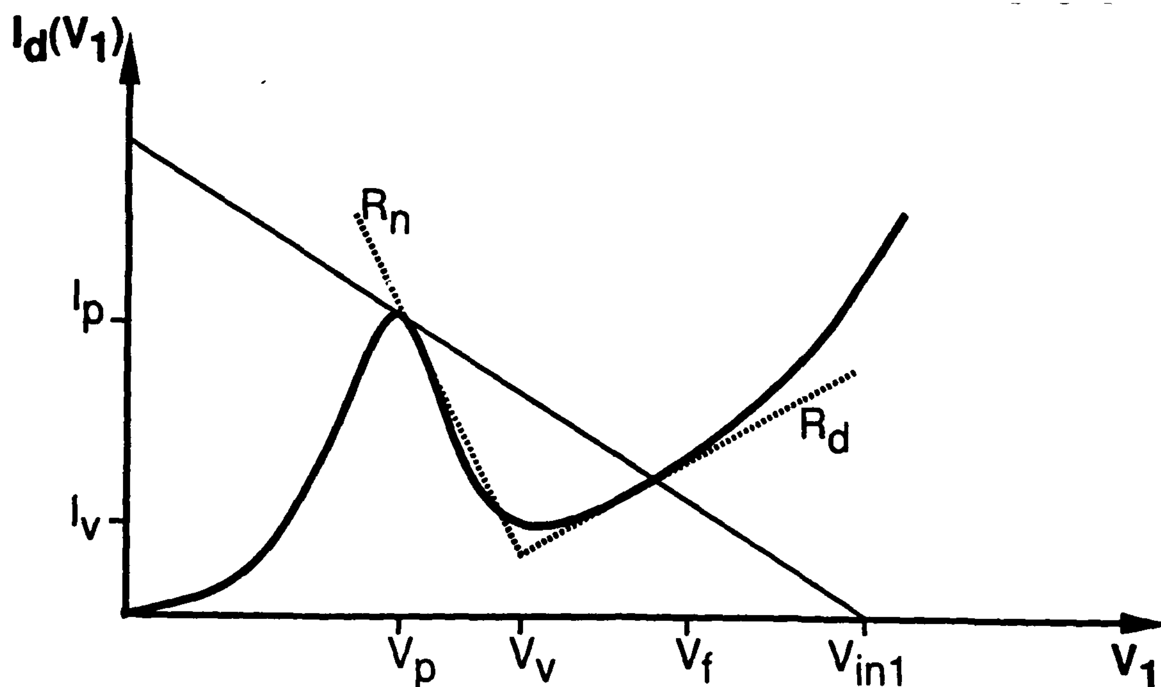

Figure 5.5: Load line for piecewise linear approximation

5.4 Static I-V curves

Fig. 5.7 shows typical room temperature and 77 °K static I-V curves for the first generation of devices fabricated. The devices exhibit current densities in the range of .9-1.3$\times 10^5$ A/cm^2 with PVR's from 2-2.5. At 77 °K, current densities increase to 1.5-1.7$\times 10^5$ A/cm^2 with PVR's from 5.2-6.1. These devices are unique, for the *GaAs/AlAs* system, in their high current densities and simultaneous high PVR's.

The negative differential resistance region is not discernible in the static I-V curves. Other researches have proposed that this structure is due to quantum mechanical oscillations in the device [5.12]. However as discussed by Sollner and Lui, this structure is most likely attributable to device negative resistance oscillating with the measurment fixture and is not due to any quantum mechanical effect [5.13,14].

The I-V curve for these devices is asymmetric, as is to be expected from the

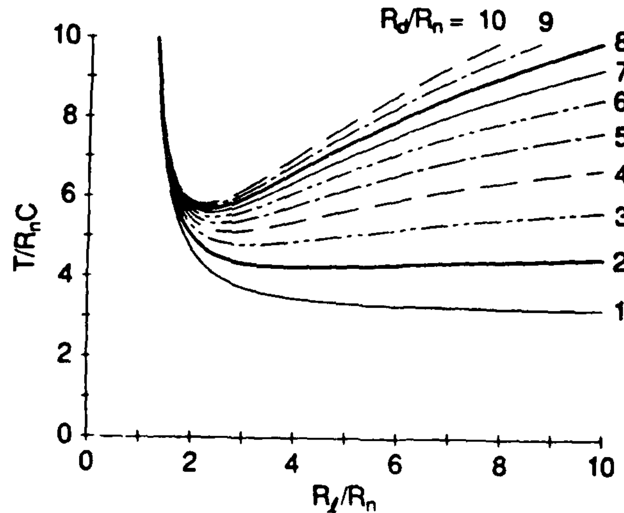

Figure 5.6: Normalized rise time is plotted as a function of different ratios of load resistance to device negative resistance for various shapes of current voltage curves. Minimum obtainable rise time is typically 4-5 $R_n C$

asymmetric growth. The devices were designed to operate under forward bias. A 50 Å spacer was placed on the emitter side and a 700 Å spacer layer is on the collector side of the double barrier structure. Under reverse bias less voltage is dropped across the depletion layer and resonance is reached at a smaller voltage. The current density is significantly reduced because the large undoped region before the barriers limits the electron density at the barriers.

GEN1 devices can generate up to 3.25 $mW/\,\mu m^2$. This proved to be a significant problem and for devices larger than 40 μm^2 the top ohmic contact melted through the device and shorted out the double barrier region. In the second generation of devices, GEN2, the reduced length of the depletion layer shifted the resonance voltage down to lower voltages. Fig. 5.8 shows the static I-V curves for two typical GEN1 and GEN2 devices at room temperature. The power dissipation was reduced

by 40% for the GEN2 and devices larger than 70 μm^2 were successfully tested.

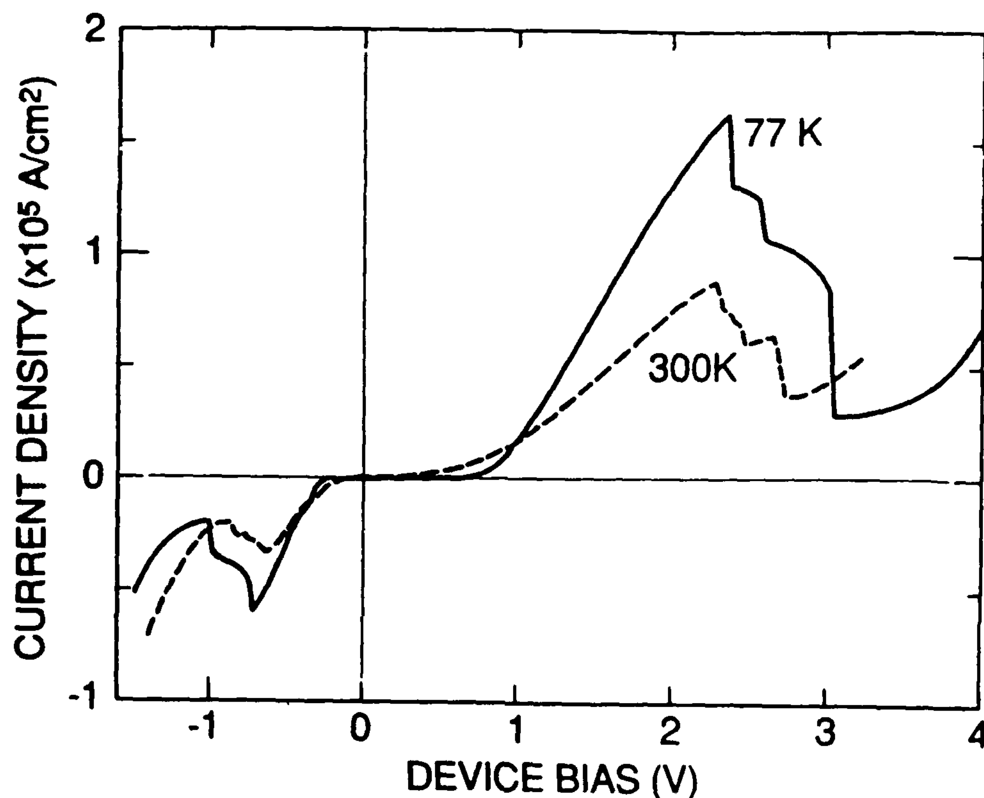

Figure 5.7: Static I-V curves for typical GEN 1 devices at room temperature and 77 K.

5.5 Scattering Parameter Measurements

Scattering parameter (or S parameter) measurements were performed. For these experiments, a transmission line structure was not used, but instead devices were connected directly to a pad compatible with microwave probes. Using microwave probes allowed testing the device equivalent circuit at frequencies up to 26.5 GHz.

The equivalent circuit for S parameter measurements is shown in Fig. 5.9.

Generation 1 and Generation 2 Devices

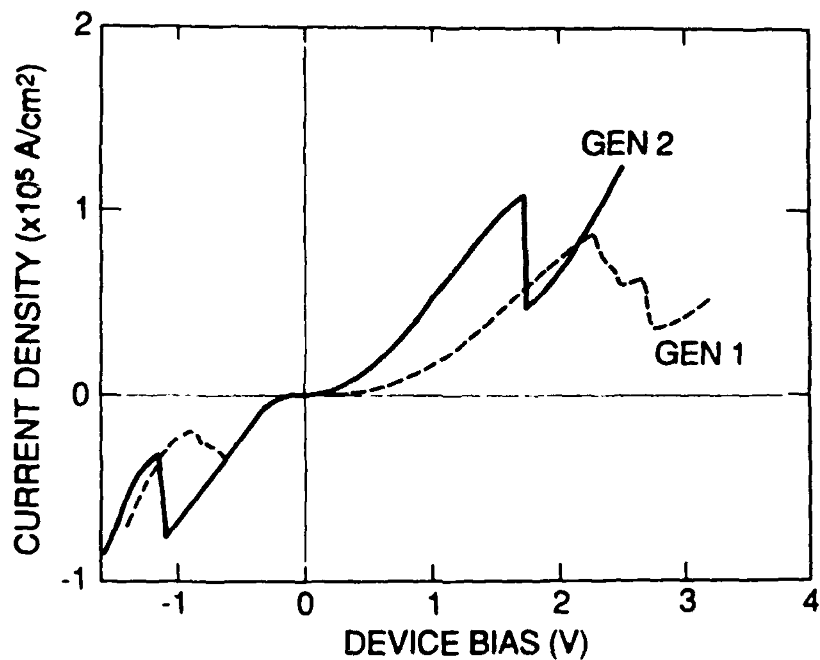

Figure 5.8: I-V curve for GEN1 and GEN2 devices

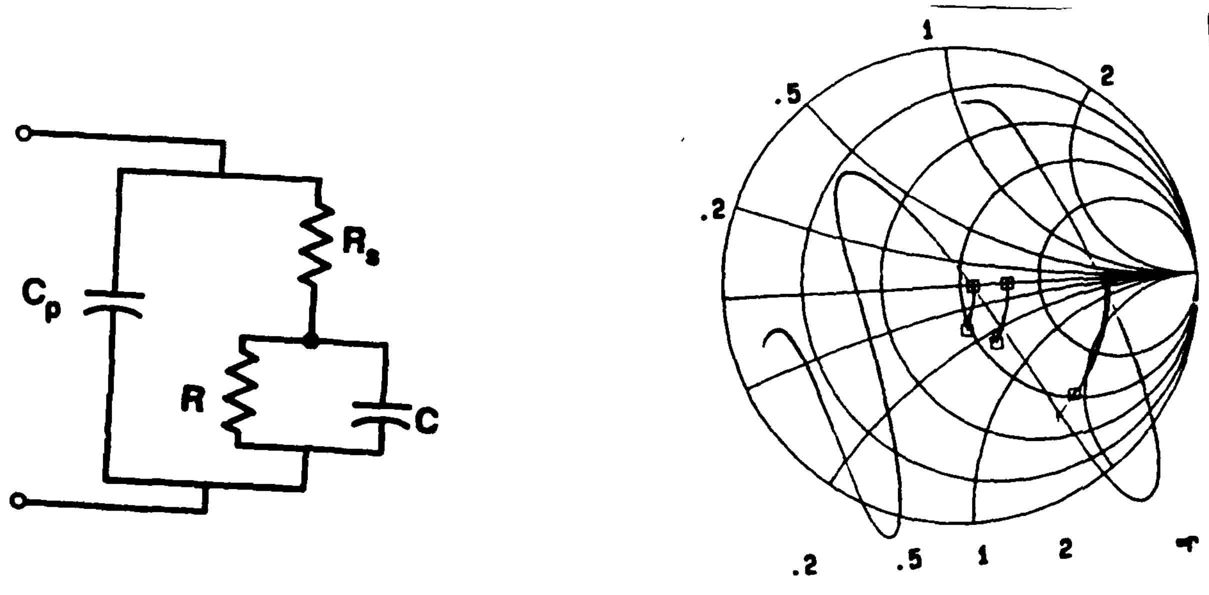

Figure 5.9: Equivalent circuit for S parameter measurements

The contact resistance was measured as $r_c = 4.6 \times 10^{-7}\ \Omega - \mathrm{cm}^2$ from on wafer transmission line test patterns. The series resistance for these devices is estimated at $223\ \Omega -\ \mu\mathrm{m}^2$.

The device capacitance was estimated at $1.3 fF/\ \mu\mathrm{m}^2$ based on the spacer layer thickness. Because of the high doping outside of the undoped spacer layer, the capacitance should be relatively independent of the bias voltage.

The small signal device resistance, R, is a function of the bias point. At each bias point where the device S parameters were measured, R was estimated by fitting a tangent line to the I-V curve at that bias point. The series resistance is then subtracted from the resistance of the line to obtain the small signal device resistance.

The pad capacitance was obtained by two different methods. Blank pads were fabricated on wafer. S_{11} measurements of these blank pads showed that they were capacitive in nature with a capacitance of 32 fF. To check this the capacitance for a number of different size devices was measured as a function of device area. The total capacitance was plotted as a function of area, extrapolating this plot to devices of zero area yielded a capacitance of 32 fF.

S parameter measurements were performed at 0.5, 1.0 and 1.5 volts. All of these bias points are before the negative differential resistance region. It would have been desirable to measure S_{11} within the negative differential resistance region, however this was not possible. Device oscillations made the data unreliable through portions of the NDR region. In addition the I-V curve is highly nonlinear in this region and S parameters are only valid if the I-V curve can be treated as linear. Typically, for nonlinear regions, the power is reduced until a linear operation is achieved, however this was not observed for the RTDs even at the lowest power settings.

S_{11} measurements were performed on a 15 $\mu\mathrm{m}^2$ device. The independently, experimentally measured circuit parameters are listed in table 5.3.

Fig. 5.10 plots the measured S parameters at three different bias points. Also plotted in the figure are the theoretically calculated S parameters. These parameters were calculated from the data listed in table 5.3. It should be emphasized that there is no fitting between the theory and experiment. Each of the four circuit parameters were measured independently from the device S parameter measurements. The close

match between theory and experiments means that the proposed circuit model for these devices is accurate to at least 26.5 GHz and that the calculated device parameters are relatively close to the actual device parameters.

S Parameter Measurements and Theory

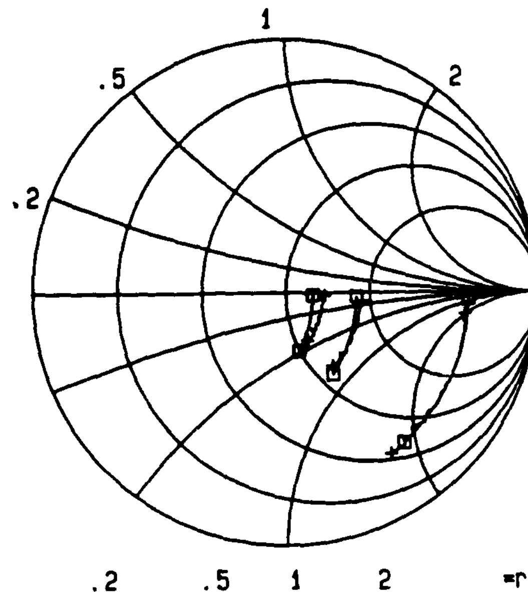

Figure 5.10: S_{11} measurements and theory at three bias point. The experimental data curves have plus mark endpoints. The predicted curves have box endpoints.

5.6 Switching Measurements

5.6.1 Expected performance

The S parameter measurements validated the RTD equivalent circuit model and at this point the device performance can be predicted for oscillator and switching applications. In oscillator circuits, the maximum frequency of oscillation or f_{max} is

the appropriate figure of merit. f_{max} is given by:

$$f_{max} = \frac{1}{2\pi|R_n|C}\sqrt{\frac{|R_n|}{R_s} - 1} \tag{5.5}$$

where R_n is the value of the negative resistance in the NDR region. Oscillations in the NDR region make determination of R_n impossible however R_n can be approximated by the average negative resistance $R_n^{avg} = (V_{peak} - V_{valley})/(I_{peak} - I_{valley}) - R_s$.

For switching applications the product $|R_n^{avg}|C$ is the appropriate figure of merit, with the minimum switching time equal to $4 - 5|R_n^{avg}|C$. Often $f_t = 1/2\pi|R_n^{avg}|C$ is used as the figure of merit for switching applications. Table 5.6.1 lists the figures of merit for each generation of device.

5.6.2 Electrooptic Measurements

Electrooptic sampling measurements were performed on a number of devices [5.15]. In practice a 2 GHz sine wave and DC bias was applied to the input transmission line. If the device is to be reset, the amplitude of the sine wave must be sufficient to switch the load line above the peak voltage, V_p and move the load line back down to less than the valley voltage V_v. Fig. 5.11 illustrates the expected waveforms for a sinusoidal input voltage. For the devices tested, and the applied sinusoidal voltages, the switching transition were typically less than 70% of the total output voltage swing.

Fig. 5.12 is a typical electro-optically measured pulse. Switching times of 6-10 ps were measured with voltage swings of 400-500 mV. The measured risetimes are 2 ps greater than the theoretically predicted minimum rise time. The difference between the estimated and the measured switching times might be due to jitter in the device switching or variations in device capacitance.

Research Group	PVR	I_P (KA/cm^2)	avg. R_n $(\mu\Omega - cm^2)$	C (nF/cm^2)	$\frac{R_d}{\lvert R_n \rvert} \equiv y$	T_{rise} (ps)
Lincoln Labs	3.5	40	16	160	2.6	12
Texas Instr.	1.6	80	4.2	340	1.0	4.6
Fujitsu	14	23	13	340	1.5	13

Table 5.2: Minimum rise time for best devices

Bias (V)	C_p (fF)	R_s (Ω)	C (fF)	R (Ω)
0.5	32	14.9	19.5	205
1.0	32	14.9	19.5	60
1.5	32	14.9	19.5	41

Table 5.3: Independently measured RTD circuit elements

Device	R_s ($\Omega -$ μm^2)	$\lvert R_n^{avg} \rvert$ ($\Omega -$ μm^2)	C ($fF/$ μm^2)	f_{max} (GHz)	f_t (GHz)	$4.5R_n^{avg}C$ (ps)
GEN1	233	650	1.3	254	190	4
GEN2	233	340	2.5	227	190	4

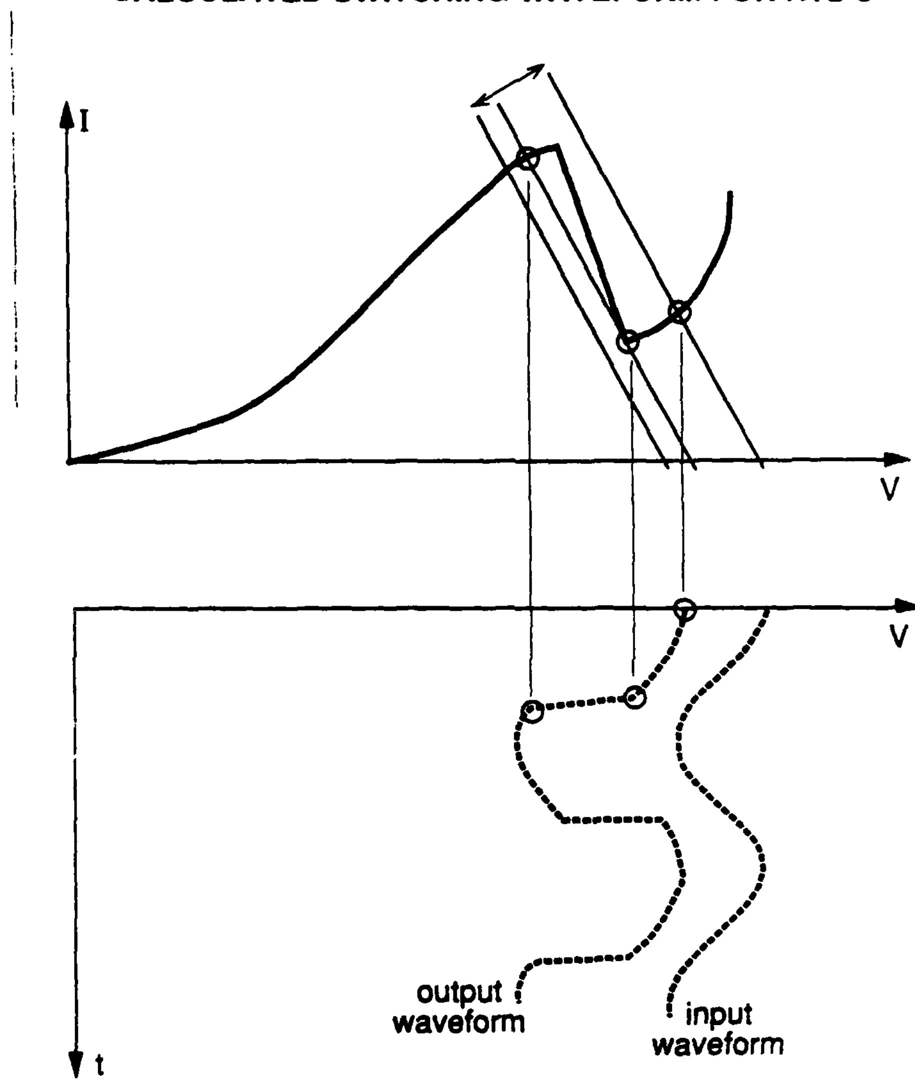

Figure 5.11: Expected switching waveforms with a sinusoidal input.

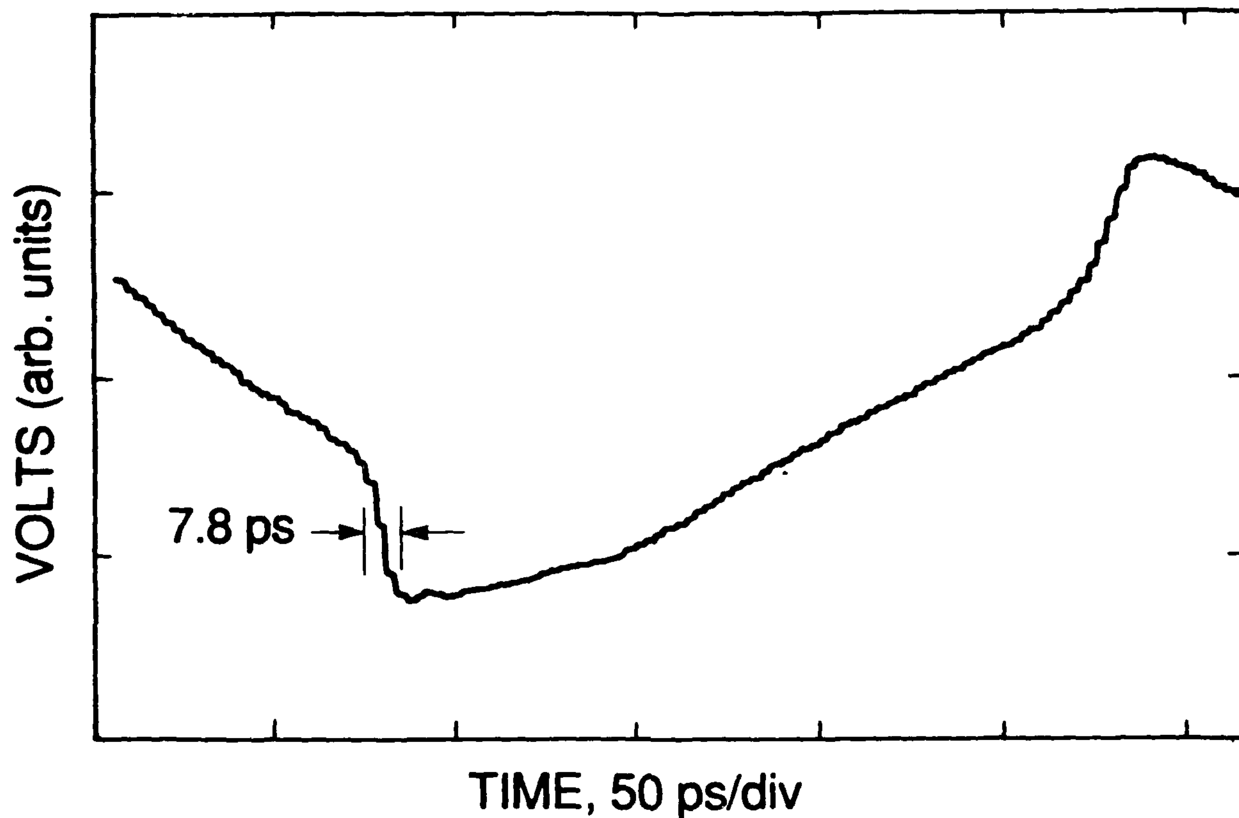

Figure 5.12: Measured switching waveform with electrooptic sampling. The quantization in the time axis is due to the measurement system

References

[5.1] E.R. Brown, W.D. Goodhue and T.C.L.G. Sollner "Fundamental Oscillations up to 200 GHz in Resonant Tunneling Diodes and New Estimates of their Maximum Oscillation Frequency from Stationary-State Tunneling Theory," *J. Appl. Phys.* **64**, 1519–1529 (1988).

[5.2] F. Capasso, S. Sen A.C. Gossard, A.L. Hutchinson and J.H. English "Quantum-well resonant tunneling bipolar transistor operating at room temperature," *IEEE Electron Device Lett.* **EDL-7**, 573–576 (1986).

[5.3] M.A. Reed, W.R. Frensley, R.J.Matyi, J.N. Randall and A.C. Seabaugh "Realization of a three-terminal resonant tunneling device: The bipolar quantum resonant tunneling transistor," *Appl. Phys. Lett.* **54**, 1034–1036 (1989).

[5.4] P. Wolf, *Picosecond Optics and Optoelectronics*, edit by G.A. Mourou, D.M. Bloom and C.-H. Lee, Springer-Verlag, 1985, p. 236

[5.5] C.J. Madden, R.A. Marsland, M.J.W. Rodwell D.M. Bloom and Y.C. Pao "Hypeabrupt-doped *GaAs* nonlinear transmission line for picosecond shockwave generation," *Appl. Phys. Lett.* **54**, 1019–1021 (1989).

[5.6] R.A. Marsland, V. Valdivia, C.J. Madden, M.J.W. Rodwell and D.M. Bloom, "130 GHz *GaAs* monolithic integrated circuit sampling head" To be published

[5.7] A. Barna, *High-speed pulse ciruits*, Wiley-Interscience, 1970

[5.8] W.F. Chow, *Principles of tunnel diode circuits*, John Wiley & Sons 1964

[5.9] E.R. Brown, T.C.L.G. Sollner, W.D. Goodhue and C.D. Parker "Millimeter-band oscillations based on resonant tunneling in a double-barrier diode at room temperature," *Appl. Phys. Lett.* **50**, 83–85 (1987).

[5.10] M.A. Reed, J.W. Lee and H-L. Tsai "Resonant tunneling through a double $GaAs/AlAs$ superlattice barrier, single quantum well heterostructure," *Appl. Phys. Lett.* **49**, 158–160 (1986).

[5.11] T. Inata, S. Muto, Y. Nakata, S. Sasa, T. Fujii and S. Hiyamizu "A psuedomorphic $In_{0.53}Ga_{0.47}As/AlAs$ resonant tunneling barrier with a peak-to-valley current ratio of 14 at room temperature," *Jpn. J. Appl. Phys.* **26**, L1332–L1334 (1987).

[5.12] V.J. Goldman, D.C. Tsui and J.E. Cunningham "Observation of intrinsic bistability in resonant-tunneling structures," *Phys. Rev. Lett.* **Vol. 58, No. 12**, 1256–1259 (1987).

[5.13] T.C.L.G. Sollner "Comment on 'Observation of intrinsic bistability in resonant-tunneling structures'," *Phys. Rev. Lett.* **Vol. 59, No. 14**, 1622–1623 (1987).

[5.14] H.C. Lui "Simulation of extrinsic bistability of resonant tunneling structures," *Appl. Phys. Lett.* **53**, 485–486 (1988).

[5.15] K.J. Weingarten, M.J.W. Rodwell and D.M. Bloom "Picosecond optical sampling of GaAs integrated circuits," *IEEE J. of Quant. Electr.* **QE-24**, 198–220 (Feb. 1988).

PUBLICATIONS

J. S. Harris, Jr.

1. S. Y. Chou, E. Wolak, J. S. Harris, Jr. and R. F. W. Pease, "Resonant Tunneling of Electrons of 1 or 2-Degrees of Freedom," *Appl. Phys. Lett.* **52** (8), 657-659, 22 February 1988. (Supported by ONR N00014-86-K-0530 and by JSEP DAAG-29-85-K0048.)

2. G. W. Yoffe, D. G. Schlom and J. S. Harris, Jr., "Summary Abstract: MBE Growth of Tunable Multi-Layer Interference Optical Modulators," *J. Vac. Sci. Technol. B.* **6** (2), 688, Mar/Apr 1988. (Supported by DARPA and ONR through contracts N00014-84-K-0077 and N00014-86-K-0530)

3. G. W. Yoffe, D. G. Schlom and J. S. Harris, Jr., "Modulation of Light by Electrically Tunable Multi-Layer Interference Filter," *Appl. Phys. Lett.* **51** (23), 1876-1878, 7 December 1987. (Supported by DARPA and ONR N00014-84-K-0077 and N00014-86-K-0530)

4. S. Y. Chou and J. S. Harris, Jr., "Room-Temperature Observation of Resonant Tunneling Through a AlGaAs/GaAs Quasi-Parabolic Quantum Well Grown by MBE," *Appl. Phys. Lett.* **52** (17), pp. 1422-1424, 25 April 1988. (Supported by DARPA and ONR N00014-86-K-0530 and N00014-84-K-0077)

5. K. L. Lear, K. Yoh and J. S. Harris, Jr., "Monolithic Integration of GaAs/AlAs Resonant Tunnel Diode Load and GaAs Enhancement-Mode MESFET Drivers for Tunnel Diode FET Logic Gates," to be published in *Proceedings of 15th International Symposium on Gallium Arsenide and Related Compounds,* Atlanta, GA, September 1988. (Supported by DARPA N00014-84-K-0077 and ONR N00014-86-K-0530)

6. S. K. Diamond, E. Özbay, M. J. W. Rodwell, D. M. Bloom, Y. C. Pao, E. Wolak and J. S. Harris, "Fabrication of 200GHz F_{max} Resonant Tunneling Diodes for Integrated Circuit and Microwave Applications," *IEEE Electron Device Letters,* **10** (3), 104-106, March 1989. (Supported by ONR N00014-86-K-0530)

7. E. Wolak, K. L. Lear, P. M. Pitner, B. G. Park, E. S. Hellman, T.Wejil and J. S. Harris Jr., "The Effect of Elastic Scattering Centers on the Current Voltage Characteristics of Double Barrier Resonant Tunneling Diodes", to be published in Proceedings of SPIE #943 (Supported by DARPA N00014-84-K-0077 and the Office of Naval research)

8. E. Wolak, K. L. Lear, P. M. Pitner, E. S. Hellman, B. G. Park T.Weil, and J. S. Harris, Jr., "Elastic Scattering Centers in Resonant Tunneling Diodes" submitted Appl. Phys Lett. **53** (3), July 1988. (Supported by ONR and DARPA N00014-84-K-0077).

9. S. K. Diamond, E.Ozbay, M. J. W. Rodwell and D. M. Bloom, Y. C. Pao, E. Wolak, and J. S. Harris, Jr., "Fabrication of Resonant Tunneling Diodes for Switching Applications" *(Supported by ONR N00014-84-K-0530).*